PRESSURE-INDUCED PHASE TRANSITIONS
OF INDIUM SELENIDE

By

ANYA MARIE RASMUSSEN

A dissertation submitted in partial fulfillment of
the requirements for the degree of

DOCTOR OF PHILOSOPHY

WASHINGTON STATE UNIVERSITY
Department of Physics and Astronomy

MAY 2016

To the Faculty of Washington State University:

The members of the Committee appointed to examine the dissertation of ANYA MARIE RASMUSSEN find it satisfactory and recommend that it be accepted.

Matthew D. McCluskey, Ph.D., Chair

Yi Gu, Ph.D.

Choong-Shik Yoo, Ph.D.

Acknowledgements

I wish to thank:

My advisor, Matthew McCluskey, for teaching me how to do physics, from performing experiments to interpreting the results, and for mentoring and encouraging me these last six years.

My labmates for assisting in experiments, listening to practice talks, and for providing amusement during long work days.

Elham Mafi and Yi Gu for providing the nanowire samples, performing Raman measurements, and contributing to manuscripts.

The beamline 12.2.2 team at ALS/LBNL: Martin, Christine, Andrew, and Alistair, for hosting me last year as a doctoral fellow and for their assistance with the XRD experiments.

Wenguang Zhu for performing first-principles calculations.

Zhongwu Wang at CHESS for assisting with the XRD experiments.

My classmates for all the late nights finishing homework, our prelim study sessions, and emotional support. Michele and Kasey, I wouldn't have made it to the end without the two of you.

My family who have provided support, encouragement, and childcare: Candace (a.k.a. Aunt Candace), Mom (a.k.a. Grandma), Dad (a.k.a. Grandpa), Jill (a.k.a. Grammy), and Abby (a.k.a. ABBY!).

My husband, Chris. I am who I am today because of you.

Financial support by DOE (DE-FG02-07ER46386), NSF (DMR-1206960), and ACS-PRF (PRF# 51598-ND7) is gratefully acknowledged. The Advanced Light Source is supported by the Director, Office of Science, Office of Basic Energy Sciences, of the U.S. Department of Energy under Contract No. DE-AC02-05CH11231. The Cornell High Energy Synchrotron Source (CHESS) is supported by the National Science Foundation and the National Institute of Health/National Institute of General Medical Sciences under NSF award DMR-0225180.

PRESSURE-INDUCED PHASE TRANSITIONS

OF INDIUM SELENIDE

Abstract

by Anya Marie Rasmussen, Ph.D.
Washington State University
May 2016

Chair: Matthew D. McCluskey

In_2Se_3 has potential as a phase-change material for memory applications. Understanding its phase diagram is important to achieve controlled switching between phases. Pressure-dependent phase transitions of In_2Se_3 bulk powders and nanowire samples were studied at room temperature and at elevated temperatures using synchrotron x-ray diffraction and diamond-anvil cells (DACs). α-In_2Se_3 transforms into the β phase at 0.7 GPa, an order of magnitude lower than phase-transition critical pressures in typical semiconductors. The bulk moduli are reported and the c/a ratio for the β phase is shown to have a highly nonlinear dependence on pressure. γ-In_2Se_3, metastable under ambient conditions, transforms into the high-pressure β phase between 2.8 GPa and 3.2 GPa in bulk powder samples and at slightly higher pressures, between 3.2 GPa and 3.7 GPa, in nanowire samples. While the γ phase bulk modulus is similar to that of the β phase, the decrease due to pressure in the unit cell parameter ratio, c/a, is less than half the decrease seen in the β phase. Using high-temperature DACs, we investigated how elevated temperatures and pressures affect the crystal structure of In_2Se_3. From these measurements, the high-pressure β phase was found to be metastable. The high-pressure β phase transitions into the high-temperature β phase at temperatures above 380 °C.

Dedication

To Madeline Marie.

Contents

List of Figures

Chapter 1

Introduction

The push for smaller, faster, and even physically flexible mobile and wearable computing devices is driving demand for increasingly compact and efficient digital memory. Phase change random access memory (PRAM) is a promising alternative to flash memory for use in mobile devices. PRAM utilizes the electronic and optical differences between various amorphous and crystalline phases of a phase change material [1].

The most common phase change materials studied and used in prototype PRAM devices are chalcogenides, with germanium-antimony-tellurium (GST) compounds being the most common [1]. In a chalcogenide PRAM device the amorphous and crystalline phases correspond to digital 0 and 1 states of the bits. Two electrodes are placed across the phase change material and phase switching is controlled by heating the material using one of the electrodes, the heating electrode (figure 1.1). The state of the bit is then read by measuring the resistance of the material across the electrodes.

Flash memory requires erasing and then rewriting in large memory blocks. PRAM, however, is written and erased bit-by-bit, resulting in faster write-rewrite times. PRAM can also withstand several orders of magnitude more write-rewrite cycles than flash memory before the device begins to degrade [1]. Perhaps most importantly, a PRAM approach to memory storage allows for multilevel memory [1, 2]. One multi-level PRAM method is to

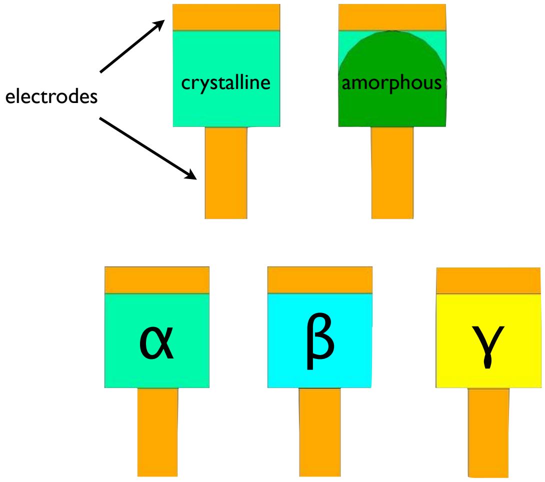

Figure 1.1: Phase change memory bits.

select a material that has multiple stable and metastable crystalline states under operating and atmospheric conditions. Then a single physical bit can hold multiple digital information bits (figure 1.1), thereby increasing the storage density of the PRAM device.

For this work we investigated the thermodynamic properties of several crystalline phases of indium selenide (In_2Se_3), a phase change material that could be used as an alternative material to GST compounds in PRAM devices [2–4].

1.1 Indium selenide

In_2Se_3 is a III-VI semiconductor and phase change material that exists in multiple crystalline phases, including the layered α and β phases and the defect wurtzite γ phase [5–9]. In_2Se_3 may offer advantages over $Ge_2Sb_2Te_5$ as a potential PRAM material because of its higher resistivity and the large difference in resistivity between the crystalline and amorphous phases, up to a factor of 10^5 [3]. In addition, the multiple metastable crystalline phases of In_2Se_3 at ambient conditions may allow for multilevel memory [2,10]. The use of In_2Se_3 in a PRAM device requires the ability to precisely control the switching between phases. To accomplish this, it is important to understand the phase transformations of the material under various conditions of temperature and stress. Stresses in operating Ge-Sb-Te devices are estimated to be on the order of GPa [11].

Figures 1.2 (a)-(c) show ball and stick models of the crystal structures for the α, β, and γ phases. Each layer of the α and β phases consists of five alternating sub-layers of selenium and indium atoms. Neighboring layers interact through van der Waals forces. The γ phase is a defect wurtzite structure with vacancies ordered in a screw pattern on every third In site [6,8]. It can crystalize in a number of related space groups, $P6_1$, $P6_5$, $P6_122$, or $P6_522$, corresponding to particular arrangements of the vacancy screws [6–8]. γ phase In_2Se_3 is isostructual with the ambient phases of the topological insulators Sb_2Te_3, Bi_2Te_3, and Bi_2Se_3 [9,12].

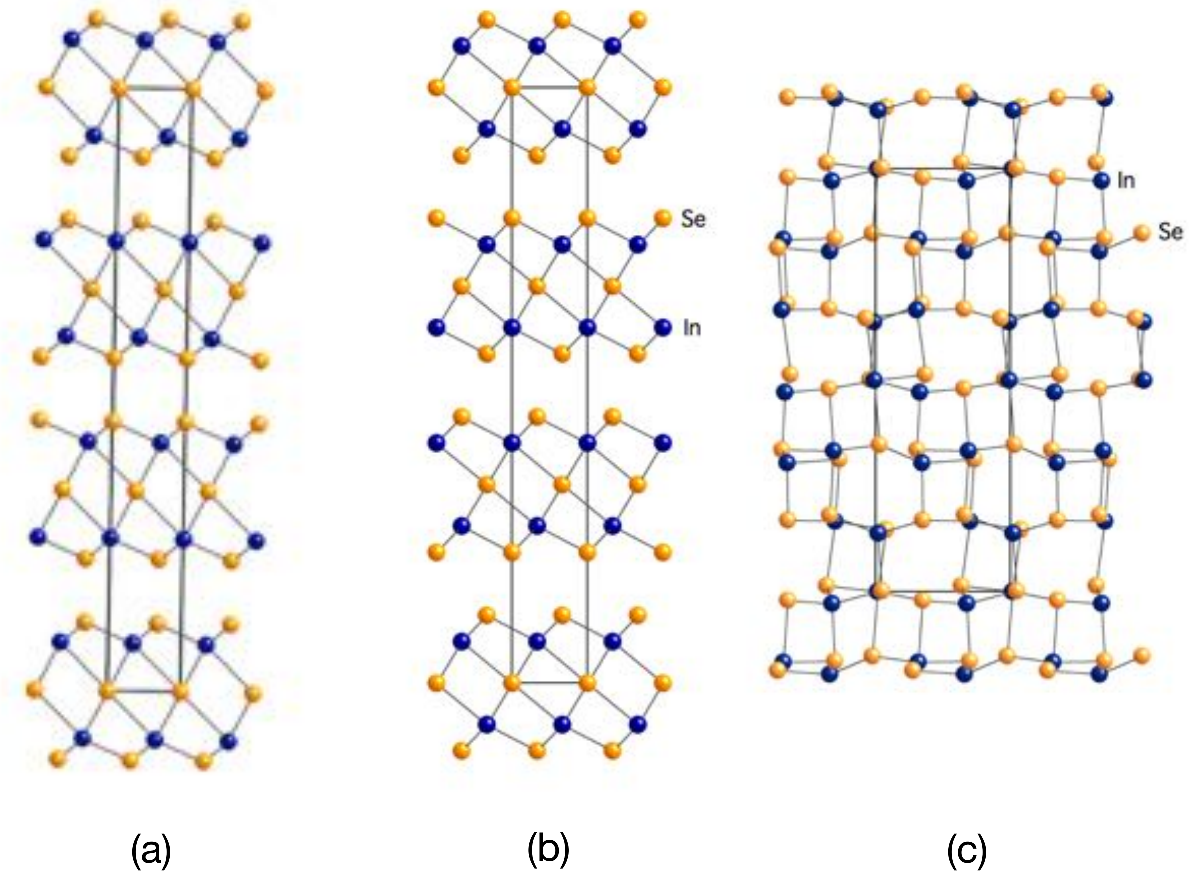

Figure 1.2: Ball-and-stick models of In_2Se_3 crystal structures. (a) and (b) are models of α and β phases, respectively, showing the rhombohedral $R\bar{3}m$ space group and atomic positions determined by Ke et al. [13]. (c) γ phase model showing the $P6_1$ space group and atomic positions determined by Pfitzner and Lutz [6].

Known temperature-dependent phase transitions for bulk In_2Se_3 include the α to β phase transition at 473 K, the β to γ phase transition at 793 K, and the γ to δ transition at 1003 K [5]. While the temperature-induced phase transitions in In_2Se_3 have been well studied, the pressure dependence of these phase transitions had not been reported prior to this work.

1.2 Phase Transitions

The equilibrium condition for a thermodynamic system is that the Gibbs potential, $G = U + PV - TS$, is minimized [14]. Consider a thermodynamic system with the Gibbs potential plotted verses volume at three different pressures (figure 1.3). The Gibbs potential has two local minima separated by a barrier. At P_1, the system's thermodynamically stable phase corresponds to the right minimum and has volume V_1. If the pressure is increased through the transition pressure P_2, where the minima become equal, to pressure P_3, then the phase corresponding to the left minimum becomes the stable phase and will have a volume V_3.

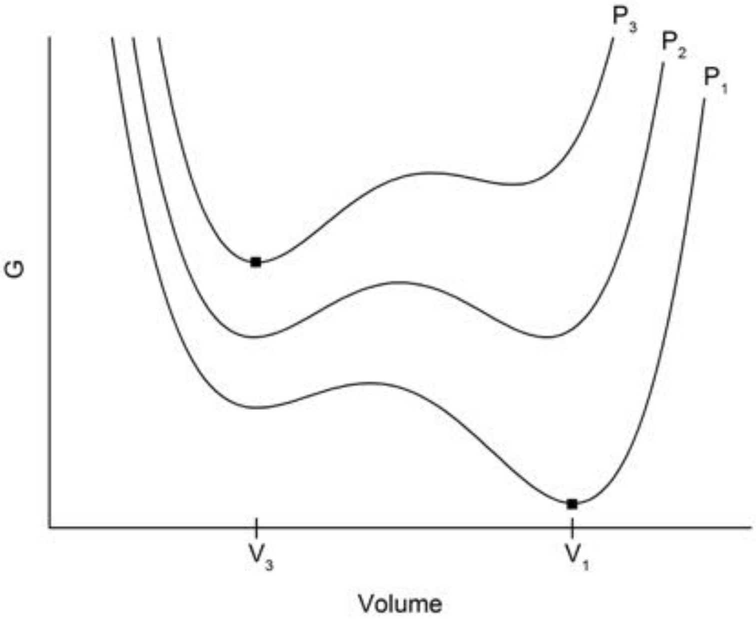

Figure 1.3: Gibbs potential verses volume at three different pressures, $P_1 < P_2 < P_3$.

At a phase transition the Gibbs potential for each phase must be equal; however, there may be a discontinuity in the derivatives of the Gibbs potential [14]. Phase transitions are often classified by the order of the derivative where this discontinuity occurs. In a first-order phase transition there is a discontinuity in the first derivative of the Gibbs potential. In a second-order transition the Gibbs potential and the first derivatives are equal for both phases and a discontinuity is observed in one or more of the second derivatives. For pressure-induced transitions, the first derivative is

$$\frac{\partial G}{\partial P}_T = V. \tag{1.1}$$

Therefore, we will see a discontinuous change in volume for a first-order phase transition. In a second-order transition the discontinuity is observed in the compressibility of the material [15].

In solids the barrier between local minima can be very large; so large that transitions occur over very large time scales. This allows for long-living metastable phases. The most commonly known example of a long-lived metastable phase is diamond under atmospheric conditions. While diamond is not thermodynamically stable at atmospheric pressure and temperature, there is a large potential barrier that prevents diamond from transitioning into atmospherically stable graphite over any sort of observable timescale, so effectively "diamond is forever." The strength of a kinetic barrier separating a metastable phase and a stable phase can be altered by changing the pressure and temperature conditions. For some critical pressure and temperature the metastable phase will transform into the stable phase over an experimentally observable timescale [16]. At sufficiently elevated temperatures the lifetime of diamond is significantly reduced, to just hours at 1700 K [16].

In_2Se_3 is a "phase change" material with a variety of crystal structures. α-In_2Se_3 is the stable phase at ambient temperature and pressure. The β and γ phases are both metastable under ambient conditions and can be produced by annealing α-In_2Se_3 at a temperature within the temperature range for which the desired phase is stable followed by a room temperature quench.

1.3 Subject of this work

In this work we looked for pressure-induced phase transitions in bulk powder and nanocrystaline In_2Se_3 by conducting *in situ* high-pressure x-ray diffraction (XRD) experiments on the In_2Se_3 samples using diamond anvil cells (DACs) and synchrotron radiation as an x-ray source. A first-order phase transformation was identified by a discontinuous change in the XRD pattern with changing pressures. From the XRD spectra taken at various pressures a discontinuity in the unit cell volume and/or a restructuring of atoms resulting in a new crystal symmetry can be detected. In addition to the high-pressure experiments, high-temperature DAC experiments were conducted to investigate how elevated pressures effect the thermally driven phase transitions in In_2Se_3.

Chapter 2

Experimental and Analytical Techniques

This chapter describes the experimental methods, equipment, and analysis techniques used to complete this work.

2.1 Diamond anvil cells

Diamond anvil cells (DACs) are simple devices used to create extremely large pressures [17, 18]. Samples are compressed between the flattened tips, or culets, of two opposing diamonds. Figure 2.1 shows a cross section of the interior of a DAC. Four different types of DACs were used, piston-cylinder DACs [figure 2.2 (a)], Merrill-Bassett style DACs [figure 2.2 (b)], a BX90 DAC supplied by the ALS Beamline 12.2.2 [figure 2.2 (c)] and a parallel plate DAC supplied by the the Advanced Light Source (ALS) Beamline 12.2.2 (not pictured). Due to the small surface of the diamond culets, only a moderate amount of force applied to the diamonds is needed to create high pressures within the sample chamber, as pressure=force/surface area. Pressures reaching up to hundreds of gigapascals can be achieved in a DAC, with the record high pressure being 770 GPa with the use of second stage micro-anvils [19]. When applying moderate pressures, relatively large culet diameters are preferable because they allow for finer control of the pressure steps. For this work I used anvils with culet diameters of 300 μm, 600 μm, or 1000 μm.

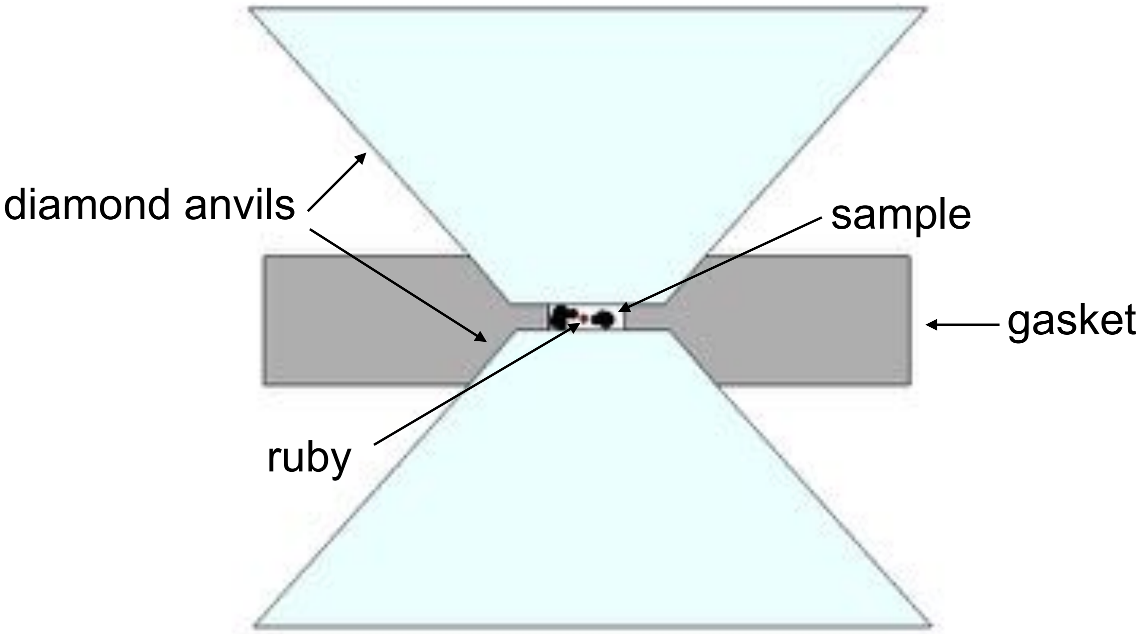

Figure 2.1: Cross section of a diamond anvil cell.

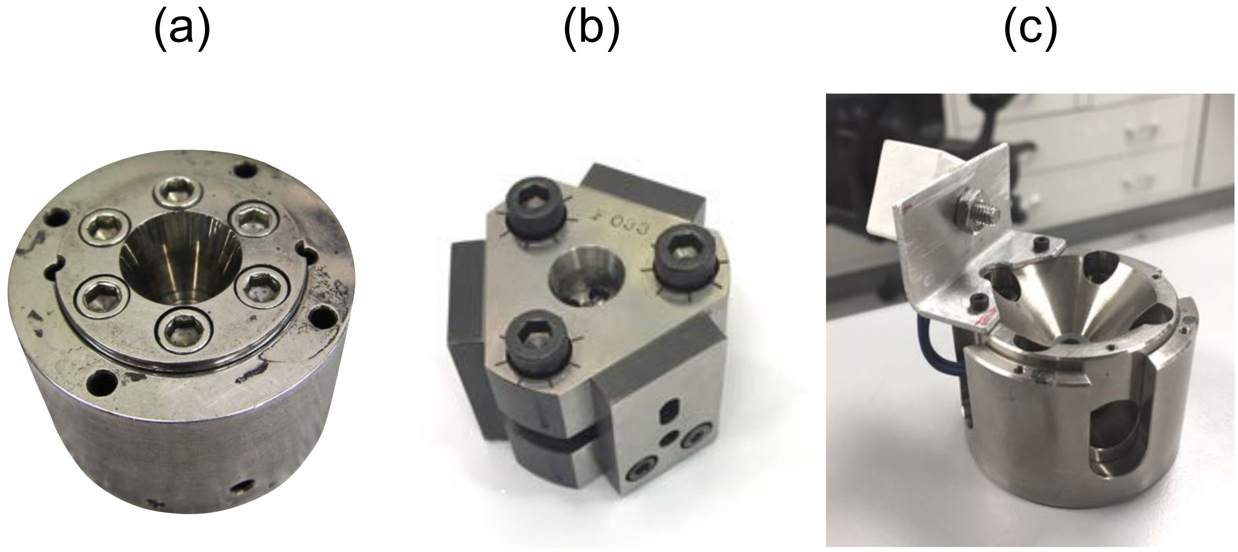

Figure 2.2: (a) piston-cylinder DAC. (b) Merril-Bassett style DAC. (c) BX90 DAC.

2.2 Gasket preparation

To create an enclosed sample chamber, a pre-indented stainless steel gasket was made by first pinching a small piece of stainless steel sheet metal with initial thickness of 250 μm between the diamond anvils, then drilling a hole centered inside the indention. Pre-indenting the gasket helps reduce the chance of gasket failure from the hole collapsing under compression. Proper diamond culet alignment is determined by monitoring the interference fringe pattern created between the diamond culet faces while carefully tightening the DAC screws. When the fringes just disappear off the edge of the culet faces, the faces are parallel (see figure 2.3). A dial indicator is then used to measure relative heights at three different locations on the top surface of the DAC. Figure 2.4 shows a piston cylinder DAC with markings indicating the three spots where the height was measured.

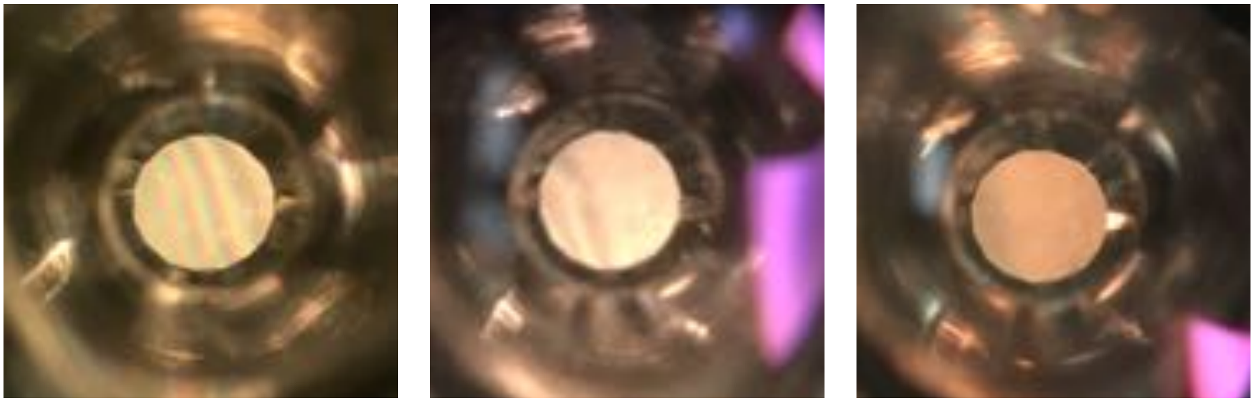

Figure 2.3: Anvil alignment using the interference fringes. Culet diameter=500 μm.

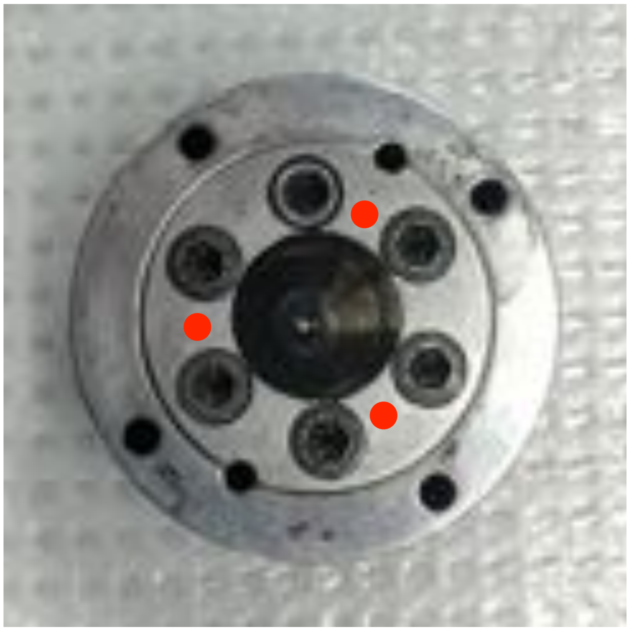

Figure 2.4: Height measurement locations on a DAC used to maintain proper alignment when indenting gaskets.

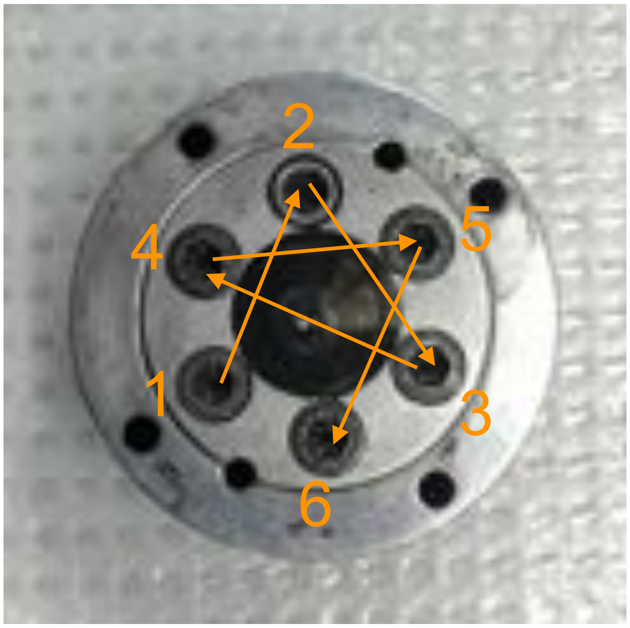

Figure 2.5: Screw tightening pattern for the piston cylinder DACs.

The gasket material is then placed in the DAC between the anvils. The indention is made by carefully tightening the DAC screws in an appropriate pattern for evenly compressing the gasket (figure 2.5). Diamond alignment is maintained by checking the relative heights of the marked locations and correcting for any deviations between each round of screw tightening. When the gasket has been indented to the desired thickness, $\sim 50\ \mu$m (measured by the dial indicator), the screws are carefully and evenly loosened and the gasket is removed.

The primary drilling method we use is an electrode discharge drill manufactured by Besta (figure 2.6). The electrode drill creates a clean circular hole. The diameter of the gasket hole is determined by the size of the electrode. Approximately 300 μm and 500 μm diameter gasket holes were drilled for anvils with 600 μm or 1000 μm diameters, respectively. Figure 2.7 shows a finished gasket pre-indented with 1000 μm diameter culet diamonds and an approximately 500 μm diameter hole. When preparing gaskets at the ALS, an Oxford laser mill was used for drilling gasket holes.

Figure 2.6: Besta electrode discharge drill.

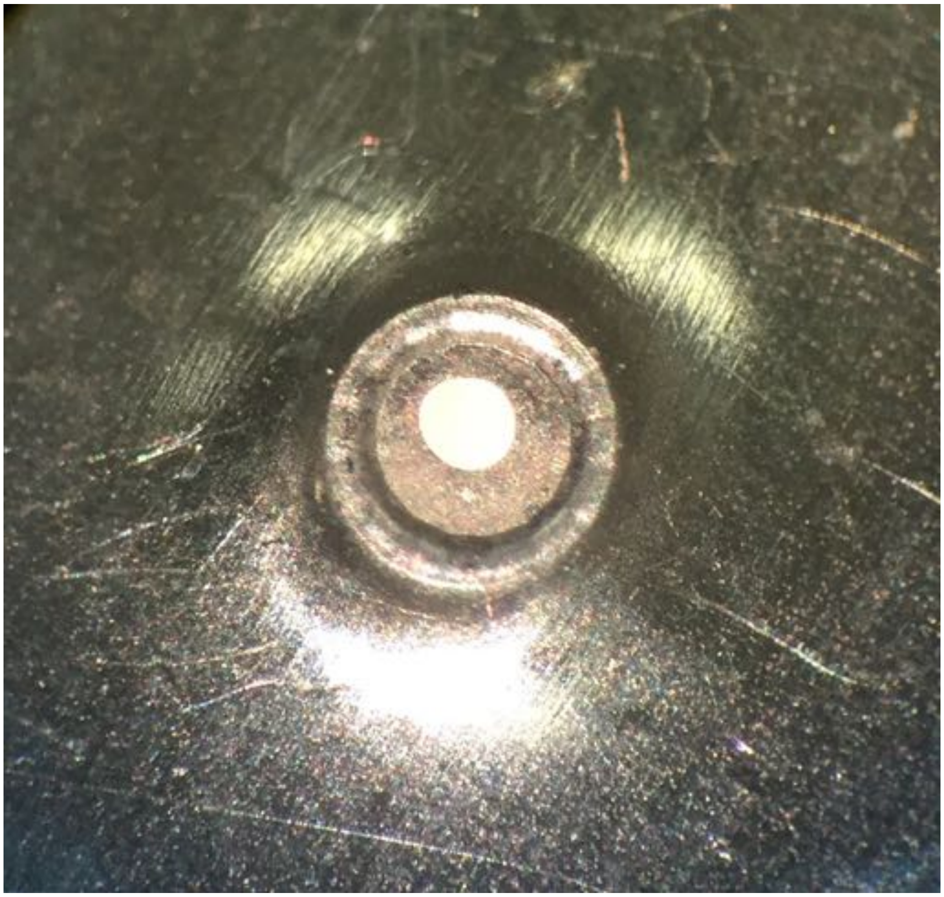

Figure 2.7: Pre-indented gasket for 1000 μm diameter culet diamond anvils and an approximately 500 μm diameter hole.

2.3 Sample Loading

To load the DAC, first the pre-indented gasket is placed over the bottom diamond anvil so that the indention and hole are properly aligned over the diamond culet. Small balls of modeling clay are used to help hold the gasket in place. Next, I use a needle to pick up a small amount of the powder sample and deposit it into the gasket hole and repeat until about 3/4 of the hole is covered in sample. Then, again using a needle, a few ruby micro spheres [20], which will be used for *in situ* pressure measurements, are placed in the gasket hole. Figure 2.8 shows a gasket loaded with the In_2Se_3 bulk powder.

Finally, I fill the gasket with a pressure transmitting medium. Two different pressure media were used, either a 4:1 methanol-ethanol mixture, which is known to provide hydrostatic conditions up to 10 GPa [21], or mineral oil, which is hydrostatic up to 4 GPa as determined by the width and splitting of the ruby lines [22]. I have two different methods to fill the sample chamber with the pressure medium. The first uses a syringe to deposit drops of the medium into the gasket indention before closing the DAC and lightly securing the screws, just tight enough to seal the sample chamber. This method works well when using mineral oil because it doesn't evaporate during loading and screws can be left just "finger tight," allowing us to load a DAC to ambient pressure. The methanol-ethanol mixture, however, evaporates quickly, making it more difficult to load using the syringe method. An alternative method to load the piston cylinder DACs is to gently close the DAC with the top anvil hovering just over the gasket indention and then place the DAC into a dish and fill the dish with the methanol-ethanol mixture. The cylinders have holes in the bottom that allow the pressure-medium to flood the DAC and the sample chamber. I then tighten the screws to seal the sample chamber and remove the DAC from the dish.

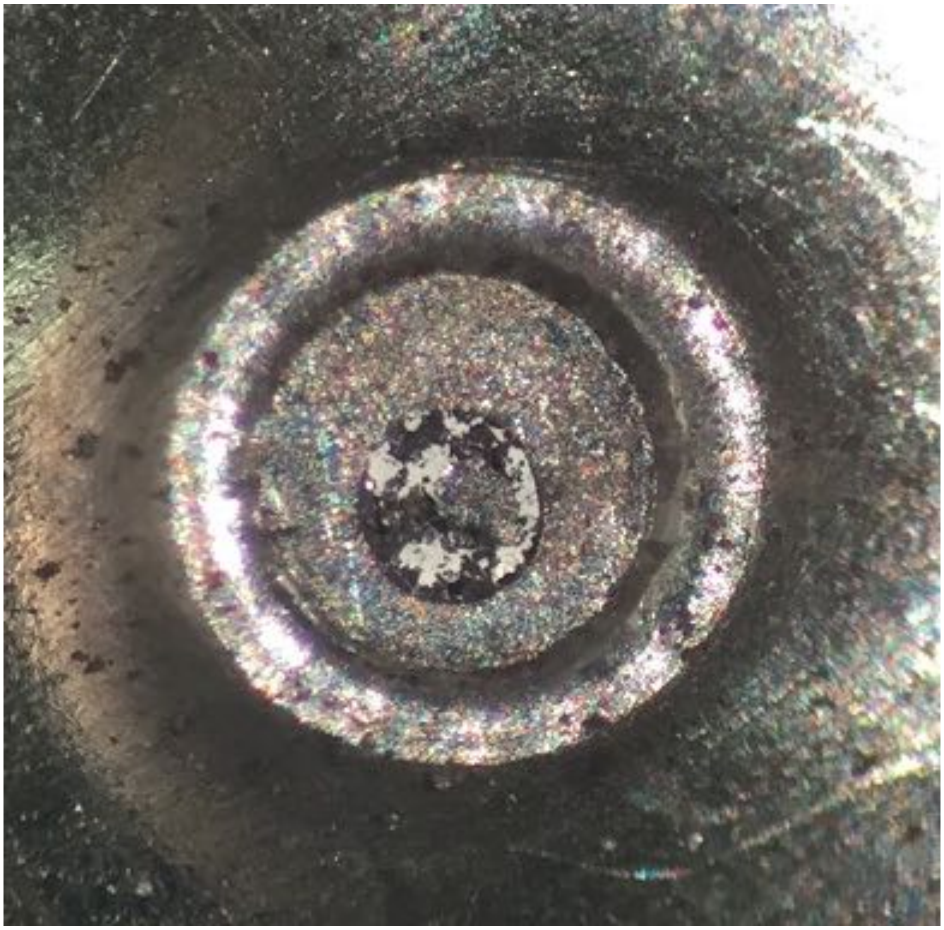

Figure 2.8: Mounted gasket loaded with In_2Se_3 bulk powder

2.4 Raman Spectroscopy

In 1930 C. V. Raman received the Nobel Prize in physics for demonstrating inelastic scattering of light. Using filters and focused sunlight he created a monochromatic light source and observed a color shift in the light scattered from various liquids. It was several decades later, with commercial availability of lasers, that Raman spectroscopy took off as a common experimental technique [23]. Raman spectroscopy probes the low-frequency modes of a system, such as the vibrational modes of a molecular or crystal system, and can be used to identify and characterize a material. Monochromatic light, typically from a laser in the visible, near IR, or near UV range, illuminates the sample and the intensity of the scattered light is measured as a function of wavenumber (inverse wavelength) [23]. The scattered light with the same wavelength as the source is filtered out and only the inelastically scattered light, which has been either shifted down in frequency, Stokes shifted, or shifted up in frequency, anti-Stokes shifted, is detected. A Stokes shift in the scattered light occurs when the system transitions into a higher vibrational energy level due to the perturbing illumination and an anti-Stokes shift occurs when the system transitions into a lower vibrational energy level (figure 2.9). In a crystal lattice a quantum of vibrational energy can be represented as a quasiparticle called a phonon. Stokes Raman scattering results in the creation of a phonon and anti-Stokes Raman scattering results in the annihilation of a phonon [24].

We used Raman spectroscopy to identify the phases present in our In_2Se_3 samples. A 633 nm He-Ne laser was used as the light source and the scattered light was collected by a Leica optical microscope coupled to a Renishaw InVia spectrometer.

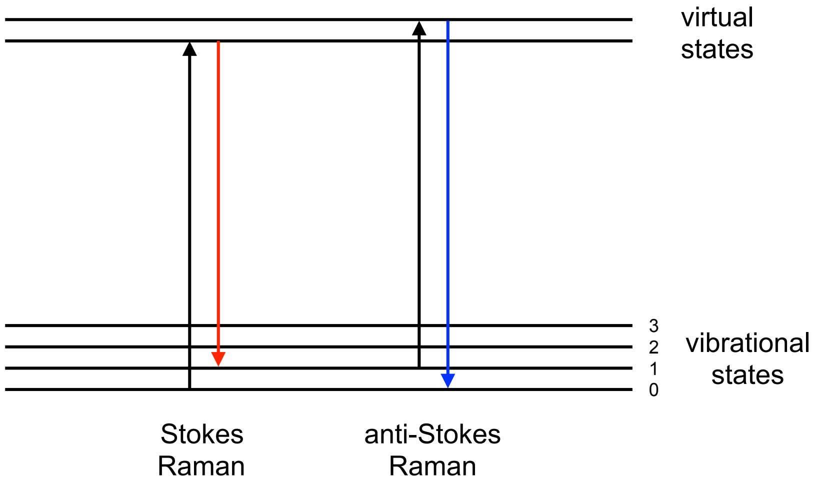

Figure 2.9: Energy-level model showing Stokes Raman scattering and anti-Stokes Raman scattering.

2.5 Ruby Fluorescence for pressure measurements

Ruby fluorescence has become one of the most common methods for determining the pressure inside a DAC. In the 1970's there was a push to develop a spectroscopic pressure calibration method [18]. The ruby R_1 and R_2 fluorescence peaks were found to shift linearly with pressure in the 0 GPa - 20 GPa range with a slope of 2.740 GPa nm^{-1} [25]. Mao *et al.* extended the ruby pressure gauge to 80 GPa [26]. I use ruby microspheres purchased from RSA Le Rubis, which I load along with the sample for *in situ* pressure measurements. A green laser beam is focused on a ruby sphere inside the sample chamber and the resulting ruby fluorescence is measured. Figure 2.10 shows the fluorescence spectrum of a ruby sphere excited by a 532 nm laser at ambient pressure and the fluorescence of the same ruby sphere at an elevated pressure of 0.9 GPa as determined from peak shifts. Best practice is to take a ruby pressure measurement before and after each experimental measurement of the sample with the average pressure used as the experimental pressure.

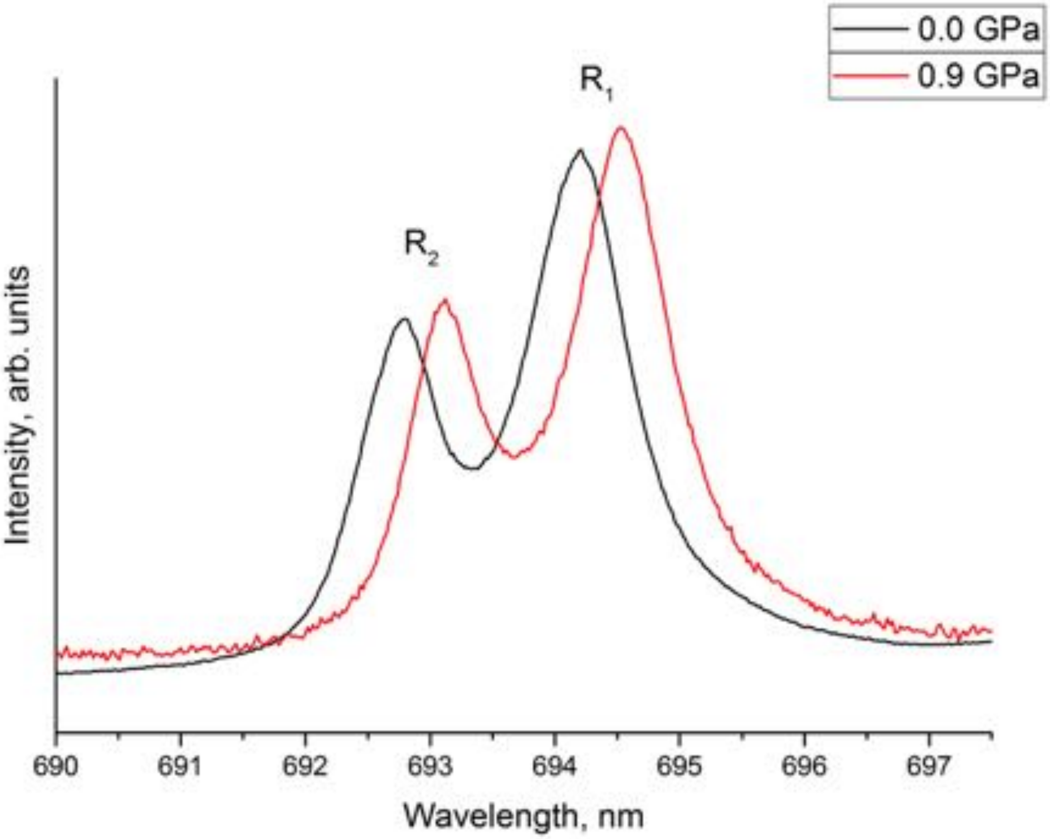

Figure 2.10: The fluorescence spectrum of a ruby sphere excited by a 532 nm laser at ambient pressure (black) and at an elevated pressure of 0.9 GPa (red).

2.6 Synchrotron X-ray Diffraction

Radiation from a relativistic particle undergoing centripetal acceleration was predicted by Liénard in 1898. Like many great scientific discoveries, it was first observed by accident in 1947 by a GE technician working on a 70-MeV electron synchrotron who was using a mirror to look for sparking in the electron tube. What he saw was an arc of light originating from the electron beam. The GE group, realizing that it was synchrotron radiation, began the experimental process of characterizing the beam [27, 28]. At first the radiation was viewed as an unfortunate energy loss. However, over the following two decades, the usefulness of synchrotrons as a radiation source became apparent, especially for solid-state research, and synchrotron light source user facilities were established.

Quoting William A. Bassett, “The diamond anvil cell and synchrotron radiation were made for each other” [18]. The small, well collimated, intense beam makes synchrotron radiation an ideal x-ray source for diamond anvil XRD studies. Soon after synchrotron light source user facilities became available, new styles of DACs were designed with larger conical shaped openings and x-ray transparent backing plates to allow for large diffraction angles [17, 18].

2.6.1 Bragg diffraction

The father-son team, William Henry and William Lawrence Bragg, won the 1915 Nobel prize in physics for their work using x-rays to determine crystal structures [29]. Radiation with wavelength comparable to inter-atomic distances scattered off a crystal will, at certain angles, interfere constructively. Bright peaks are detected at those angles. Consider two beams directed at an angle θ with respect to the atomic planes in a crystal and are scattered off two different atomic planes separated by a distance d (Figure 2.11). The second beam must travel a distance $2d\sin\theta$ farther than the first beam. Constructive interference occurs when the two beams reach the detector in phase, which occurs at angles where the difference in path length, $2d\sin\theta$, is equal to an integer number wavelengths, $n\lambda$. This is known as the Bragg diffraction condition:

$$2d\sin\theta = n\lambda. \tag{2.1}$$

The bright peaks in a diffraction pattern are located at angles that satisfy the Bragg diffraction condition and are called Bragg peaks. The location of a Bragg peak is measured relative to the incoming x-ray beam by the angle 2θ, where θ is the incident angle of the incoming beam with respect to the atomic planes of the crystal.

The lattice spacings for a crystal with a hexagonal unit cell can be found using the

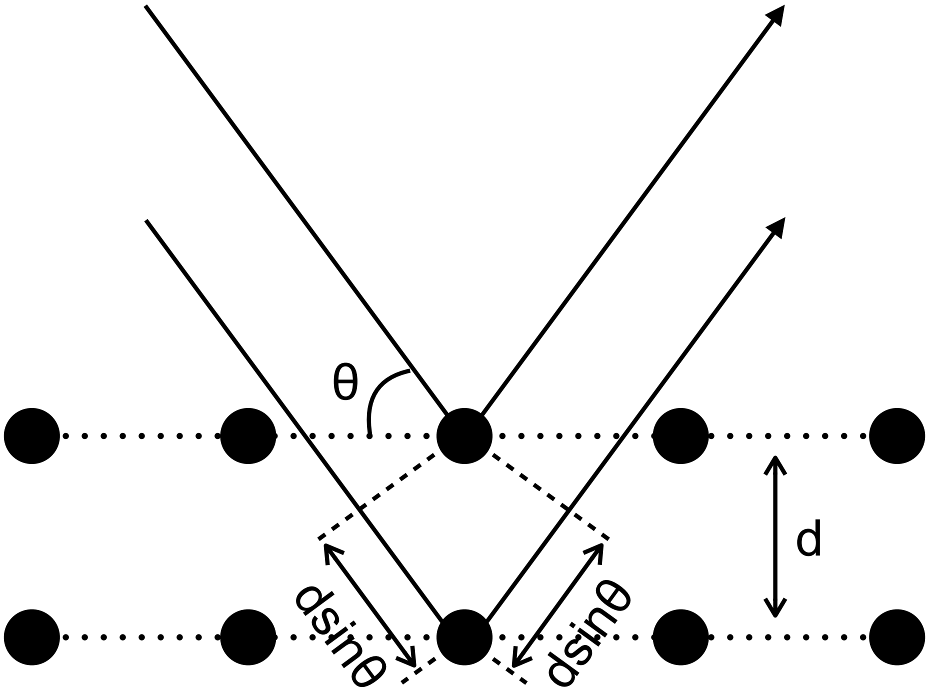

Figure 2.11: Illustration of Bragg's law.

relation:

$$\frac{1}{d^2} = \frac{4}{3}\left(\frac{h^2 + hk + k^2}{a^2}\right) + \frac{l^2}{c^2} \tag{2.2}$$

where h, k, and l are the Miller indices of the atomic plane.

In powder diffraction the sample is comprised of many small, randomly oriented crystals and the resulting diffraction pattern represents all possible crystal orientations simultaneously. Instead of the discrete bright spots detected in single crystal diffraction, smooth concentric diffraction rings (Debye-Scherrer rings) are imaged on a flat plate detector.

2.6.2 Experimental XRD setup

The XRD experiments for this work were done at both the Advanced Light Source (ALS) [30] and the Cornell High Energy Synchrotron Source (CHESS). Figure 2.12 is a photograph of the high-pressure beamline, 12.2.2, at the ALS. A tunable crystal monochromator is used to select the desired x-ray energy and mechanical slits allow control of the beam size. We typically used an energy of 25 keV (0.4959 Å) and beam widths between 10μm to 30μm. An illustration of the x-ray scattering and the resulting detected 2D image is shown in figure 2.13. The XRD spectra were collected by a high resolution MAR3450 plate detector. The ring spacings are measured by the angle 2θ (see figure 2.13). The distance between the sample and the detector must be precisely known to calculate the 2θ spacings of the Debye-Scherrer rings on the detected image. This distance is measured using a calibration spectrum from powder LaB_6. The known 2θ spacings of the XRD rings from LaB_6 allow the distance between the sample and detector to be calculated using the Fit2D analysis program. Unfortunately, the stainless steel backing plates for the piston cylinder DACs limit the 2θ diffraction angle to about 20°. However, this was sufficient to determine the lattice parameters with good accuracy.

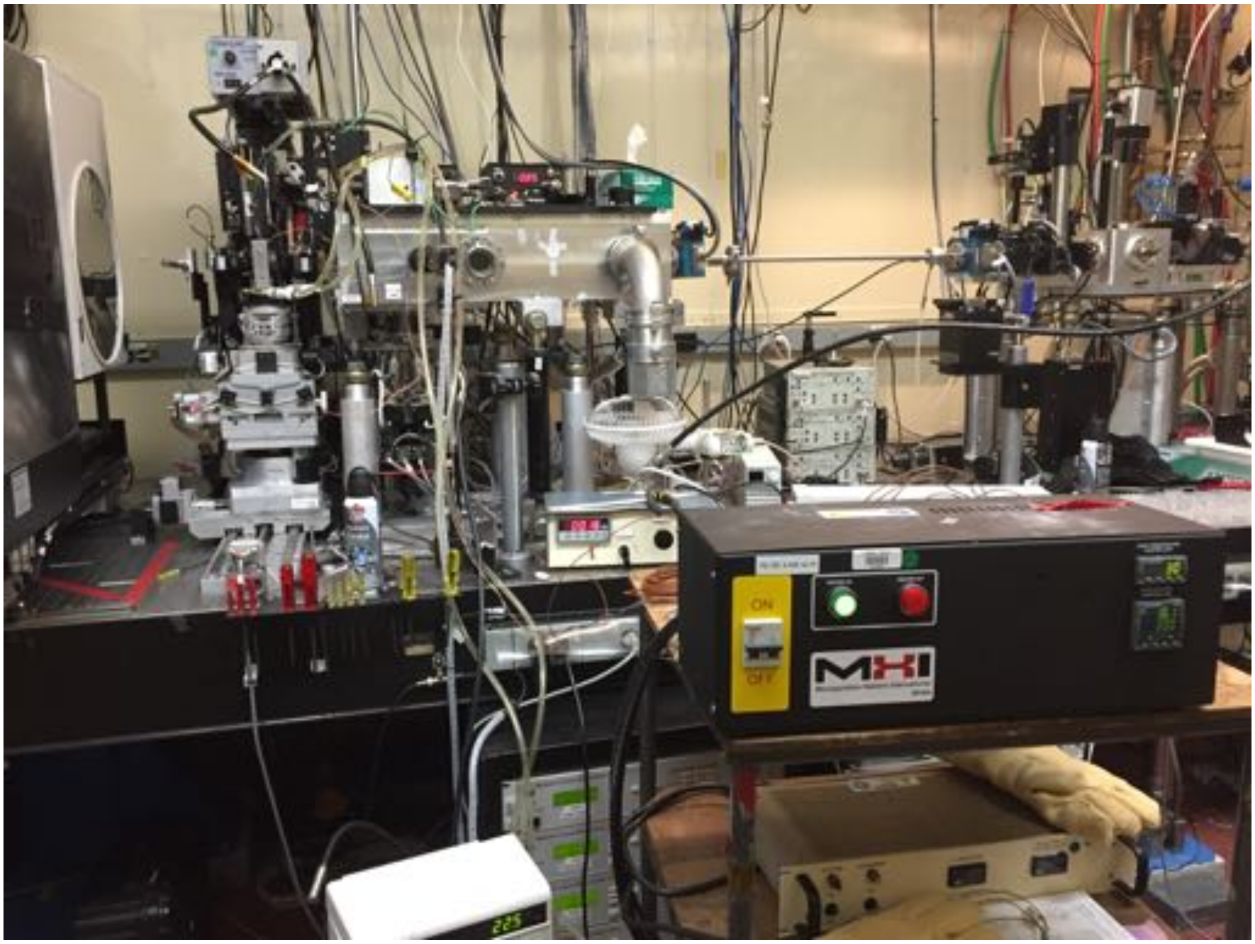

Figure 2.12: High Pressure Beamline 12.2.2 at the Advanced Light Source (ALS).

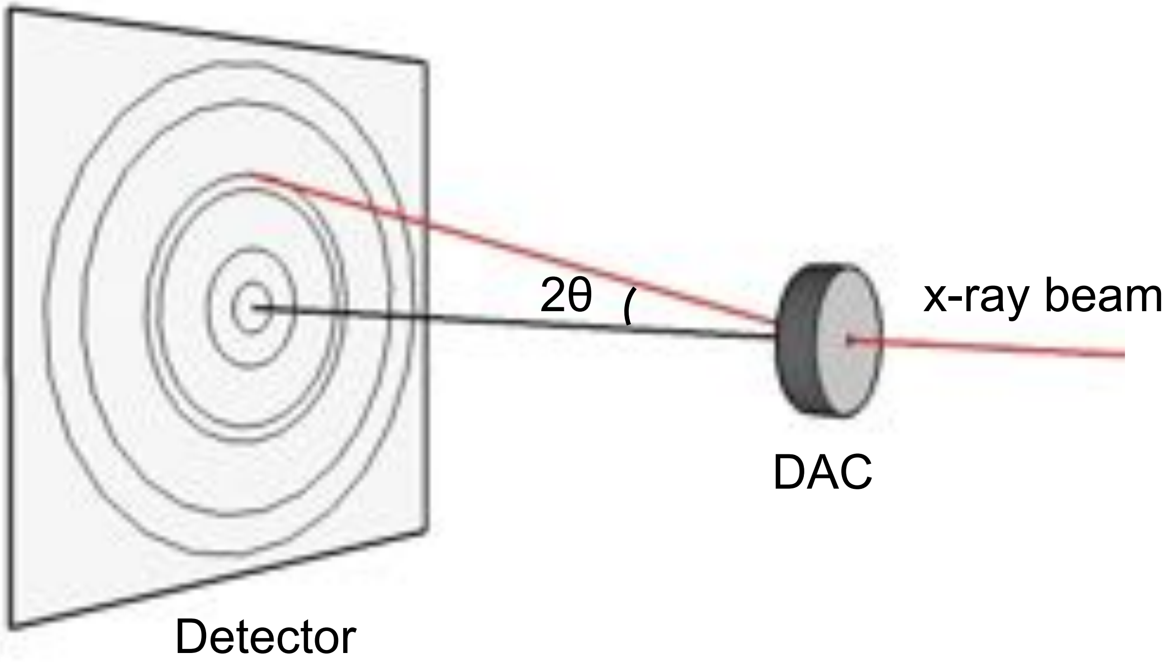

Figure 2.13: Illustration of powder x-ray scattering and the detected 2D image. Ring spacings are measured by the angle 2θ

Diffraction images were integrated using the FIT2D program [31]. Figure 2.14 shows an example 2D powder diffraction image collected by the MAR3450 detector and the 1D spectrum, intensity verses 2θ, after the FIT2D integration. Each peak in the 1D spectrum corresponds to a Debye-Scherrer ring. From the 1D spectrum we obtain the unit cell parameters using the Le Bail refinement method.

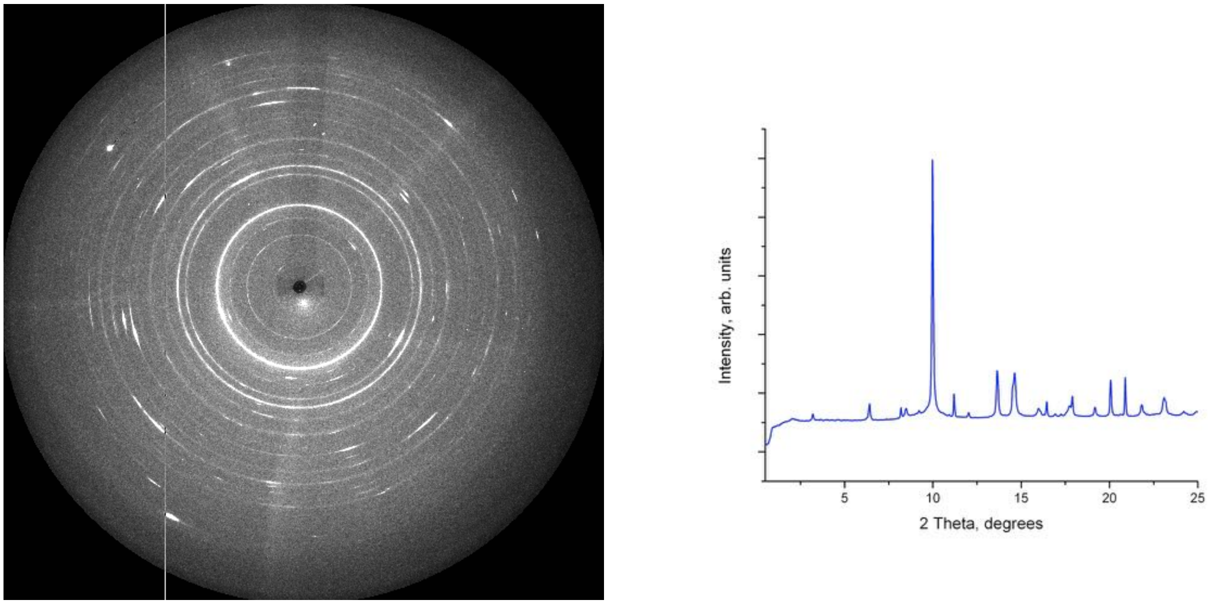

Figure 2.14: 2D powder diffraction image collected by the MAR3450 detector and the 1D spectrum, intensity verses 2θ, after the FIT2D integration.

2.7 Le Bail refinement method

Le Bail refinement exploits the Rietveld decomposition formula,

$$I_K = \sum_j \{w_{j,K} \cdot S_K^2 \cdot y_j(obs)/y_j(calc)\} \tag{2.3}$$

where $w_{j,K}$ is a measure of the contribution of the Bragg peak at position $2\theta_K$ to the diffraction profile y_j at position $2\theta_j$, S_K^2 is the structure factor calculated from the atomic coordinates, and $y_j(calc)$ is the calculated total intensity profile at position $2\theta_j$ from all contributing Bragg peaks. The sum is over all $y_j(obs)$ that can theoretically contribute to the intensity I_K. This equation approximates the contribution of the intensity profile of the Bragg peak at $2\theta_K$ to the total observed intensity profile [32, 33]. In a Rietveld refinement this formula is used to decompose the observed intensity profile into "observed" intensity profiles from individual Bragg peaks based on the structure factor, S_K^2, calculated from the atomic coordinates. These "observed" intensities are then used to calculate statistical R values for the least-squares refinements.

Armel Le Bail saw that this decomposition formula could alternatively be used in an iterative fashion to approximate the structure factor S_K^2 when the atomic positions are unknown [33, 34]. Initially, all S_K^2 are set to an arbitrary equal value and equation 2.3 gives I_K values for each Bragg peak, which are then used to determine new S_K values. The unit cell parameters are refined by least-squares using the traditional Rietveld method [32]. Then new S_K values are calculated using the decomposition formula to use for the next least-squares refinement of the unit cell parameters. The process is repeated until a good fit is obtained (i.e. low R values).

2.7.1 Special cases

Following are two example cases to illustrate how the Rietveld decomposition formula is used to determine S_k values for a Le Bail fit.

No peak overlap

In the case that there is no peak overlap, only one Bragg peak contributes to an observed intensity. Then,

$$y_j(calc) = w_{j,K} \cdot S_K^2. \tag{2.4}$$

Plugging this into equation 2.3 gives

$$I_K = \sum_j y_j(obs). \tag{2.5}$$

All of the observed intensity profile is attributed to the single Bragg peak. The new S_K is then set so that the intensity of the peak fit matches the intensity of the observed peak.

Perfect peak overlap

Consider the case where two Bragg peaks perfectly overlap, $2\theta_{K1} = 2\theta_{K2}$. Then,

$$y_j(calc) = w_{j,K1} \cdot S^2_{K1} + w_{j,K2} \cdot S^2_{K2}. \tag{2.6}$$

For the Le Bail starting conditions we set $S^2_{K1} = S^2_{K2} = 1$. Using the approximation that $w_{j,K}$ depends only on 2θ and calculating the decomposed intensities for each Bragg peak we find,

$$I_{K1} = \sum_j 1/2 \cdot y_j(obs) \tag{2.7}$$

and

$$I_{K2} = \sum_j 1/2 \cdot y_j(obs). \tag{2.8}$$

Thus, for two perfectly overlapping Bragg peaks the observed intensity is attributed equally to both Bragg peaks. If, however, the starting S^2_K values where not equal (e.g. in the Von Dreele modification available in GSAS [35]) the resulting I_K values for overlapping peaks would maintain the same ratio as the initial S^2_K values.

When two Bragg peaks are near each other but not perfectly overlapping it may take several Le Bail iterations without refining any cell parameters to find the right relative intensities for each peak that result in a good fit to the observed intensity. After a good intensity profile match is achieved one can proceed with a least-squares regression on the unit cell parameters and any other profile parameters that will be varied. Of course, parameters that affect the structure factor should not be refined. After the regression fit, new S^2_K values are determined by equation 2.3 which are used for the next iteration.

2.7.2 Le Bail method in GSAS

Le Bail refinement was done using the GSAS program [35,36]. We fit our spectra to $R\bar{3}m$ for the α and the β phases and $P6_522$ for the γ phase and used the unit cell parameters measured by Popovic *et al.* [5] for each phase. Once an appropriate space group and initial unit cell parameters are decided on and entered into the program, the refinement process begins with an appropriate fit for the background. I did this using the BKGEDIT feature in the GSAS GUI which fits a Chebyschev polynomial to selected fixed points. POWPREF is then run to calculate the initial model of the intensity profile using $S_K^2 = 1$ for all Bragg peaks. Then GENLES is run 2-3 times with no parameters selected to refine. Each time GENLES is run it decomposes the observed intensity profile according to equation 2.3 and determines the S_K values to use in the next iterative step. Next, I select parameters to refine and run GENLES, which performs the least-squares regression and determines new S_K values for the next GENLES cycle. Each time I select a parameter to refine I run GENLES 2-3 times and I set it to complete the maximum number of cycles, 999 (a total of 2997 Le Bail iterations). I only refine one parameter at a time in the following sequence: the unit cell, the zero point of the detector, the full width at half maximum (GW), ending by again refining the unit cell. This Le Bail refinement method determines the hexagonal unit cell parameters, a and c, and therefore the volume of the hexagonal unit cell which can be used to determine an EOS.

2.8 Birch-Murnaghan equation of state (EOS)

Using the unit cell volumes determined by the Le Bail refinement method I can find the equation of state parameters (e.g., the bulk modulus) for the different In_2Se_3 phases. Volume verses pressure data are fit to the third-order Birch-Murnaghan EOS.

The Birch-Murnaghan EOS is a generalization of the Murnaghan EOS. In the Murnaghan EOS the bulk modulus is assumed to depend linearly on pressure [37]. Birch extended the Murnaghan EOS by expressing the internal strain contribution to the crystal system's Helmholtz free energy as a Taylor series in compression, f [38]. From finite strain theory (see ref. [39]):

$$\frac{V}{V_0} = (1+2f)^{-\frac{3}{2}}, \tag{2.9}$$

where V_0 is the volume at ambient pressure.

Following the derivation in Poirier [39] for the third-order Birch-Murnaghan EOS we will expand the Helmholtz free energy F in powers of the compression, f, to the third order,

$$F = af^2 + bf^3. \tag{2.10}$$

Note that, for infinitesimal strains, the elastic strain energy is quadratic and that we can set the strain energy to be zero for $f = 0$. Pressure is given by

$$P = -\left(\frac{\partial F}{\partial V}\right)_T = -\left(\frac{\partial F}{\partial f}\right)_T \frac{df}{dV}. \tag{2.11}$$

Differentiating equation 2.10 yields:

$$\frac{\partial F}{\partial f} = 2af + 3bf^2. \tag{2.12}$$

Differentiating equation 2.9, we find

$$\frac{\partial f}{\partial V} = -\frac{1}{3V_0}(1+2f)^{\frac{5}{2}}. \tag{2.13}$$

Plugging equations 2.12 and 2.13 into equation 2.11, we get:

$$P = \frac{2a}{3V_0} f \left(1 + \frac{3b}{2a} f^2\right) (1+2f)^{\frac{5}{2}}. \tag{2.14}$$

Using the zero pressure conditions that at $P = 0$, $f = 0$, $K = K_0$, and $K' = K_0'$, we can find a and b in terms of K_0 and K_0'. From equation 2.9 we can get an expression for f in terms of $\frac{V}{V_0}$. The resulting $P(V)$ expression is the third-order Birch-Murnaghan EOS:

$$P = \frac{3}{2}K_0\left[\left(\frac{V_0}{V}\right)^{\frac{7}{3}} - \left(\frac{V_0}{V}\right)^{\frac{5}{3}}\right] \times \left\{1 + \frac{3}{4}(K_0' - 4)\left[\left(\frac{V_0}{V}\right)^{\frac{2}{3}} - 1\right]\right\}. \tag{2.15}$$

A least-squares fit of the volume verses pressure data to the third-order Birch-Murnaghan EOS gives the atmospheric volume (V_0), bulk modulus (K_0) and the pressure derivative of the bulk modulus (K_0').

Chapter 3

High-pressure α-to-β phase transformation

In this chapter we discuss the pressure induced transition of α-In_2Se_3 to β-In_2Se_3.

3.1 Experimental Methods

Samples of α phase In_2Se_3 powder (99.99%), purchased from Alfa Aesar, were loaded into a piston-cylinder diamond-anvil cell. A stainless steel gasket was pre-indented for the 600 μm or 1000 μm culet diamonds to a thickness of $\sim$50 μm. A 300 μm diameter hole was drilled in the center of the indentation and the sample was loaded into the hole along with a pressure transmitting medium of either a 4:1 methanol-ethanol mixture or mineral oil. The 4:1 methanol-ethanol mixture is known to provide hydrostatic conditions up to 10 GPa [21]. Mineral oil is hydrostatic up to 4 GPa, as determined by the width and splitting of the ruby lines [22]. Ruby microspheres were inserted for *in situ* pressure measurements. The pressure was measured before and after each XRD spectrum by the R_1 and R_2 peak shifts using the Mao scale [26] and the average used as the experimental pressure value with estimated

---

Portions of this chapter were published as: A. R. Rasmussen, S. T. Teklemichael, E. Mafi, Y. Gu, and M. D. McCluskey. *Pressure-induced phase transformation of In_2Se_3*, Appl. Phys. Lett. **102** (2013), p. 062105.

precision of 0.1 GPa. The opening of the DAC limited the maximum 2-theta value to 15-20°.

XRD experiments were performed at the Advanced Light Source (ALS), Lawrence Berkeley National Laboratory (LBNL), beamline 12.2.2 (Ref. [30]) and the Cornell High Energy Synchrotron Source (CHESS), Cornell University, beamline B2. Samples were loaded to a pressure of ~0.2 GPa and spectra were taken for both compression and decompression. All experiments were done at ambient temperature. Spectra were collected at wavelengths between 0.4859-0.6199 Å by a high resolution MAR3450 plate detector. Diffraction images were integrated using the FIT2D program.

Volume and lattice parameters were obtained through Le Bail fitting using the GSAS program [35, 36]. A Raman study assigned the α phase to the rhombohedral $R3m$ space group (No. 160) [40]. However, our XRD spectra for the α phase are in agreement with those of Popović *et al.* [5], who assigned peaks to the $R\bar{3}m$ space group (No. 166). For consistency, we assigned the peaks of the α and β phase to $R\bar{3}m$. Since the Le Bail fitting only extracts the a and c parameters of the rhombohedral unit cell, and not the atomic positions, our results do not rule out $R3m$ for the α phase. Pressure-volume data were fit to the third-order Birch-Murnaghan equation of state (EOS) [38, 39],

$$P = \frac{3}{2}K_0\left[\left(\frac{V_0}{V}\right)^{\frac{7}{3}} - \left(\frac{V_0}{V}\right)^{\frac{5}{3}}\right] \times \left\{1 + \frac{3}{4}(K_0' - 4)\left[\left(\frac{V_0}{V}\right)^{\frac{2}{3}} - 1\right]\right\} \tag{3.1}$$

where P is the pressure, V_0 is the lattice volume at ambient pressure, K_0 is the bulk modulus at ambient pressure, and K_0' is the pressure derivative of bulk modulus at ambient pressure.

3.2 Results and Discussion

Figure 3.1 shows XRD spectra for In_2Se_3 at pressures of 0.4 GPa, 0.7 GPa, and 1.2 GPa. The intensity of the (104) peak decreased, while the intensity of the (105) peak increased, at 0.7 GPa. In addition, a discontinuous drop in both the a and c lattice parameters, obtained from the GSAS Le Bail fitting, was observed at 0.7 GPa. From the splitting of the (006)

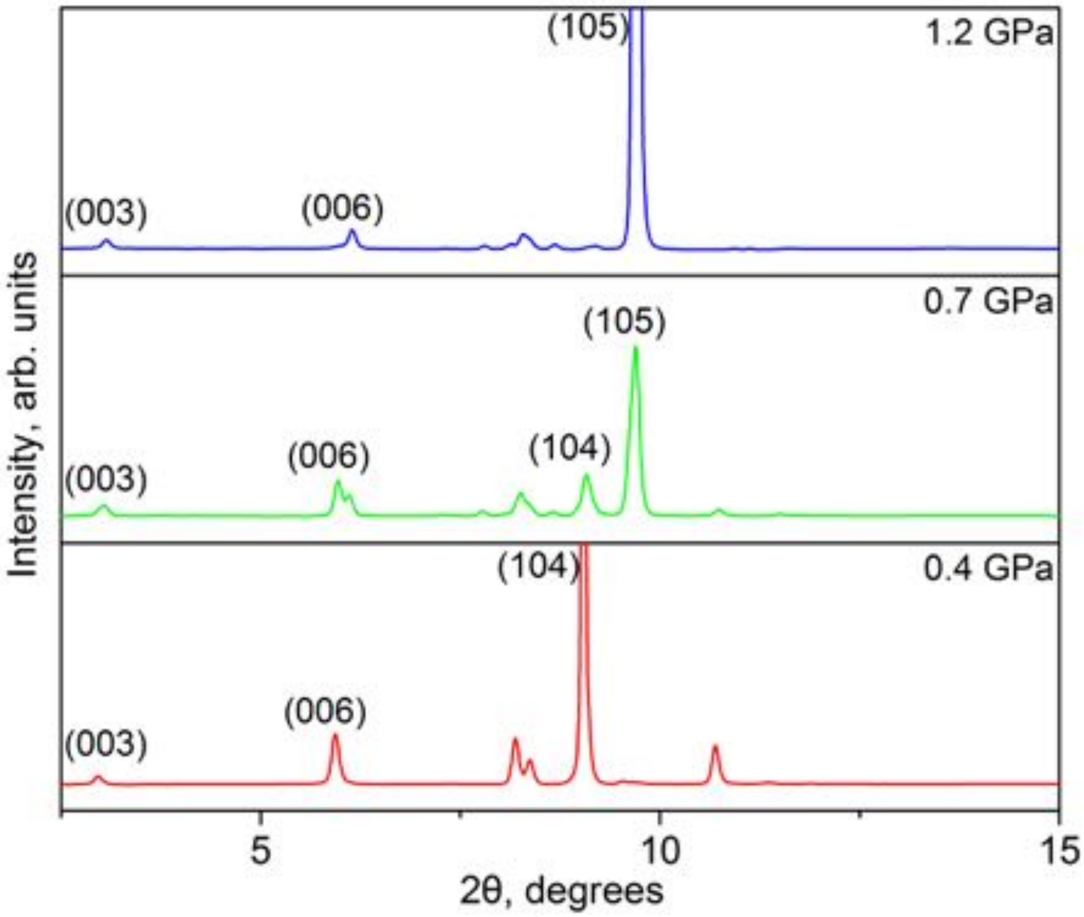

Figure 3.1: Integrated XRD spectra ($\lambda = 0.4959$ Å) for In_2Se_3 at three different pressures. The 0.4 GPa spectrum shows that the sample is in the α phase and the 1.2 GPa spectrum shows that the sample is in the β phase. The 0.7 GPa spectrum shows a mixed α-β phase, indicated by the splitting of the (006) peak and the presence of both the (104) and (105) peaks.

peak, in spectra that showed a mixture of the two phases, we find the c lattice parameter drops by $\sim 2\%$. The change in intensities and the drop in lattice constants are consistent with the $\alpha \rightarrow \beta$ phase transition previously observed at elevated temperatures [5]. The strong (105) peak persisted upon decompression down to ambient pressure (figure 3.2) and the lattice parameters at ambient pressure remained lower than the ambient α phase lattice parameters. These observations indicate the persistence of the β phase upon decompression to ambient pressure.

Pressure-volume data for the α and β phases are shown in figure 3.4 for both compression

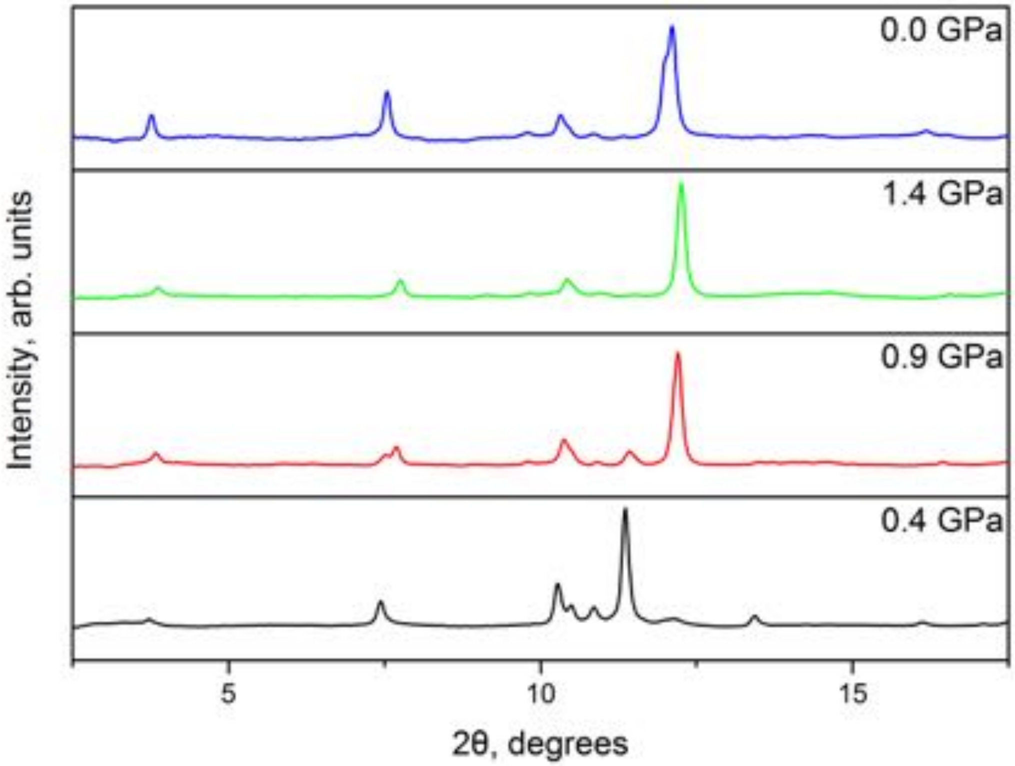

Figure 3.2: Integrated XRD spectra (λ = 0.6199 Å) for In_2Se_3 at elevated pressures and after decompression to atmospheric pressure. The 0.0 GPa spectrum shows that the sample remains in the β phase after decompression.

and decompression. It can be seen that, at ambient pressure, the β phase is denser than the α phase. The α phase and β phase data were fitted to the Birch-Murnaghan EOS and the bulk modulus for each phase was obtained. The ambient pressure derivative of the bulk modulus and the ambient lattice volume were held fixed at $K_0' = 4$ and $V_0 = 403.5$ Å for the α phase fitting. From this fit, the α phase has a zero pressure bulk modulus of $K_0 = 22 \pm 5$ GPa. All parameters were allowed to vary for the β phase fitting. The β phase has an ambient pressure bulk modulus of $K_0 = 29 \pm 2$ GPa, ambient pressure derivative of the bulk modulus of $K_0' = 6.5 \pm 0.7$, and ambient pressure volume of $V_0 = 389 \pm 1$ Å^3.

Figure 3.5 shows the ratio $r = c/a$ as a function of pressure. The β phase shows highly

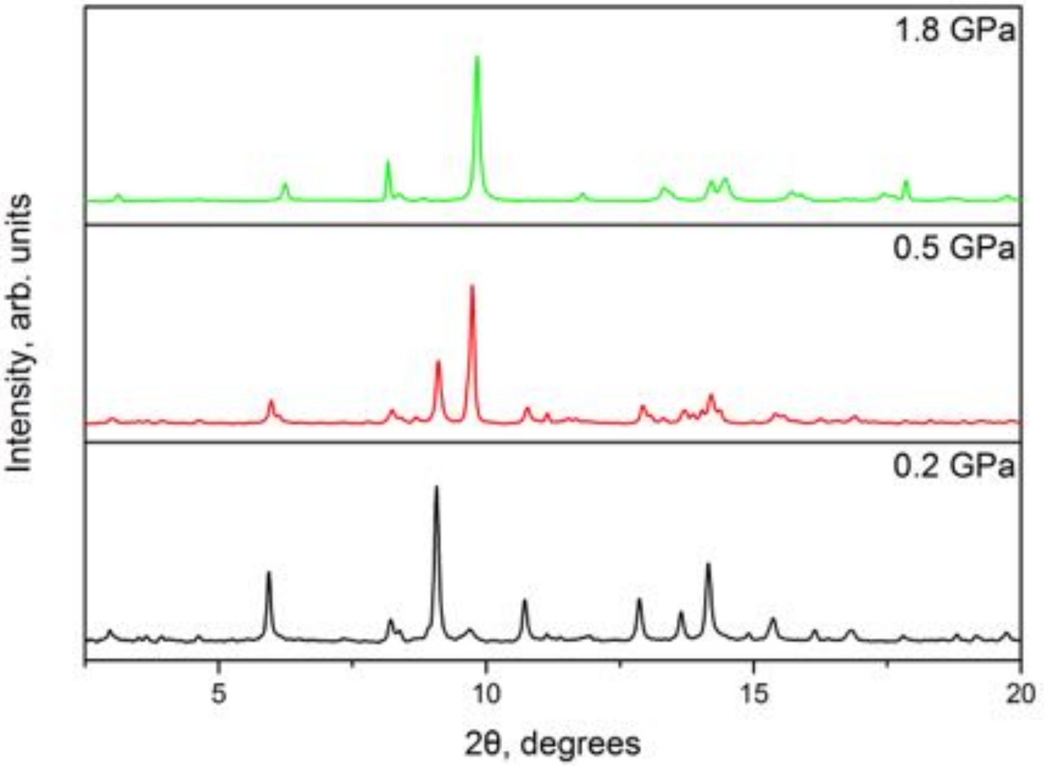

Figure 3.3: Integrated XRD spectra ($\lambda = 0.4959$ Å) for In_2Se_3 under compression.

anisotropic compression at low pressures. The ratio has a nonlinear dependence on pressure:

$$r = (6.68 \pm 0.03) + (0.38 \pm 0.02)\exp[-(0.23 \pm 0.04)P] \tag{3.2}$$

where P is the pressure in GPa. In addition, we found the value for r at ambient pressure for the β phase is smaller than that for the α phase.

To complement the XRD experiments, we performed confocal Raman spectroscopy on our samples with the back-scattering geometry, using a 633 nm He-Ne laser and a Leica optical microscope coupled to a Renishaw InVia spectrometer. In order to avoid optical heating and phase transformation we used the lowest possible optical excitation power of ∼4 mW, which is higher than what was previously used for single-nanowire Raman. The reason we used more power is that the laser was applied to a relatively large amount of bulk

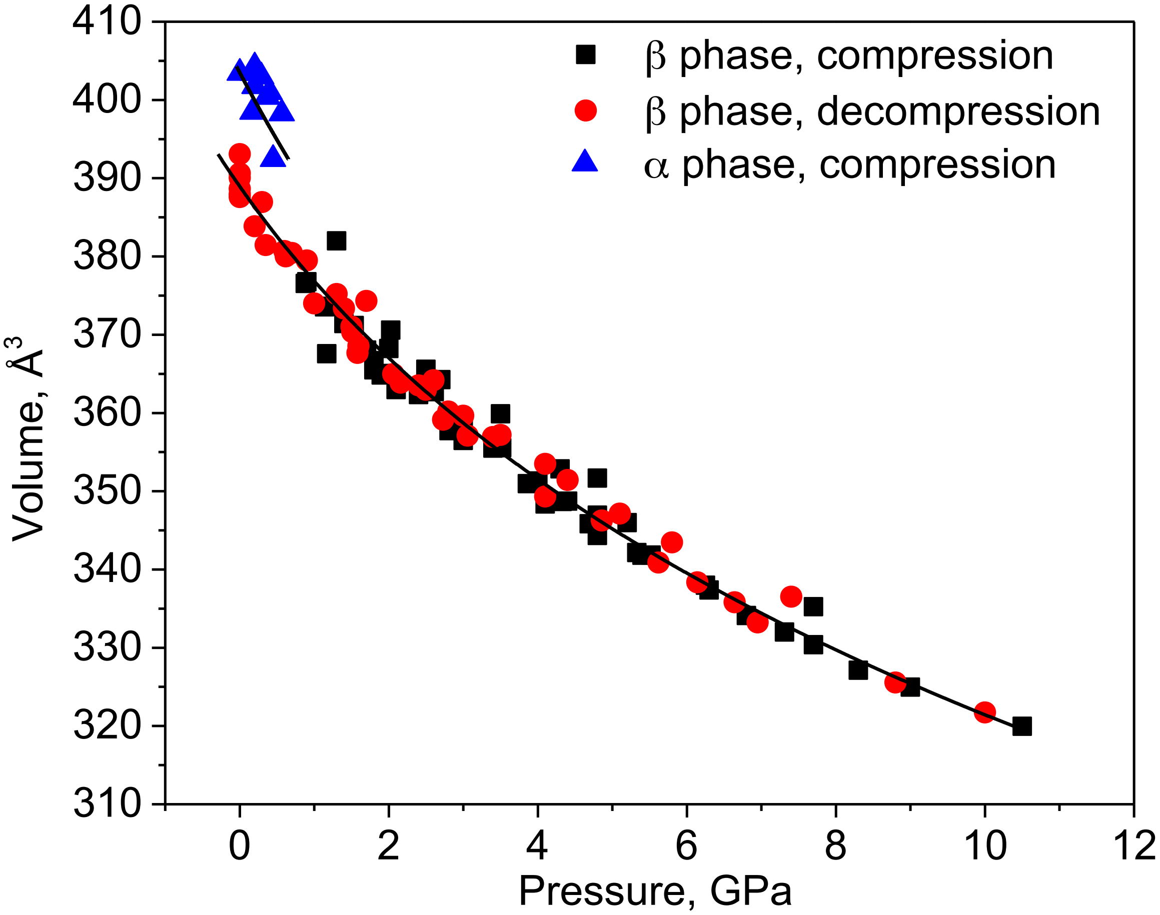

Figure 3.4: P-V data for the α and β phases of In_2Se_3. The triangles indicate α phase compression, the squares indicate the β phase compression, and the circles indicate the β phase decompression. The solid lines are fits to the third-order Birch-Murnaghan EOS.

powder instead of a single nanowire.

The In_2Se_3 powder was loaded and the pressures were measured in the same way as was done for the XRD experiments. The sample was loaded to a pressure of 0.5 GPa and a Raman spectrum was taken. (The higher background level in the high-pressure spectra is due to luminescence from the diamonds.) The sample was then compressed to 0.9 GPa. As shown in figure 3.6(a), there is a notable frequency shift ($\sim$3 cm^{-1}) of the main Raman peak from 0.5 GPa to 0.9 GPa, in addition to substantial broadening. We note that this frequency shift and peak broadening are larger than those between the Raman spectra at ambient pressure and 0.5 GPa. This suggests a phase transformation at a pressure between

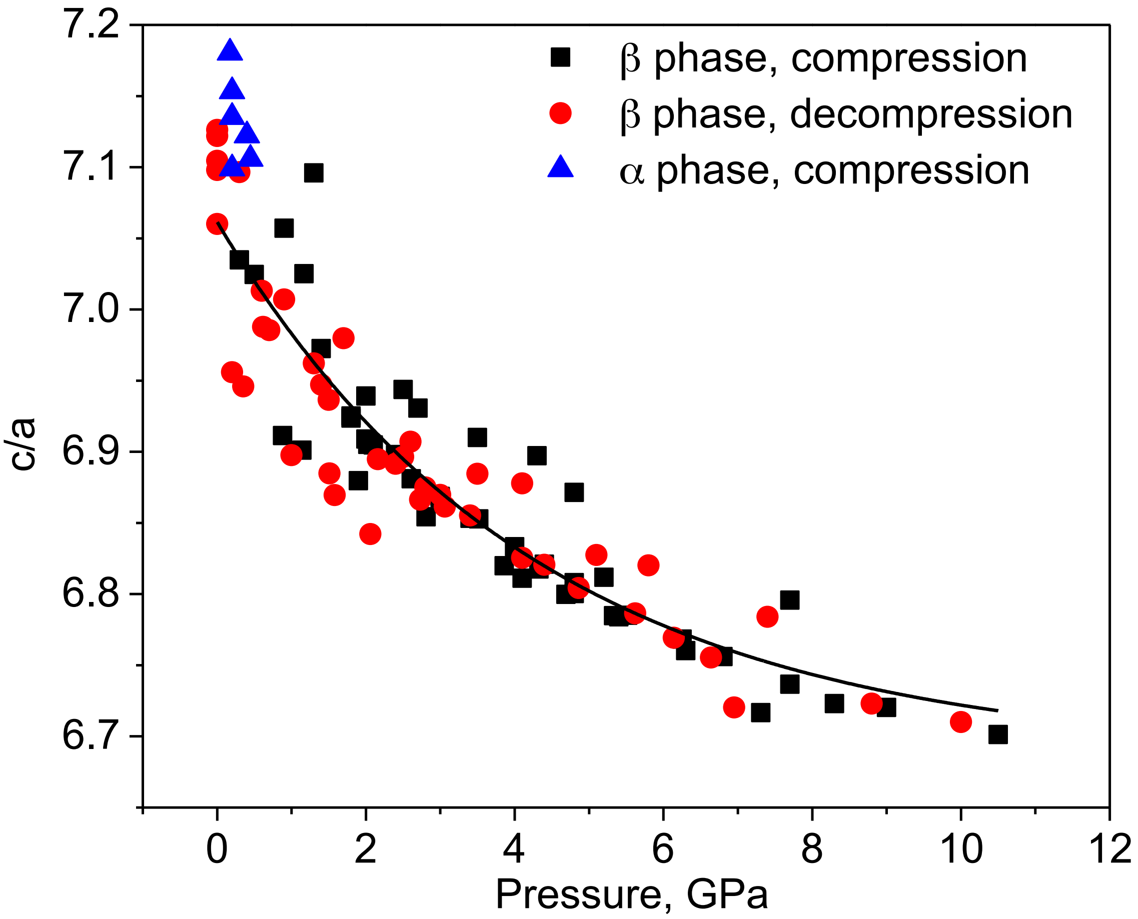

Figure 3.5: Ratio of In_2Se_3 lattice parameters, $r = c/a$, as a function of pressure. The triangles indicate α phase compression, the squares indicate the β phase compression, and the circles indicate the β phase decompression. The solid line is an exponential fit for the β phase data.

0.5 and 0.9 GPa, consistent with the $\alpha \rightarrow \beta$ transformation at 0.7 GPa obtained from XRD.

To verify the Raman assignments, we annealed a sample of the α-In_2Se_3 powder from Alfa Aesar in argon at 948 K for 5 hours, in a sealed silica ampoule. The sample was cooled by quenching the ampoule in room-temperature water. The annealing temperature is sufficient to transform the sample into β-In_2Se_3. As shown in figure 3.6(b), the Raman spectrum of the annealed β-phase powder is similar to that at 0.9 GPa. This confirms the presence of the β phase at 0.9 GPa.

3.3 Conclusions

In conclusion, using XRD we discovered a pressure-induced phase transition in In_2Se_3, from the α to the β phase, at 0.7 GPa. Raman spectroscopy verified this result. The critical pressure is an order of magnitude lower than that for most materials. For example, InSe has a phase transition at 10 GPa, while GeSe has no phase transition up to 13 GPa [41]. Bi_2Te_3 (Refs. [42, 43]) and Sb_2Te_3 (Refs. [44, 45]) undergo phase transitions at 10 and 8 GPa, respectively. Group IV, III-V, and II-VI semiconductors show phase transitions at 2 GPa or higher. We determined the EOS and c/a ratio for the β phase up to 11 GPa. The response to pressure was highly anisotropic with a nonlinear decrease of the c/a ratio. This anisotropy is related to the structure of α and β phase In_2Se_3, in which a-plane layers interact via van der Waals interactions [8]. These relatively weak interactions result in a significant decrease in c/a as pressure is applied.

Following our discovery of the α to β transition , Ke *et al.* [13] reported that the transition occurs at a critical pressure of 0.8 GPa and determined the phase transition is due to a pressure induced shear shift between neighboring layers (see figure 1.2). Zhao and Yang [12], however, report a transition from the α phase structure into an intermediate phase with a monoclinic structure around 0.8 GPa before transforming into the β phase. In addition they found that In_2Se_3 begins to transform from the layered β phase into a body center cubic structure at around 32 GPa, and completes the phase transition around 50 GPa.

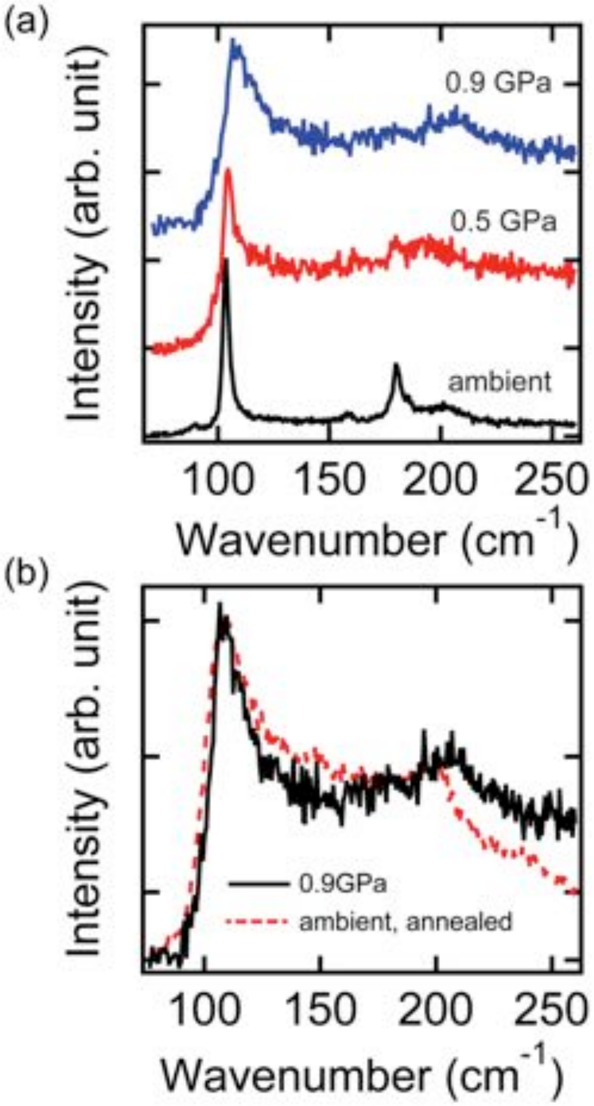

Figure 3.6: Raman spectra of In_2Se_3. (a) Ambient In_2Se_3 (α phase) and In_2Se_3 under pressure. The frequency shift and broadening is consistent with the $\alpha \rightarrow \beta$ transformation at 0.7 GPa. (b) Comparison between β-In_2Se_3 (produced by annealing) and the 0.9 GPa spectrum. The similarity between the spectra confirms the presence of the β phase at 0.9 GPa.

Chapter 4

High-pressure γ-to-β phase transformation

This chapter discusses the results of x-ray diffraction (XRD) experiments performed on In_2Se_3 bulk powder and nanowires initially in the metastable γ phase.

4.1 Experimental Methods

γ phase In_2Se_3 bulk powder was obtained by annealing α phase In_2Se_3 powder (99.99%), purchased from Alfa Aesar, at temperatures just above the γ to β transition temperature of 520 °C [5] for 24 or 48 hr in a sealed ampoule filled with ∼0.5 atm Ar gas. The nanowire samples were grown by a catalyzed vapor deposition method via vapor-liquid-solid (VLS) growth using 100 nm gold colloids. As-grown nanowire samples are a mixture of the γ and β phases. Some of the nanowire samples were annealed for 24-48 hours at ∼520 °C, transforming the β phase components to the γ phase.

Samples were loaded into a piston-cylinder diamond anvil cell with 600 μm or 1000 μm culet diamonds. A stainless steel gasket was pre-indented to ∼50 μm thick and a 300 μm or

---

Portions of this chapter have been submitted for publication as: A. R. Rasmussen, E. Mafi, W. Zhu, Y. Gu, and M. D. McCluskey. *High pressure γ-to-β phase transition in bulk and nanocrystalline In_2Se_3*, (2016).

500 μm diameter hole was drilled for the 600 μm and 1000 μm culet sizes, respectively. The sample, a pressure-transmitting medium of 4:1 methanol-ethanol mixture or mineral oil, and ruby microspheres for *in situ* pressure measurements were loaded into the hole [20]. The pressure was measured by the R_1 and R_2 peak shifts using the Mao scale [26] before and after each XRD spectrum, with the average used as the experimental pressure value. The maximum 2θ value was limited to 20° by the opening of the DAC.

XRD experiments were performed at the Advanced Light Source (ALS), Lawrence Berkeley National Laboratory (LBNL), beamline 12.2.2 [30] and Cornell High Energy Synchrotron Source (CHESS), beamline B2. Spectra were collected by a MAR3450 plate detector at the wavelengths of 0.4959 Å at ALS and 0.4859 Å at CHESS. Starting at initial pressures of 0.4-2.1 GPa, spectra were taken for both compression and decompression at ambient temperature.

Diffraction images were integrated using the FIT2D program [31] and lattice parameters were obtained using the GSAS program through the Le Bail fitting method [35, 36]. We assigned the peaks of the γ phase to $P6_522$ and the β phase to $R\bar{3}m$.

4.2 Results and Discussion

XRD spectra for an annealed In_2Se_3 bulk powder sample at pressures of 2.3 GPa, 2.8 GPa, and 3.1 GPa are shown in figure 4.1. At 2.3 GPa, the sample is in the γ phase. When pressure is increased, (003), (006) and (105) peaks appear, indicating a transition into the β phase. From multiple samples, we determined that the β and γ phases coexist in a mixed phase state above 2.8 GPa and fully transitions to the β phase above 3.2 GPa (see figures 4.2 and 4.3). The samples remained in the β phase upon decompression to ambient pressure. The Le Bail refinement results for the γ phase and the β phase are shown in figure 4.4.

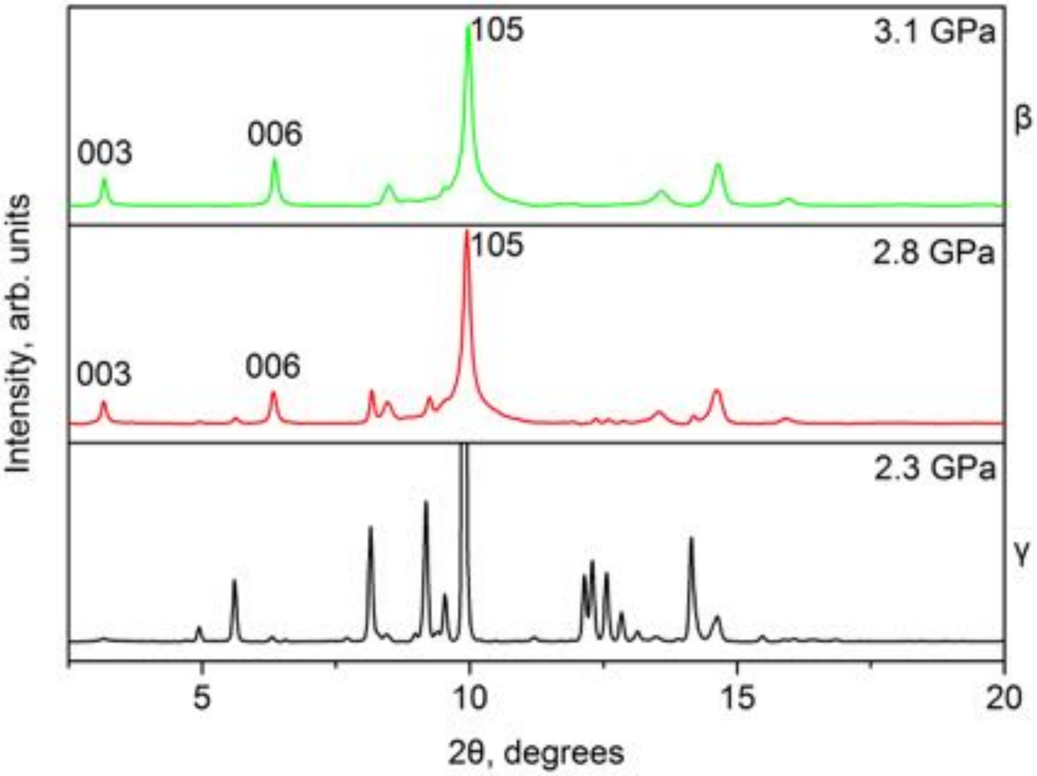

Figure 4.1: Integrated XRD spectra for bulk powder In_2Se_3 initially in the γ phase at 2.3 GPa, in a mixed γ-β phase 2.8 GPa, and in the β phase 3.1 GPa. The appearance of the (003), (006), and (105) peaks as the pressure increases indicates the transition into the β phase.

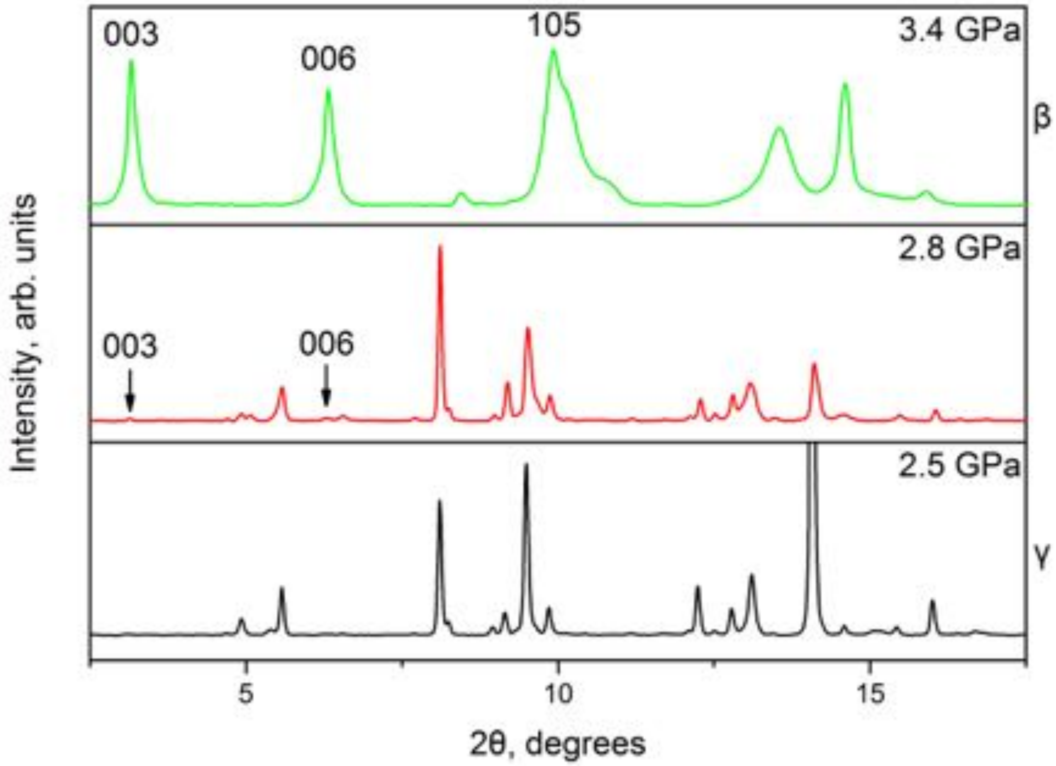

Figure 4.2: Integrated XRD spectra for bulk powder In_2Se_3 at 2.5 GPa, 2.8 GPa, and 3.4 GPa, showing the γ to β transition.

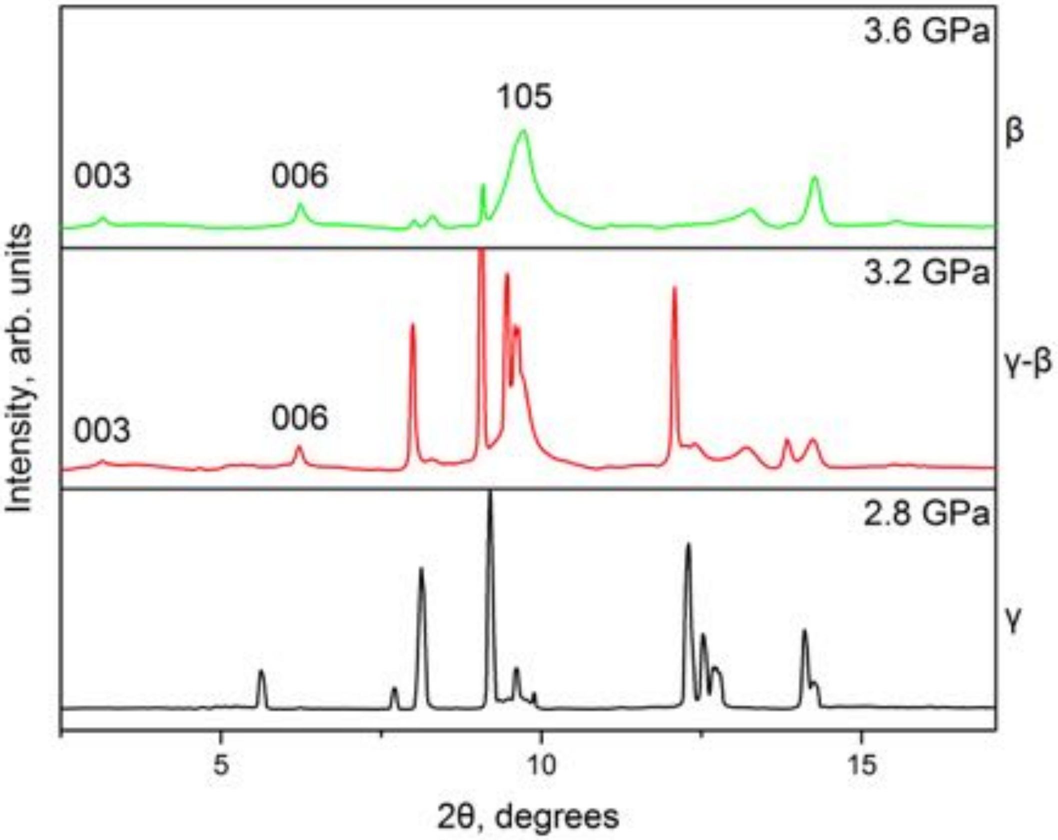

Figure 4.3: Integrated XRD spectra for bulk powder In_2Se_3 at 2.8 GPa, 3.2 GPa, and 3.6 GPa, showing the γ to β transition.

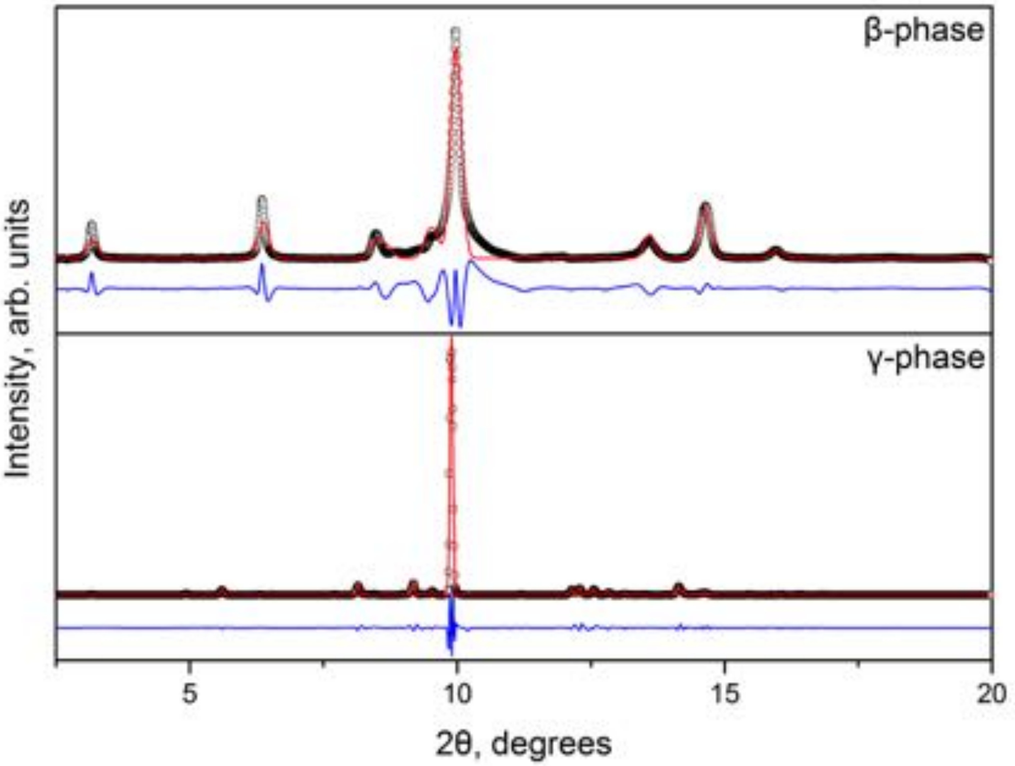

Figure 4.4: Le Bail refinements for the γ phase ($P6_522$ space group) at 2.3 GPa and the β phase ($R\bar{3}m$ space group) at 3.1 GPa. The open circles and the solid lines are the experimental and fitted data. The lower lines represent the residual intensities.

Figure 4.5 shows XRD spectra for an nanowire sample (100 nm diameters) at 3.1 GPa, 3.4 GPa, and 3.8 GPa. At 3.1 GPa, the XRD spectrum shows the nanowire sample is still in the γ phase. The 3.4 GPa spectrum shows the sample is in a mixed phase and at 3.8 GPa the sample is fully in the β phase. From multiple nanowire samples we find that the transition to the mixed phase state occurs at 3.2 GPa and fully transitions into the β phase by 3.7 GPa (see figs. 4.6, 4.7, 4.8). These values are 0.4 GPa and 0.5 GPa higher than in the bulk, respectively. It is typical in semiconductors for nanocrystaline samples to exhibit transitions at higher pressures than in bulk samples [46]. After transitioning to the β phase, we see peak broadening in both the bulk and nano samples. This may suggest that there is a decrease in the average domain size of the crystallites. Figure 4.9 shows the 2D Mar3450 images corresponding to the spectra shown in figure 4.1. Note that the β rings are very blotchy.

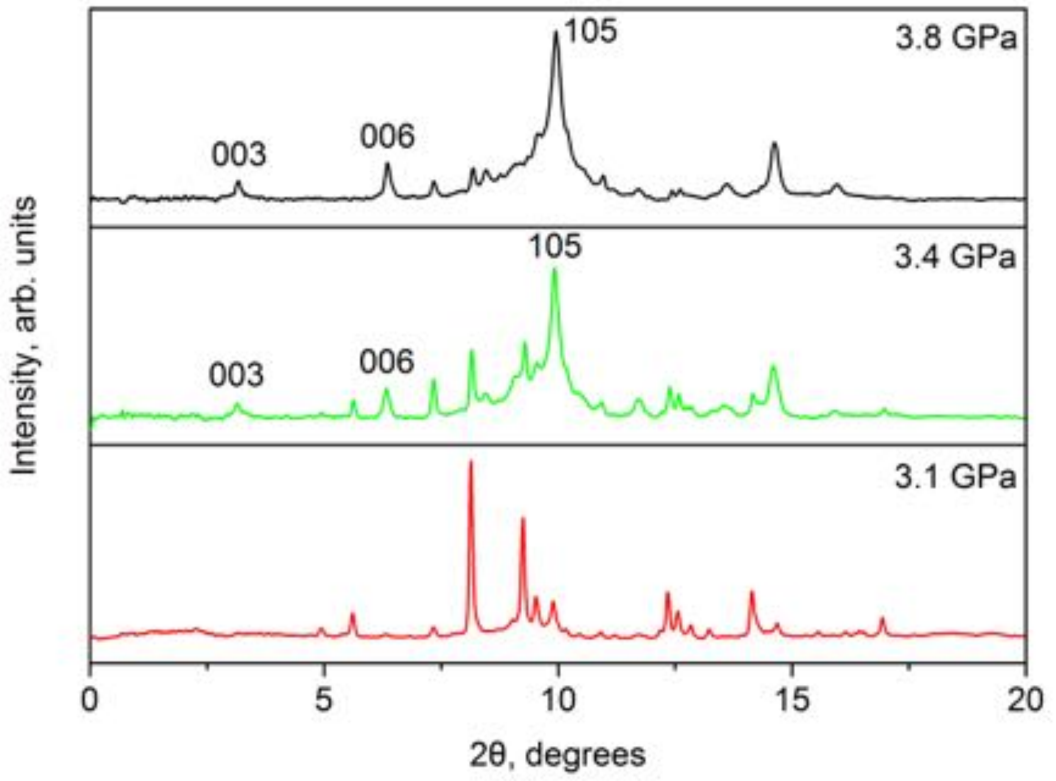

Figure 4.5: Integrated XRD spectra for 100 nm diamerter In_2Se_3 nanowires (as grown). The 3.1 GPa spectrum shows the nanowire sample is in the γ phase. The 3.4 GPa spectrum shows the sample in a γ-β mixed phase. At 3.8 GPa the sample is in the β phase.

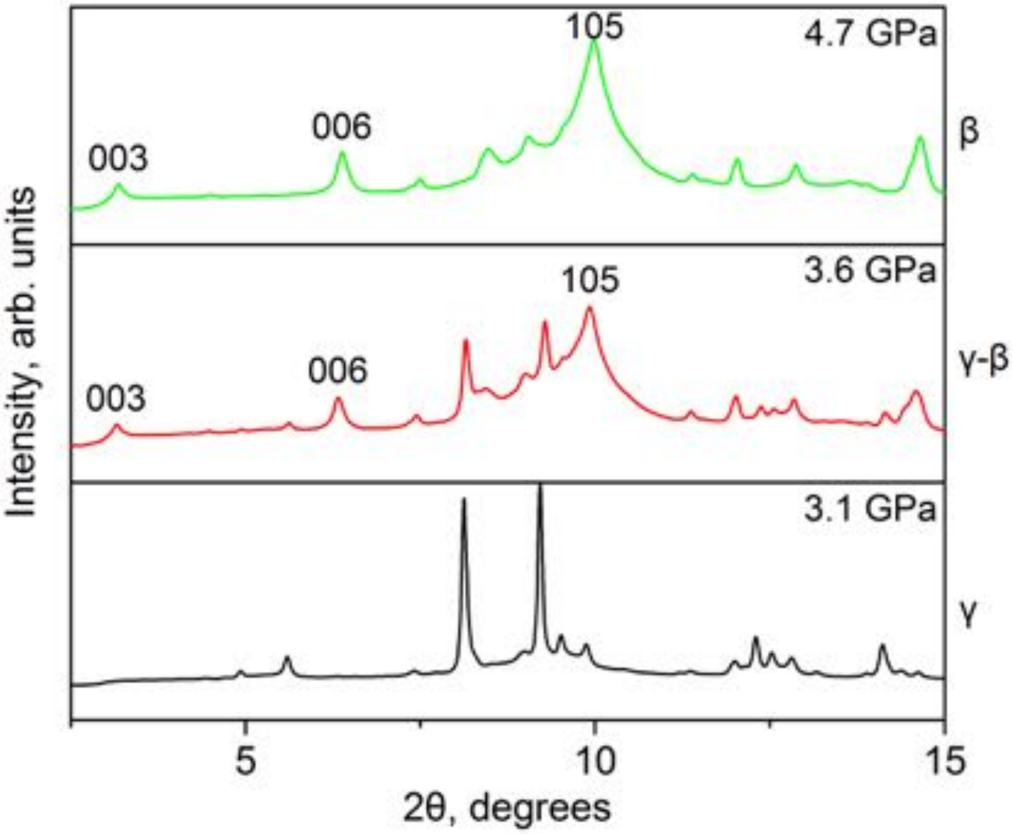

Figure 4.6: Integrated XRD spectra for 100 nm diameter In_2Se_3 nanowires (annealed) showing the γ to β phase transition.

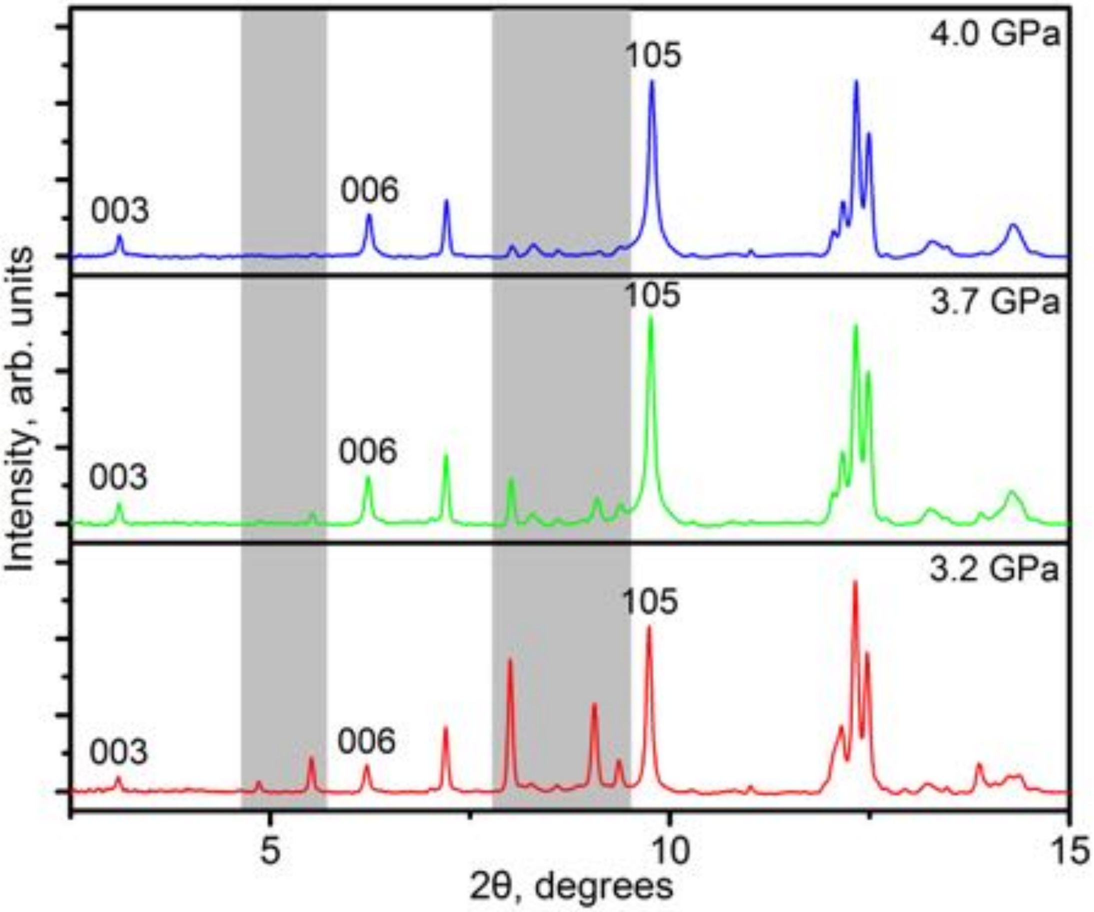

Figure 4.7: Integrated XRD spectra for 20 nm diameter In_2Se_3 nanowires (as grown). The nanowires are initially in a mixed γ-β phase as grown. Under pressure the sample transforms fully into the β phase. Note the decrease in intensity of the highlighted γ peaks.

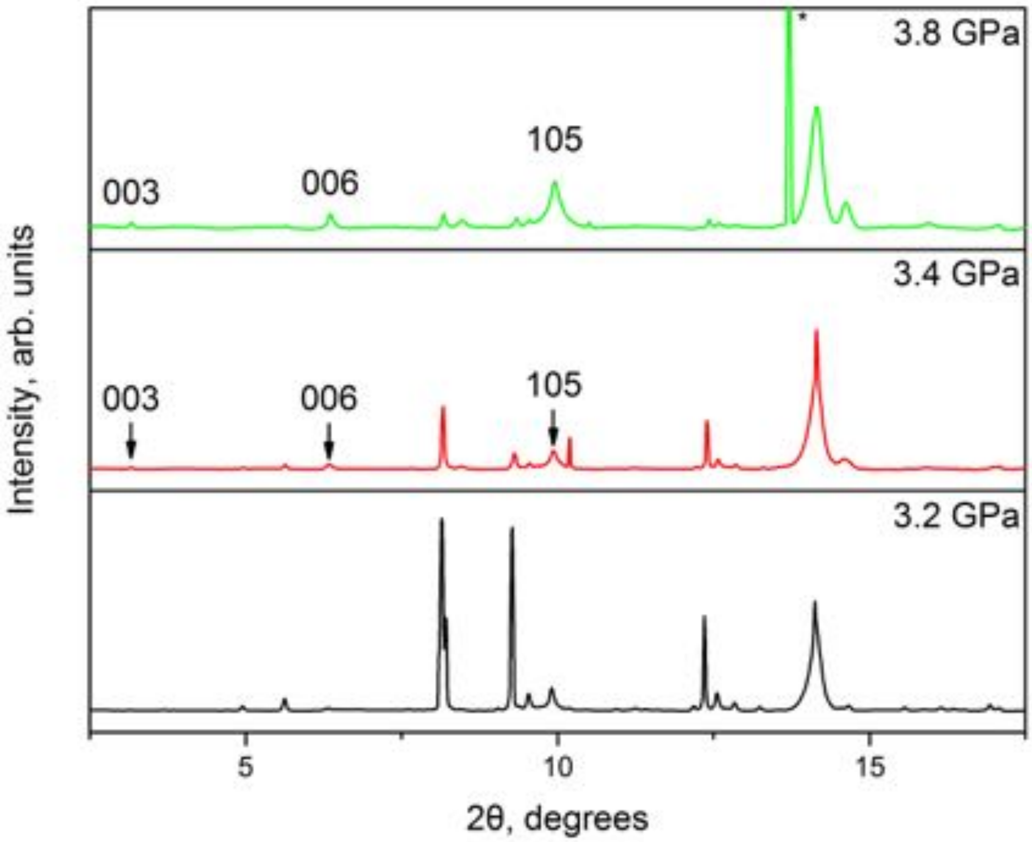

Figure 4.8: Integrated XRD spectra for 5 nm diameter In_2Se_3 nanowires (as grown) showing the γ to β phase transition. * indicates a peak from the stainless steel gasket.

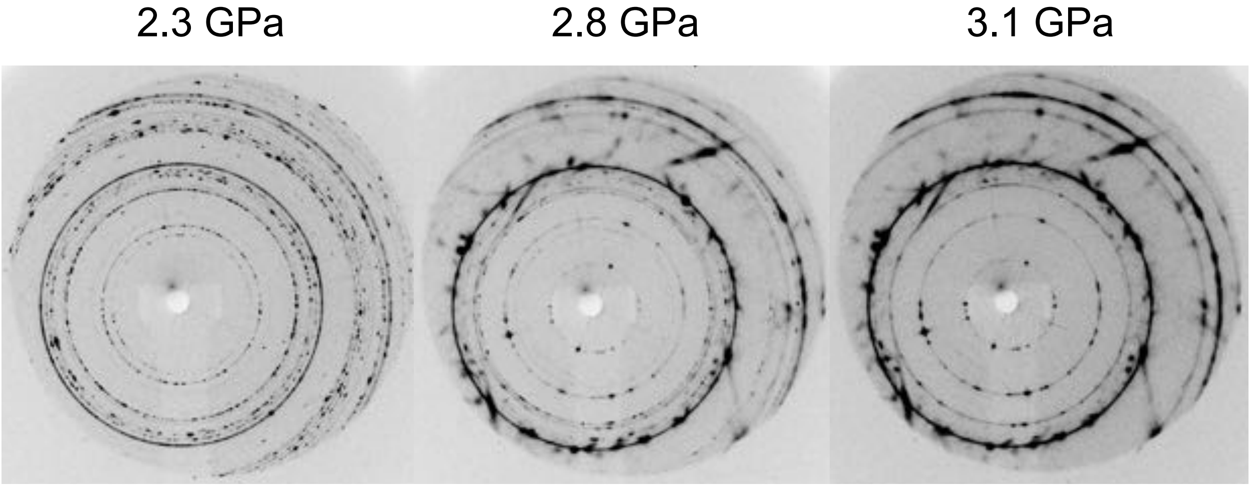

Figure 4.9: 2D Mar3450 images showing the γ to β phase transition in bulk powder samples.

Pressure-volume data for the γ phase are shown in figure 4.10 for the bulk powder samples. The data were fit to the Birch-Murnaghan EOS (Eq. 3.1) and the bulk modulus was obtained. The ambient unit volume was held fixed at $V_0 = 853$ Å^3 and the ambient pressure derivative of the bulk modulus was set to $K' = 4$. The ambient pressure bulk modulus obtained by the EOS fitting for the γ phase is $K_0 = 28.2 \pm 0.7$ GPa, similar to the β phase bulk modulus of 29 ± 2 GPa. The ratio of the γ phase In_2Se_3 lattice parameters, c/a, as a function of pressure is presented in figure 4.11. The slope of the c/a ratio is -0.029 ± 0.005 GPa^{-1}, determined by a linear least-squares fit, revealing that the compression of the γ phase is anisotropic. The decrease in the c/a ratio with pressure for the γ phase is, however, less than half the decrease in the c/a ratio for the β phase over the same pressure range (refer to chapter 3).

To elucidate the experimentally observed pressure-induced phase transformation of In_2Se_3, we performed first-principles calculations using the Vienna ab initio simulation package (VASP) [47] based on density functional theory with projector-augmented wave (PAW) pseudopotentials [48, 49], and the generalized gradient approximation in the parametrization of Perdew, Burke and Enzerhof [50] for the exchange-correlation functional. The plane wave expansions were determined by the default energy cutoffs given by the VASP PAW potentials. Van der Waals interactions were included using the semiempirical DFT-D3 method [51]

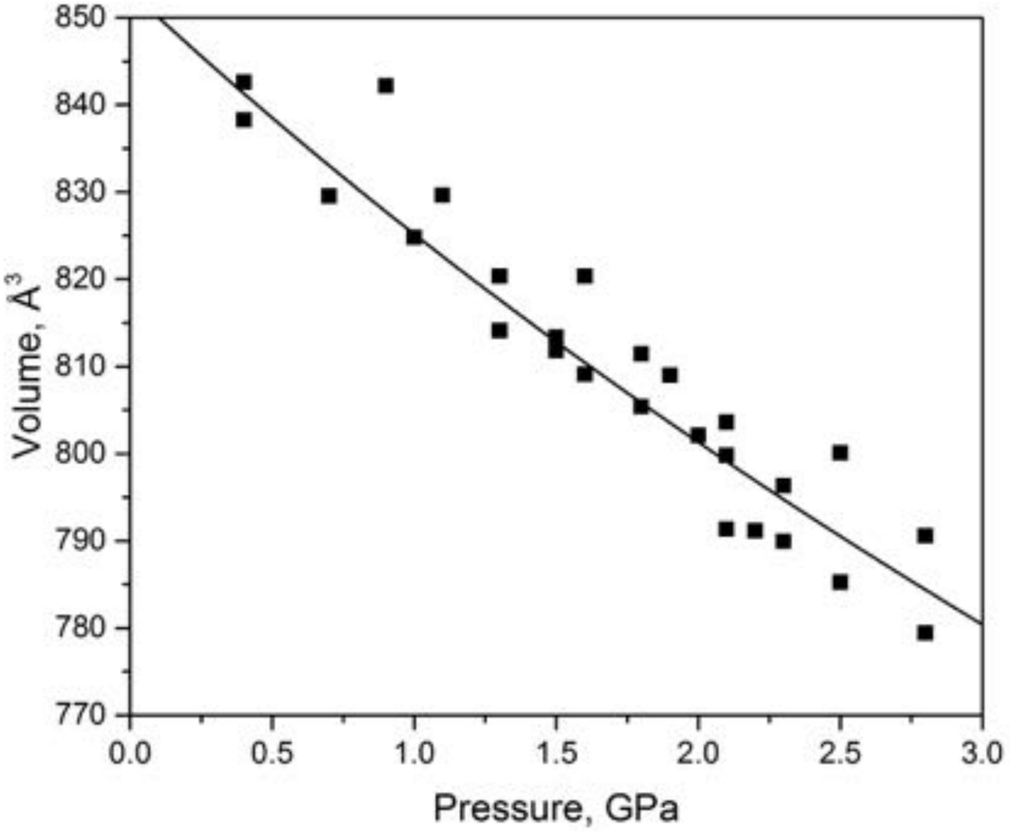

Figure 4.10: P-V data for γ phase In_2Se_3 bulk powder. The solid line is the fit to the Birch-Murnaghan EOS (Eq. 3.1), $K_0 = 28.2 \pm 0.7$ GPa.

with Becke-Jonson damping [52]. All atoms fully relaxed during structural relaxation until the force on each atom was smaller than 0.01 eV/Å.

The optimized bulk structure of the γ-phase In_2Se_3 has a volume of 143 Å^3 per In_2Se_3 molecule, while the β-phase In_2Se_3 has a smaller volume of 128 Å^3 per In_2Se_3 molecule (figure 4.12). In addition, the calculated total energy of the γ-phase is higher than that of the β-phase In_2Se_3, indicating that the γ-phase is a metastable state and the pressure-induced phase transformation is not reversible. The results of these calculations are consistent with the experimental observation.

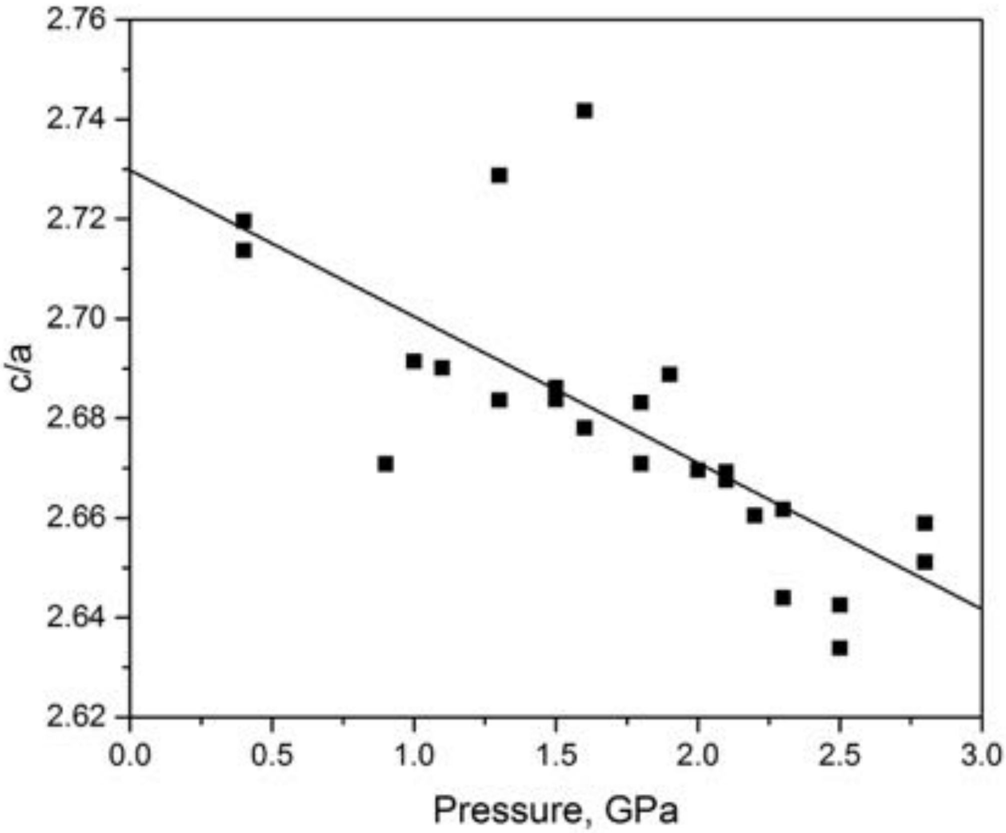

Figure 4.11: Ratio of lattice parameters, c/a, for γ phase In_2Se_3 bulk powder as a function of pressure. The solid line is a linear least-squares fit (slope: -0.029 ± 0.005 GPa^{-1} intercept: 2.73 ± 0.01).

4.3 Conclusions

In conclusion, we discovered a pressure-induced phase transition in bulk powder In_2Se_3 from the metastable γ phase to the high pressure stable β phase between 2.8 GPa and 3.2 GPa. While not a phase transition in the strictest thermodynamic sense, the energy barrier between a metastable and stable state decreases at critical pressures and temperatures, enabling the transition into the thermodynamically stable state to occur over an experimentally observable time scale [16]. In nanowire samples, the phase transition occurs at a higher pressure, between 3.2 GPa and 3.7 GPa. This higher phase transition critical pressure in the nanowires

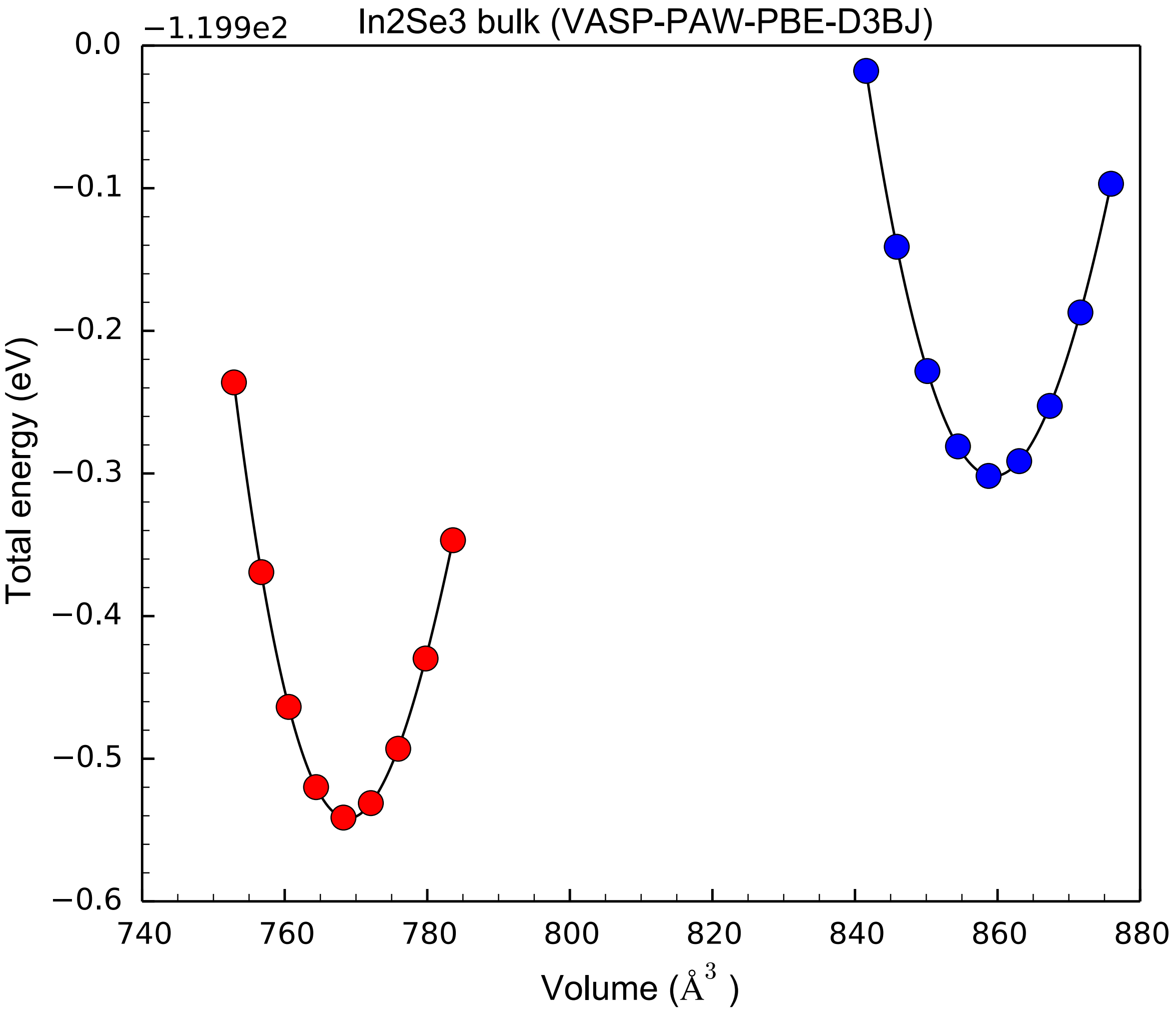

Figure 4.12: VASP-PAW calculated total energy versus unit cell volumes for β-In$_2$Se$_3$ (red/left curve) and γ-In$_2$Se$_3$ (blue/right curve).

is consistent with prior observations in other nanocrystal semiconductors [53, 54] and can be attributed to the large surface-to-volume ratio in nanocrystals [55]. The EOS was determined for the γ phase up to 3 GPa in bulk samples.

Chapter 5

In_2Se_3 at elevated temperatures and pressures

In this chapter we discuss the results of the high-temperature, high-pressure XRD of In_2Se_3. These experiments give insight into the temperature dependence of the high pressure β-phase of In_2Se_3.

5.1 Experimental Methods

5.1.1 Heaters

α phase In_2Se_3 powder (99.99%) samples were loaded into diamond anvil cells with 300 μm culet diamonds and a pre-indented stainless steel gasket with 150 μm drilled holes. The DACs were outfitted with external heating elements for high-temperature experiments. Figure 5.1 shows the two types of external heaters used: a simple resistive band heater that wraps around a DAC and a resistive ceramic heater, manufactured by HeatWave Labs, Inc., installed inside a BX90 DAC surrounding the anvil backing plates. Both heater systems were provided by the 12.2.2 beamline at the ALS [30]. The sample chamber reaches a maximum temperature just over 500 °C with each heater individually, but could be used together to reach higher temperatures. The band heater is powered and controlled by a temperature controller made by Micropyretics Heaters International. The ceramic heater is powered by a TDK 20-20 power supply. When using either heater the DAC stage was cooled by a circulating chilled water system. The temperature of the sample chamber was measured by a thermocouple cemented onto one of the diamond anvils.

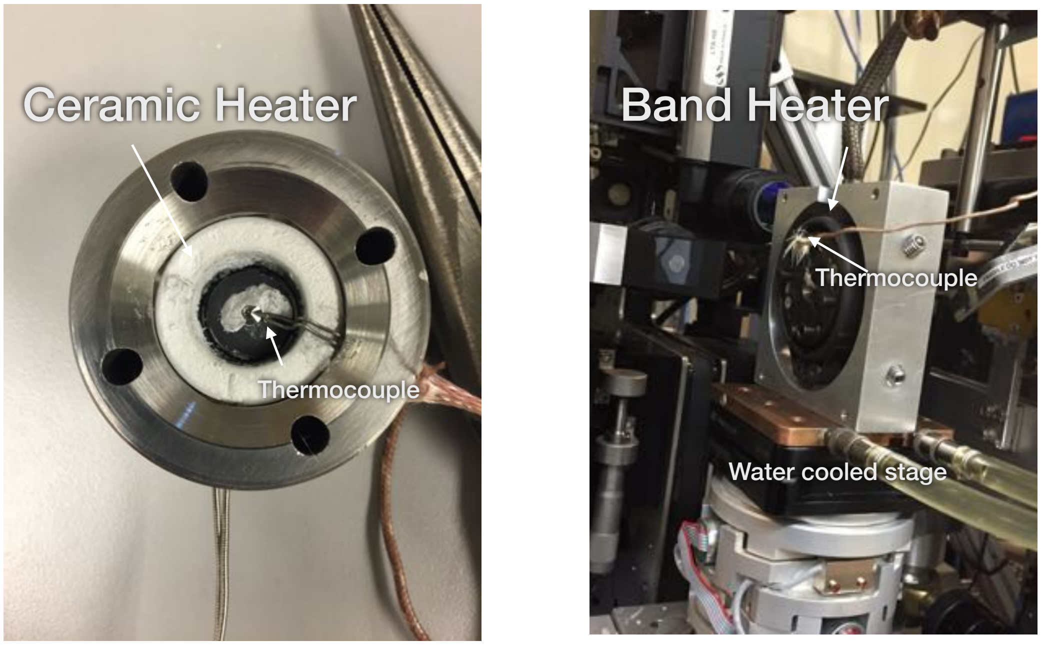

Figure 5.1: Ceramic and band heaters used for high-temperature DAC experiments.

5.1.2 High-temperature Pressure Calibration

Samples were loaded to initial pressures ranging from 0.0 GPa to 10 GPa. Initial loading pressures above 0.7 GPa cause the sample to transform from the α phase to the β phase (refer to Chapter 3). A 4:1 methanol-ethanol mixture was used as a hydrostatic pressure medium [21]. Ruby microspheres [20] were loaded along with the In_2Se_3 powder for *in situ* pressure measurements. Ruby fluorescence spectra were taken before and after each XRD spectrum and pressure was determined by the R_1 and R_2 peak shifts using the Mao scale [26] along with a correction for the temperature shift of the R_1 and R_2 peaks. The average was used as the experimental pressure.

The temperature shift of the ruby spectral lines can vary from ruby to ruby due to different chromium concentrations [56]. To determine the thermal shift of the R_1 and R_2 spectral lines for our ruby microspheres, we measured the wavelength of the R_1 and R_2 peaks at elevated temperatures and atmospheric pressure. Figures 5.2 and 5.3 show the thermal shifts of the R_1 and R_2 spectral lines at atmospheric pressure up to 150 °C. The shift of the R_1 peak is 0.0078(1) nm/°C, which is slightly higher than R_1 thermal shifts reported for ruby chips: 0.0070(4)nm/°C ref. [57], 0.0073(1) nm/°C ref. [58], 0.0063(2) nm/°C ref. [59]. The shift of the R_2 peak is 0.0071(1) nm/°C.

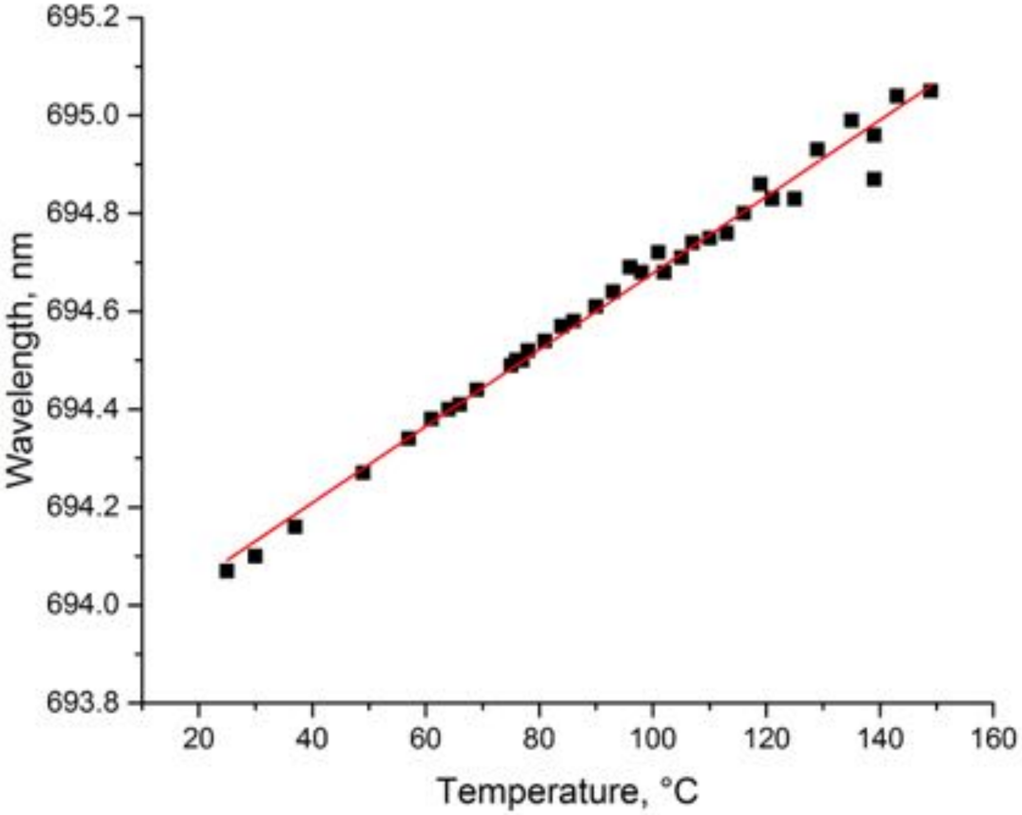

Figure 5.2: Ruby R_1 peak shift with temperature.

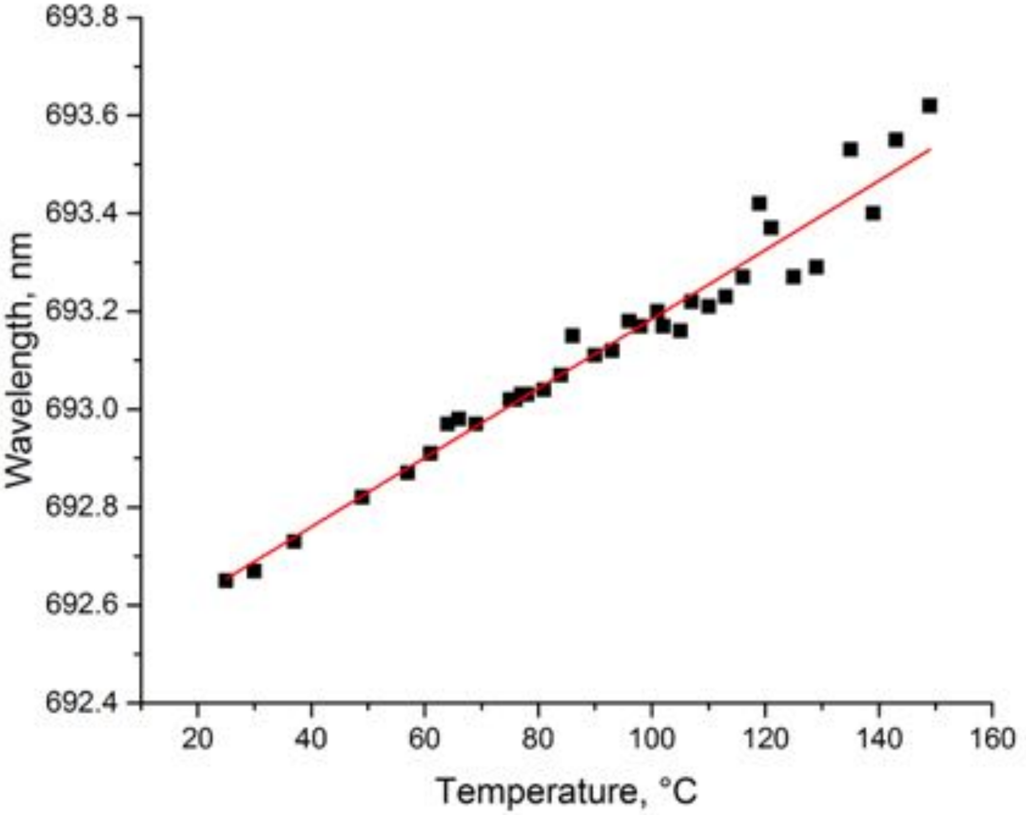

Figure 5.3: Ruby R_2 peak shift with temperature.

Above 150 °C the R_1 and R_2 peaks merge [60]. There are two ways one can deal with this. The first is to fit the peak as the sum of two Lorentzian peaks and use the peak centers from the fitting to determine the R_1 and R_2 peaks. The second is to use the temperature shift of the center of the single broad peak to determine the pressure. Both should give equivalent results; we choose the latter because of its simplicity in execution. The temperature dependence of the merged peak is shown in figure 5.4.

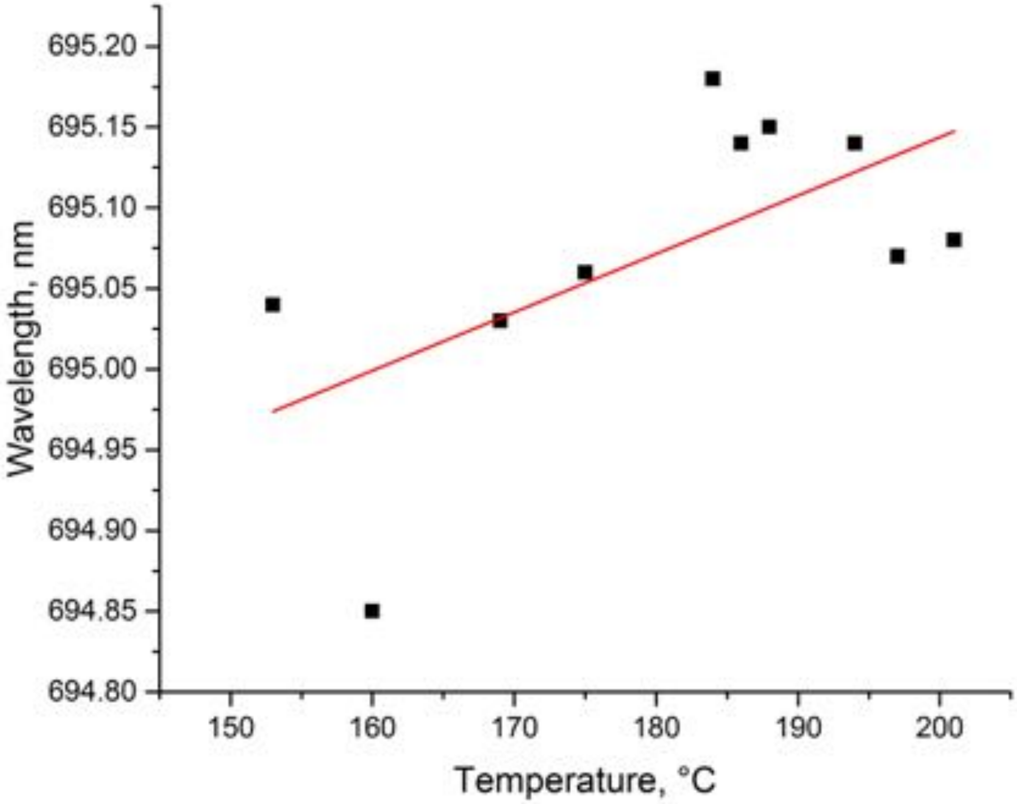

Figure 5.4: Merged ruby R_1 and R_2 peaks above 150 °C.

The experimental pressure was determined from the apparent "pressure," determined by Mao scale, and subtracting a thermal correction to the pressure,

$$P_T = p(T - T_0) \tag{5.1}$$

where p is shift of the "pressure" calculated from the ruby spectral lines of the ruby spheres at elevated temperature and atmospheric pressure. The temperature shifts for the ruby pressure calibration were determined for temperatures below 150 °C and above 150 °C, see figure 5.5.

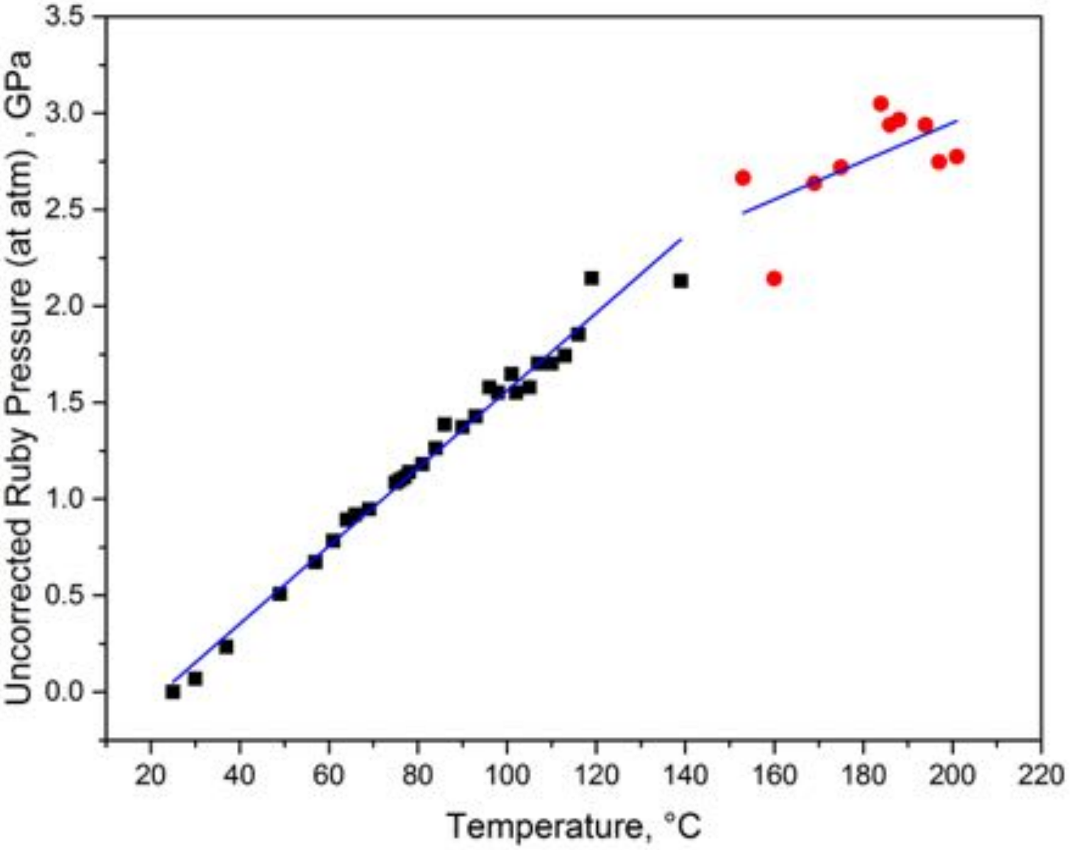

Figure 5.5: Temperature shifts for the ruby pressure calibration at atmospheric pressure. The black squares are "pressures" calculated from distinct R_1 and R_2 ruby lines. The red circles are pressures calculated from the merged R_1 and R_2 peak for temperatures above 150 °C. The solid lines are linear fits the pressure shifts.

Platinum (Pt) was also used as a pressure calibrant in some experiments to confirm the ruby pressure calibration. The unit cell volume for the Pt sample was determined through LeBail fitting in GSAS and then from the Pt EOS [61] an experimental pressure was calculated. The pressures determined from the ruby and Pt at elevated temperatures between 23 °C-295 °C are consistent (see figure 5.6).

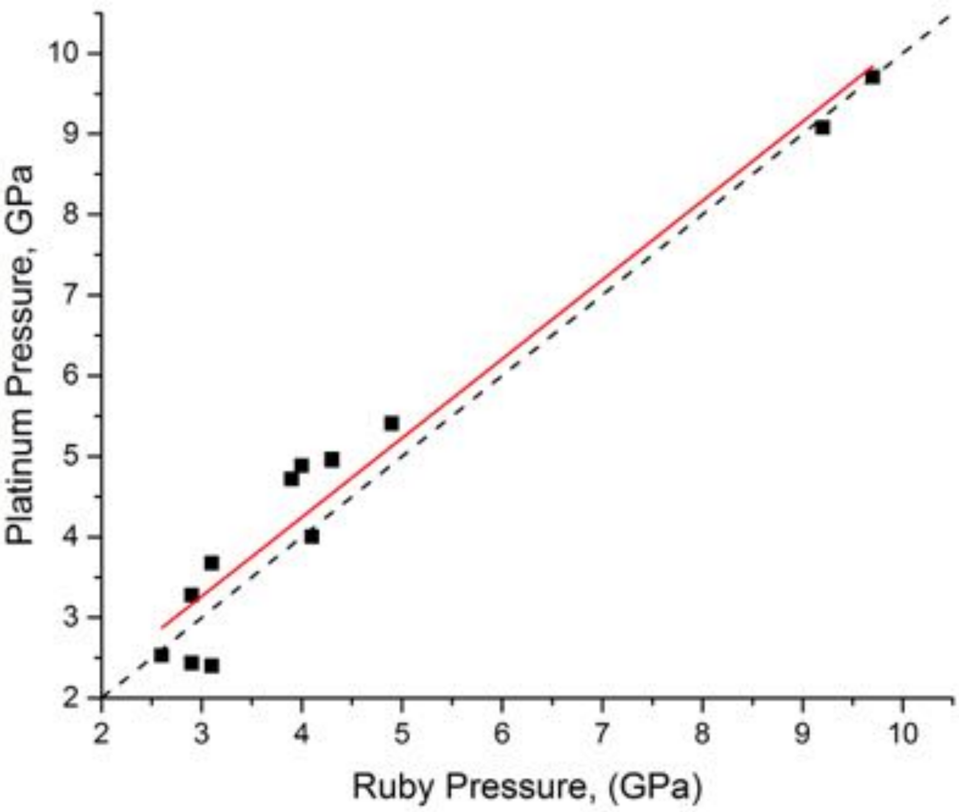

Figure 5.6: Pressures determined by Pt and ruby calibrations for temperatures up to 295 °C. The solid red line is a linear regression fit; slope: 0.97(9) and y-intercept: 0.5. The dashed line has slope of 1 and y-intercept 0.

5.1.3 X-ray Diffraction

XRD experiments were performed at the Advanced Light Source (ALS), Lawrence Berkeley National Laboratory (LBNL), beamline 12.2.2 (Ref. [30]). Spectra were collected at a wavelength of 0.4959 Å by a high resolution MAR3450 plate detector.

5.2 Results and Discussion

We performed two high temperature experiments with starting pressures of 0.0 GPa. At atmospheric pressure the sample is in the α phase. Figures 5.7 and 5.8 are XRD spectra of In_2Se_3 for each experiment showing the α to β phase transition. In figure 5.7, the spectrum taken at 175 °C shows the 006 peak just beginning to split, indicating the start of the transition from the α to the β phase. With increased temperature we see that the intensity of the 104 peak decreases while the 105 peak increases in relative intensity, consistent with the high-temperature α to β transition reported by Popović *et al.* [5].

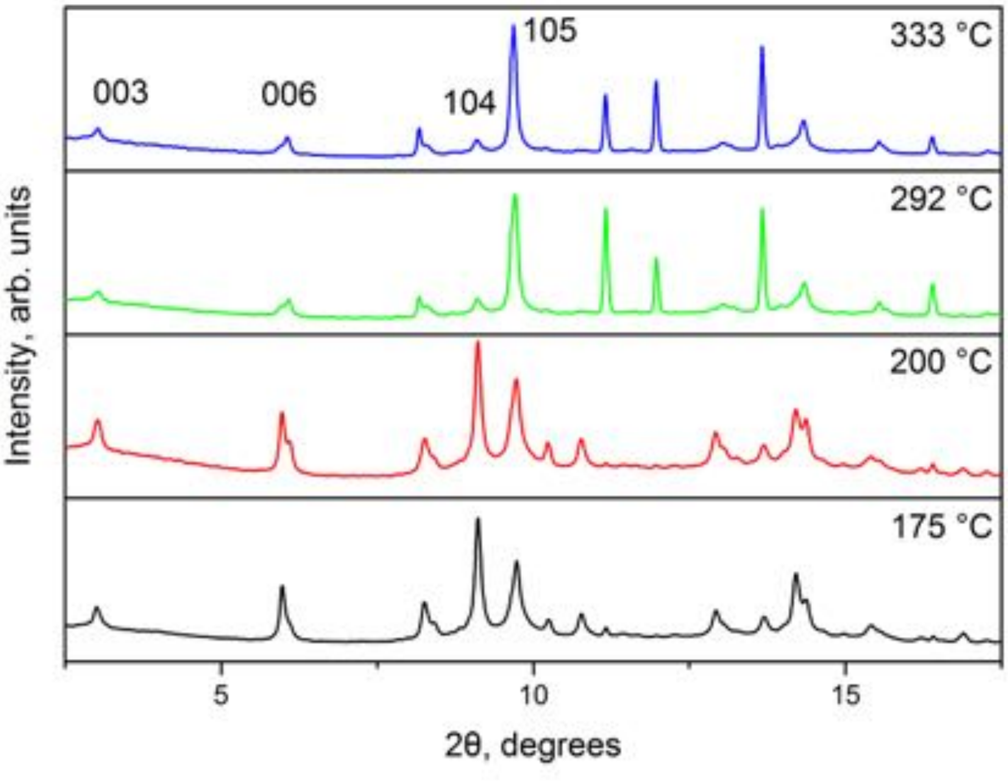

Figure 5.7: Integrated XRD spectra for In_2Se_3 at ambient pressure and increasing temperatures. The α to β transition is indicated by the splitting of the 006 peak and relative increase in intensity of the 105 peak.

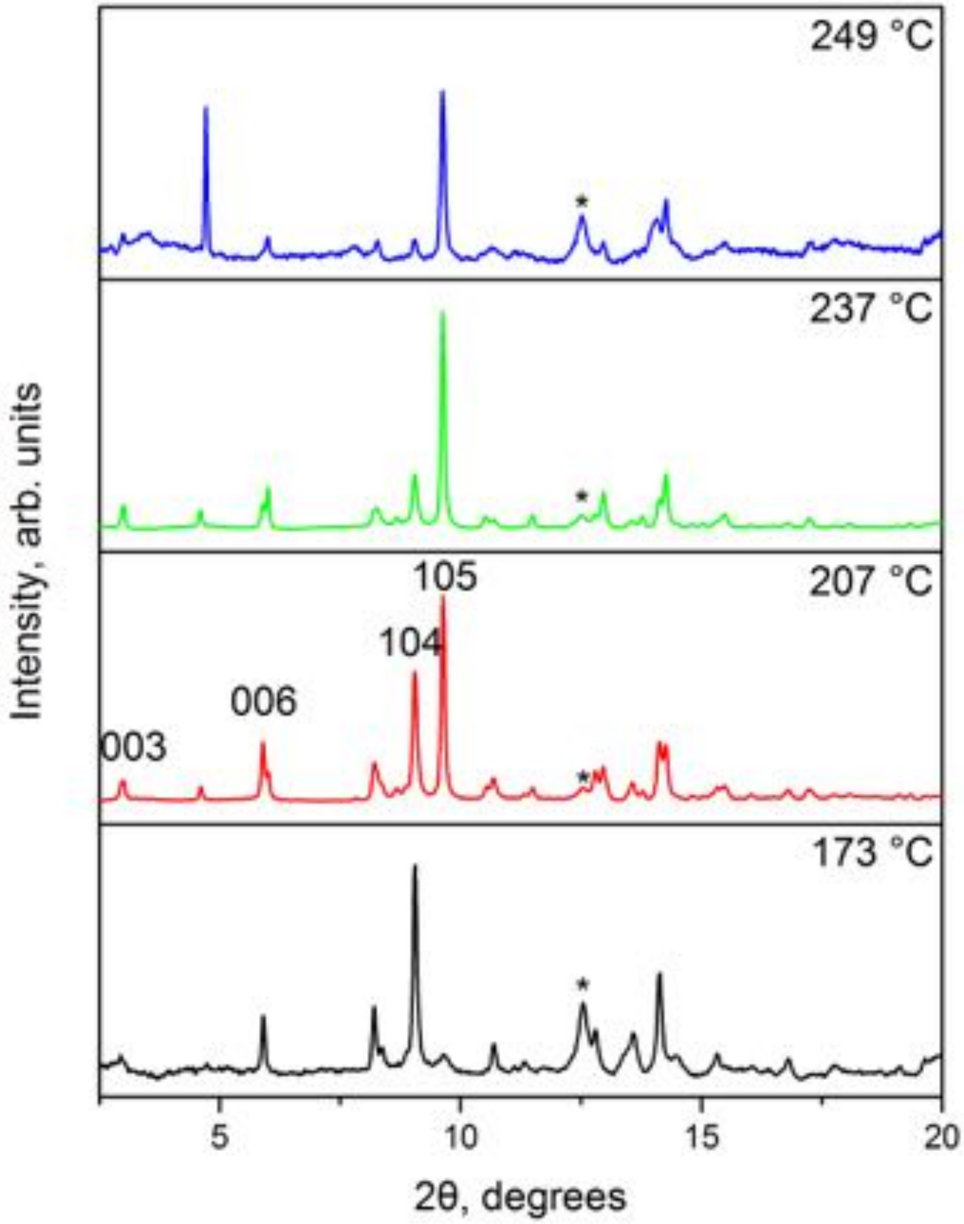

Figure 5.8: Integrated XRD spectra for In_2Se_3 at ambient pressure and increasing temperatures showing the α to β phase transition. * indicate Pt peaks used to verify ruby pressure measurements.

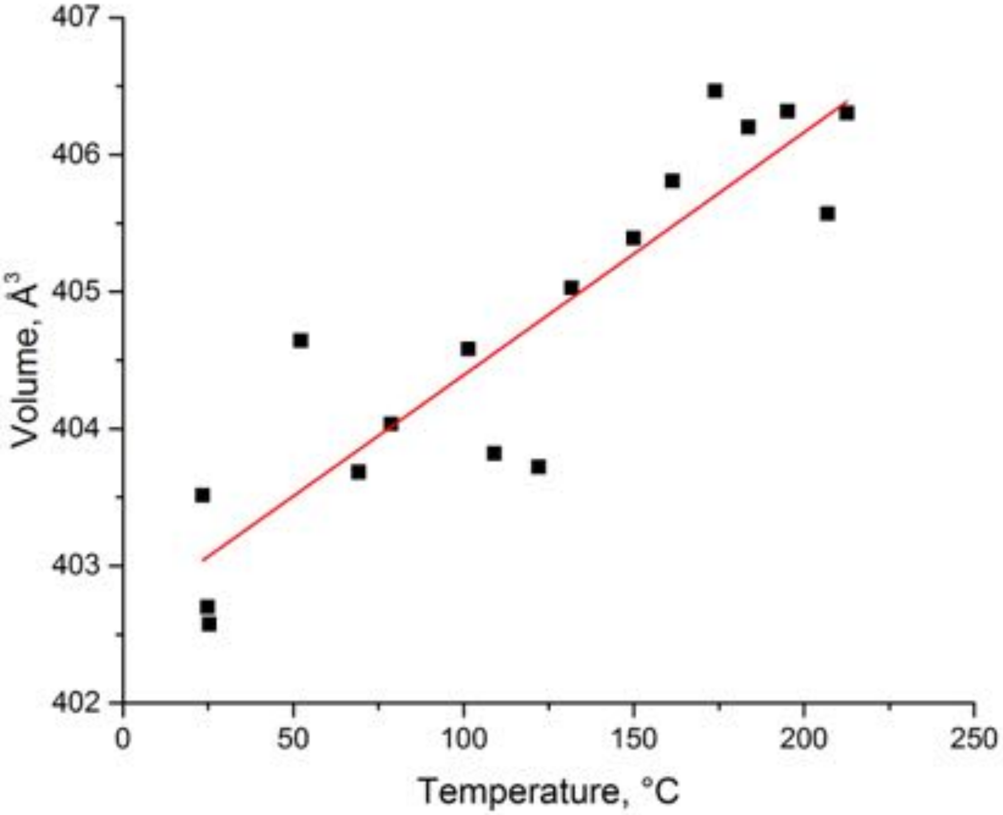

Figure 5.9: Volume versus temperature data at atmospheric pressure for α-phase In_2Se_3. The solid line is fit to the equation $V_T = V_0 \exp(aT)$: $V_0 = 403.0(3)$Å^3 and $a = 4.4(6)E - 5$ K^{-1}.

Figure 5.9 shows the volume verses temperature data for α-phase In_2Se_3 at atmospheric pressure. We fit it to an exponential model for thermal volume expansion

$$V_T = V_0 \exp(aT) \tag{5.2}$$

where a is the thermal expansivity. The fit is shown as the solid red line with $V_0 = 403.0(3)$ Å^3 and $a = 4.4(6)E - 5$ K^{-1}.

High-temperature experiments were also performed on samples under pressure. Figures

5.10, 5.12, and 5.14 show XRD spectra of In_2Se_3 from three different elevated pressure and temperature experiments. New peaks, marked with arrows, start to appear as the temperature is increased above 280 °C. These peaks do not index to the β-phase, space group $R\bar{3}m$, indicating the presence of a new phase. Figures 5.11, 5.13, and 5.15 show the pressure and temperature points for each XRD spectrum taken during each experiment. The red circles in the P-T plots indicate spectra that contain the additional peaks. Figure 5.16 is the combined P-T plot for all three experiments. In all three experiments the additional peaks appear between 280 °C and 300 °C. Therefore, the transition temperature range does not seem to be affected by elevated pressures.

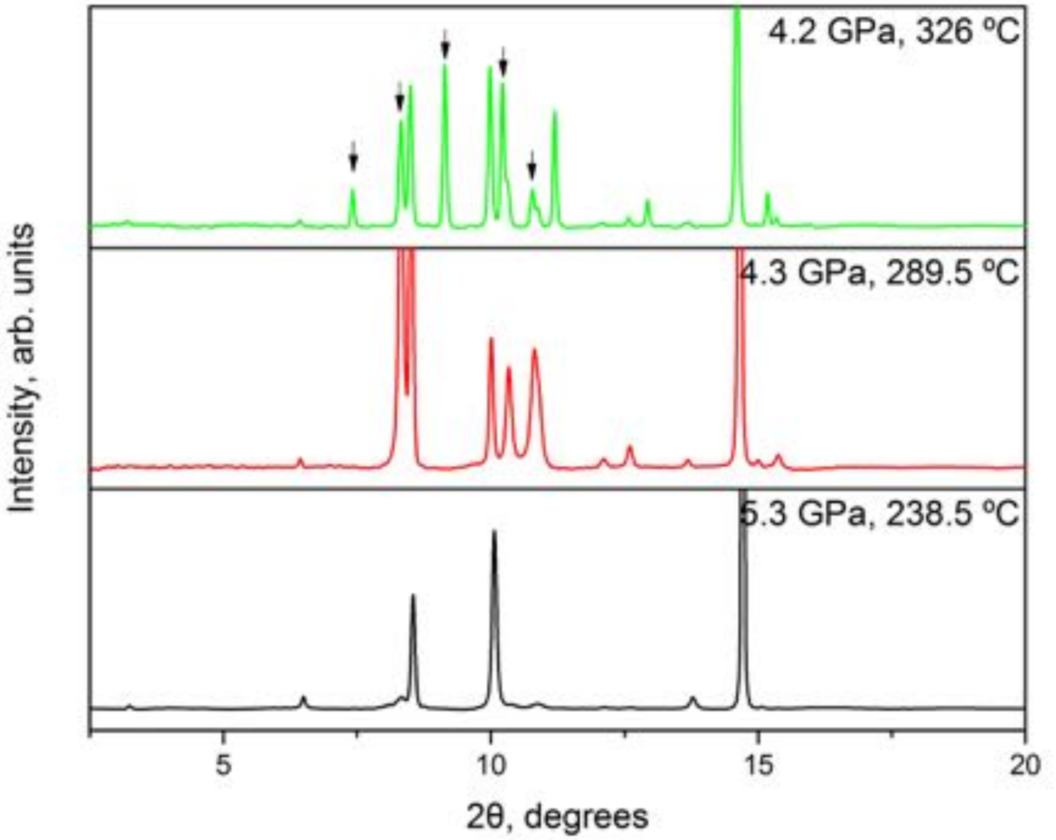

Figure 5.10: Integrated XRD spectra for In_2Se_3 at elevated pressures and temperatures.

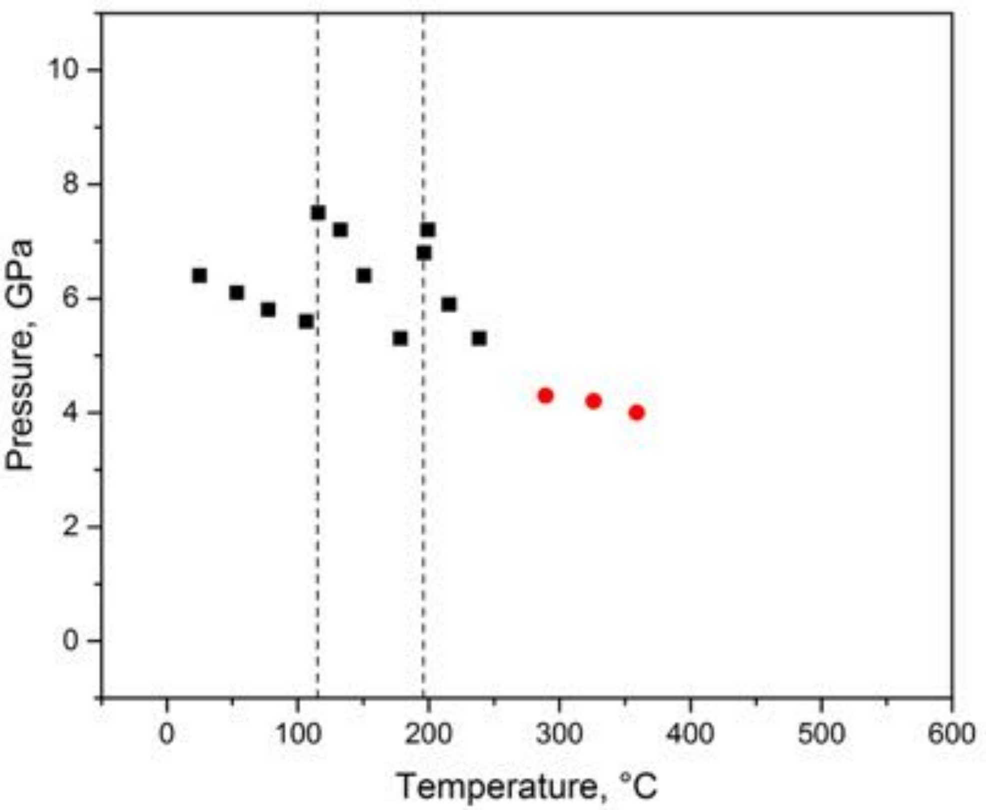

Figure 5.11: Pressure-temperture plot showing the experimental pressures and temperatures for each XRD spectrum. Black squares indicate β phase spectra; red circles indicate the spectra containing the additional peaks. Dashed lines indicate when DAC screws were tightened to maintain pressure loading.

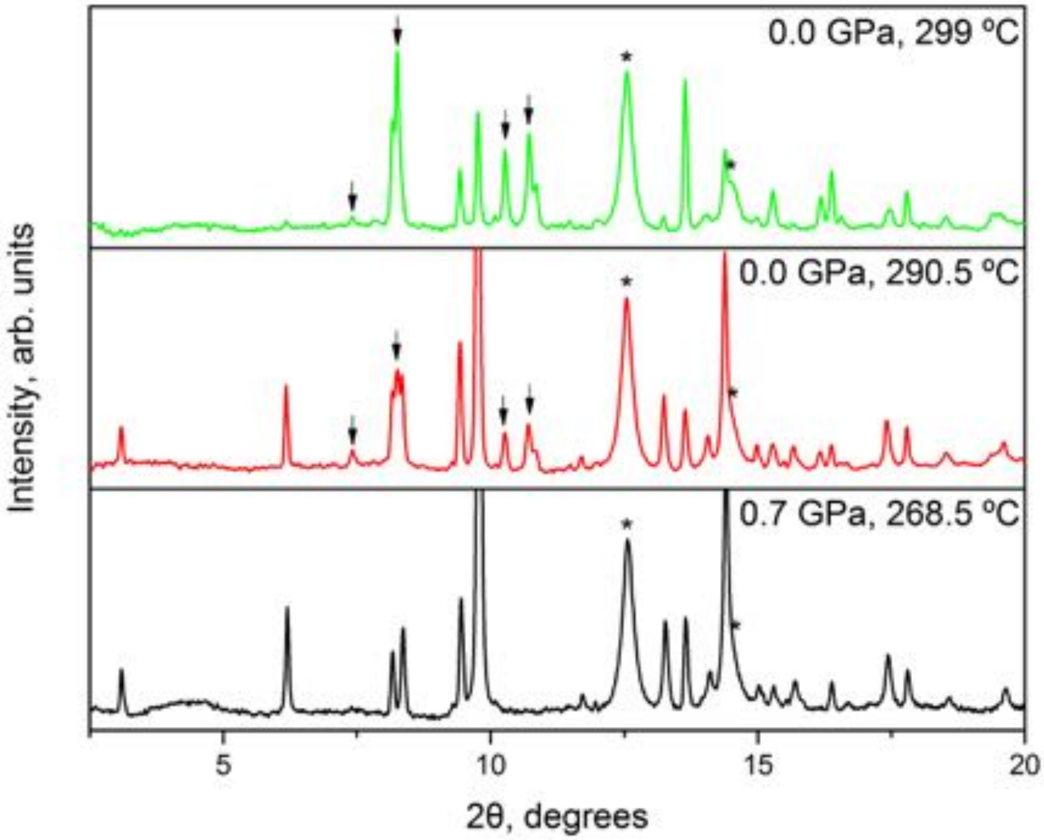

Figure 5.12: Integrated XRD spectra for In_2Se_3 at elevated pressures and temperatures. * indicate Pt peaks used to measure pressure.

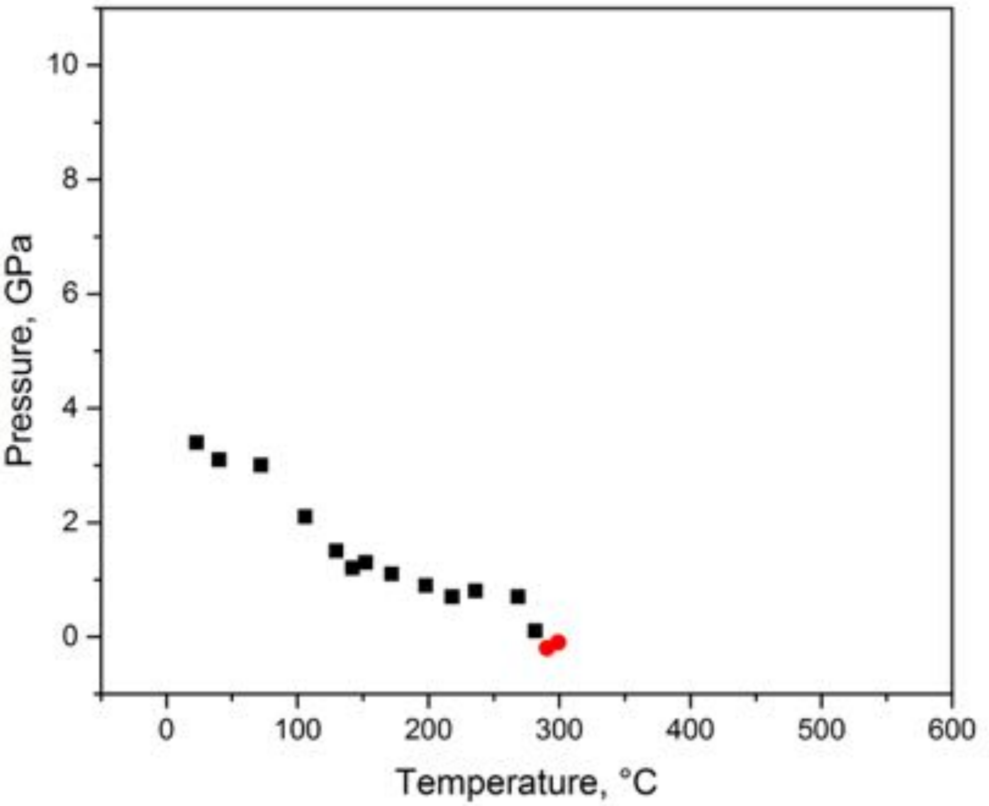

Figure 5.13: Pressure-temperture plot showing the experimental experimental pressures and temperatures for each XRD spectrum. Black squares indicate β phase spectra; red circles indicate the spectra containing the additional peaks.

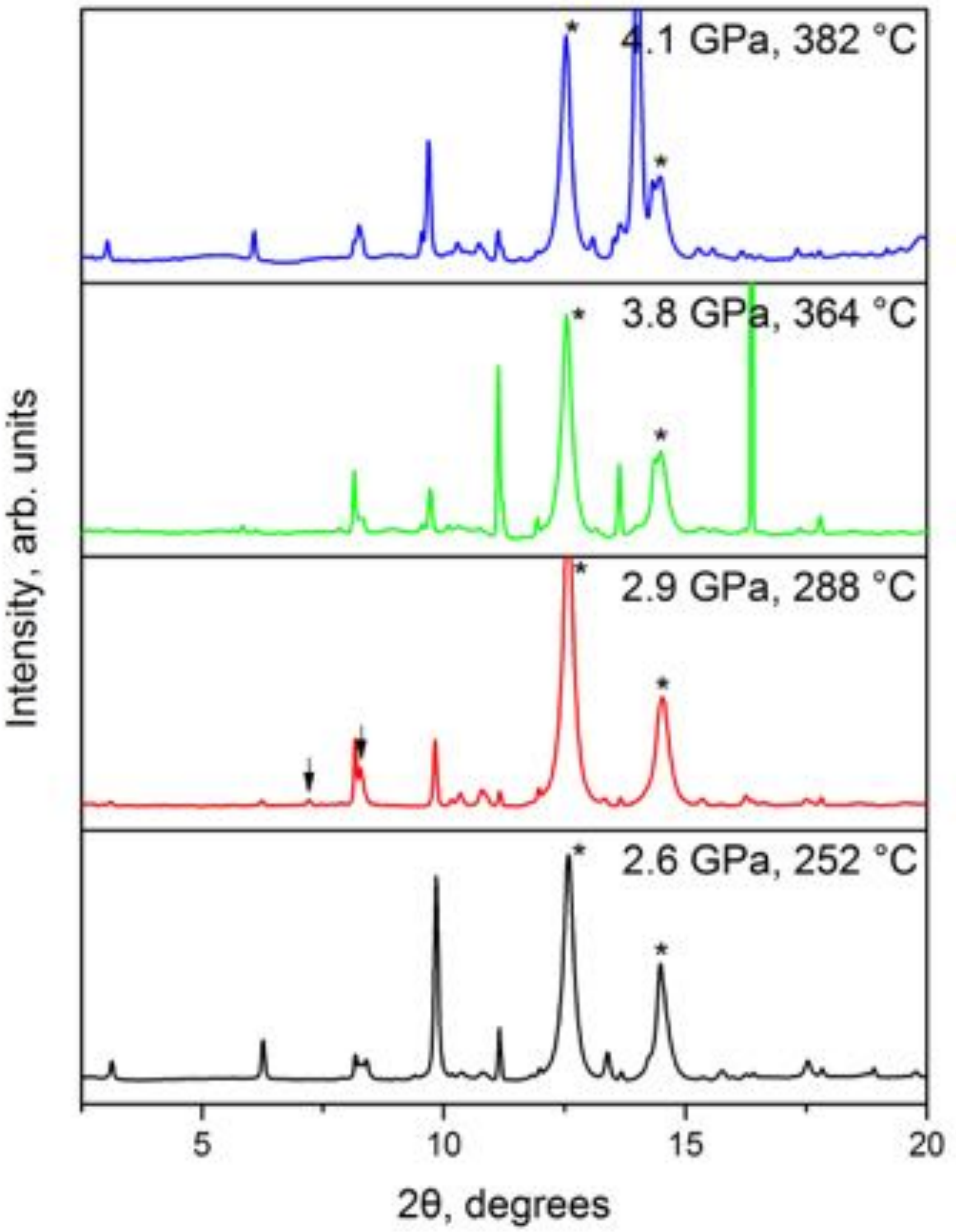

Figure 5.14: Integrated XRD spectra for In_2Se_3 at elevated pressures and temperatures.

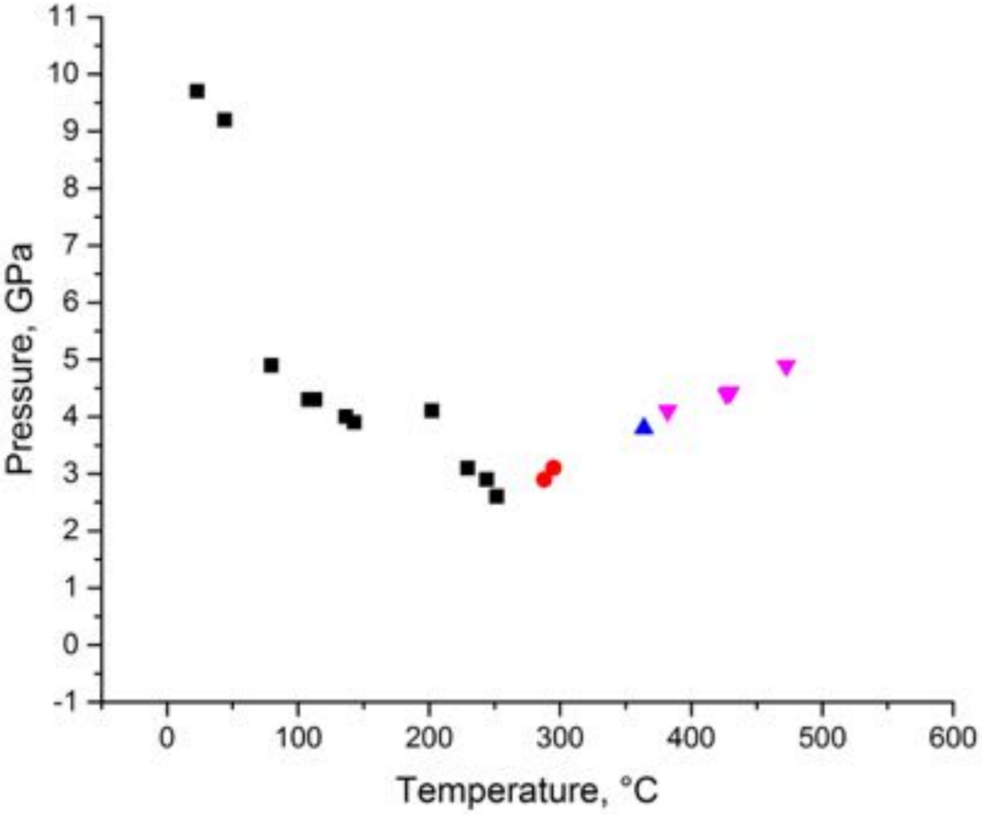

Figure 5.15: Pressure-temperture plot showing the experimental pressures and temperatures for each XRD spectrum. Black squares indicate β phase spectra, red circles indicate the spectra containing the additional peaks, the blue triangle indicates a spectrum with only the new peaks present (no β peaks), magenta triangles indicate the return of the β peaks.

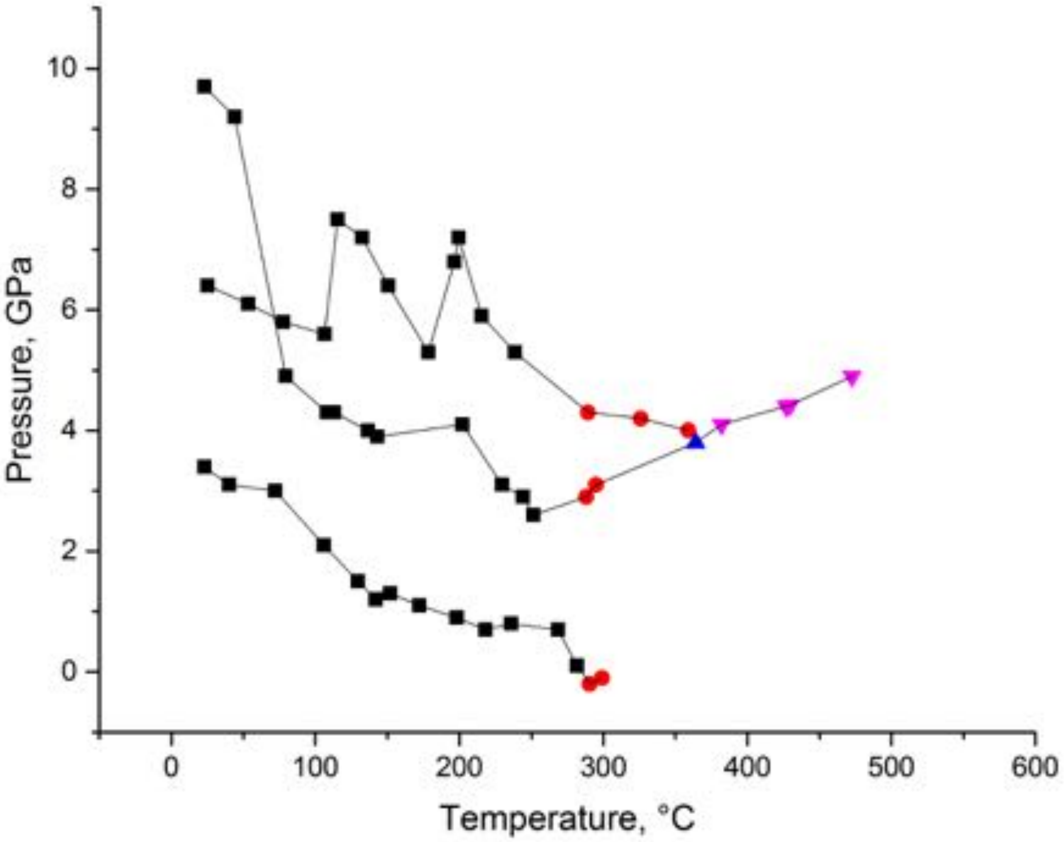

Figure 5.16: P-T plot showing phases present in all three experiments. Black squares indicate β phase spectra, red circles indicate the spectra containing the additional peaks, the blue triangle indicates a spectrum with only the new peaks present (no β peaks), magenta triangles indicate the return of the β peaks.

In figure 5.14 we see that at 364 °C the 003 and 006 peaks nearly vanish but reappear strongly at 382 °C. Before the ruby system was available on the beamline, two high-temperature high-pressure XRD experiments were performed to test the experimental set-up but without being able to take ruby spectra at elevated temperatures. An alternative pressure calibrant was not used. These experiments also showed the same vanishing and reappearing of the 003 and 006 peaks, shown in figures 5.17 and 5.18.

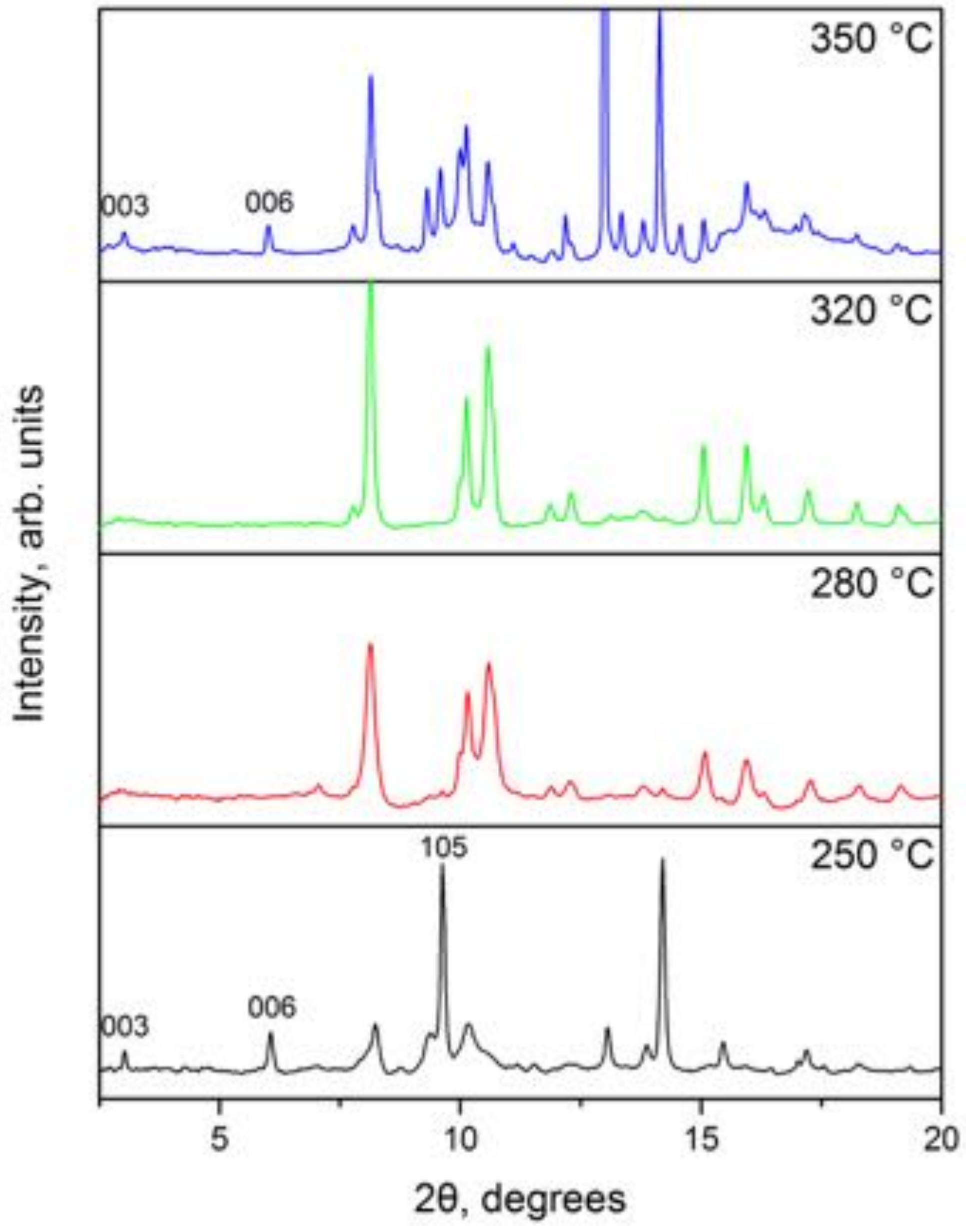

Figure 5.17: Integrated XRD spectra for In_2Se_3 at elevated pressures and temperature. Starting pressure was 1.2 GPa at room temperature. No pressure calibration was taken for elevated temperatures.

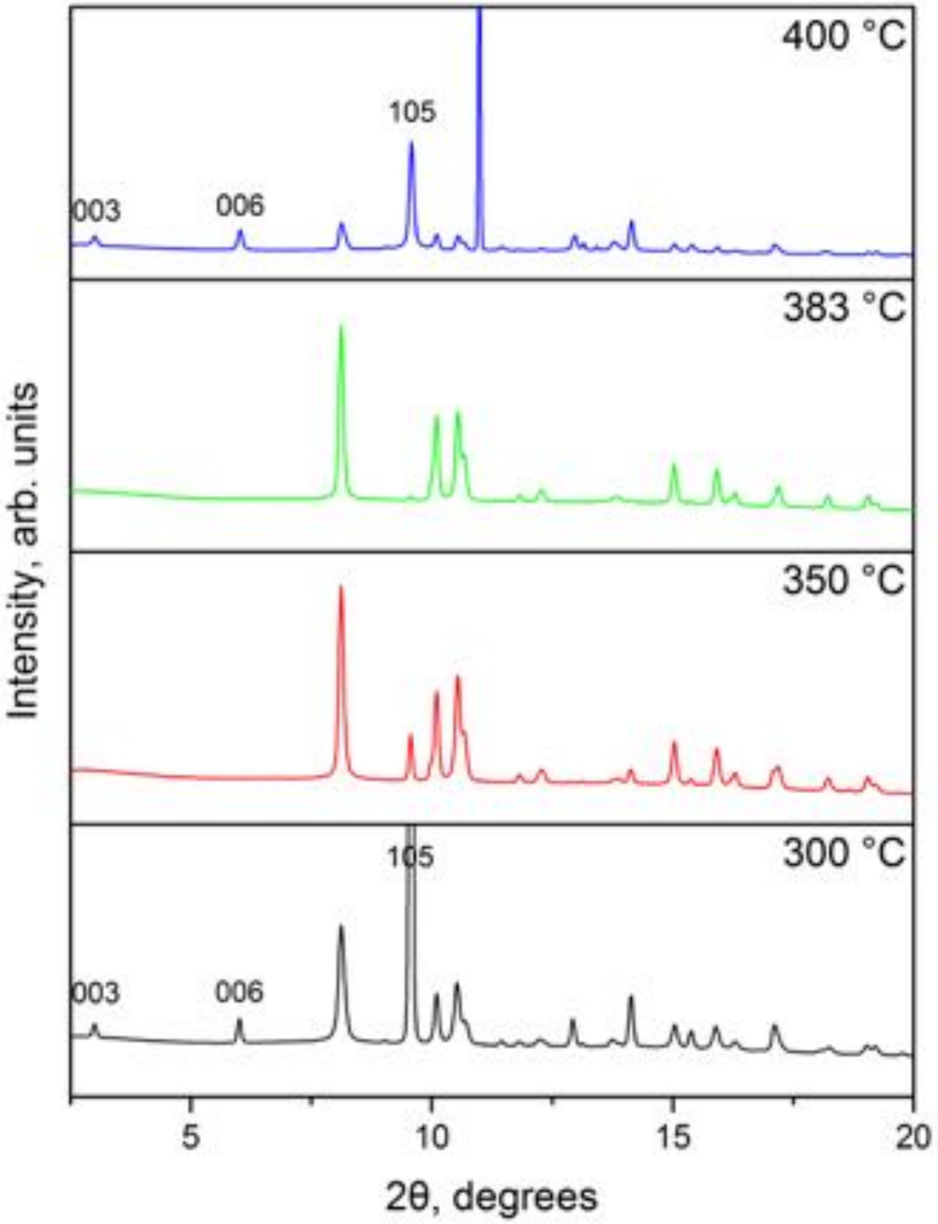

Figure 5.18: Integrated XRD spectra for In_2Se_3 at elevated pressures and temperature. Starting pressure was 2.5 GPa at room temperature. No pressure calibration was taken for elevated temperatures.

The XRD spectra were fit using the Le Bail fitting in the GSAS program [35, 36] to determine the volume and lattice parameters. We assigned the layered α and β phases to $R\bar{3}m$. Pressure-temperature-volume data for the high-pressure β phase are shown in figure 5.19, including the ambient temperature high-pressure data from chapter 3, and the surface fitting to the third-order high-temperature Birch-Murnaghan equation of state (EOS) [62],

$$P = \frac{3}{2}K_T\left[\left(\frac{V_T}{V_{PT}}\right)^{\frac{7}{3}} - \left(\frac{V_T}{V_{PT}}\right)^{\frac{5}{3}}\right] \times \left\{1 + \frac{3}{4}(K' - 4)\left[\left(\frac{V_T}{V_{PT}}\right)^{\frac{2}{3}} - 1\right]\right\} \tag{5.3}$$

where

$$K_T = K_0 + (\partial K/\partial T)(T - 300),$$

$$K' = \partial K/\partial P,$$

and

$$V_T = V_0 \exp\left[\int \alpha(T)dT\right].$$

K_0 is the isothermal bulk modulus under ambient conditions (300 K) and K_T the isothermal bulk modulus at elevated temperature T. $\partial K/\partial T$ and $\partial K/\partial P$ are the temperature and pressure partial derivatives of the bulk modulus. V_0 is the unit cell volume under ambient conditions and V_T, the unit cell volume at elevated temperature T. V_{PT} is the experimentally determined unit cell volume from the XRD spectrum taken at pressure P and temperature T. $\alpha(T)$ is the the volume thermal expansivity, which we fit assuming a linear dependence on temperature, $\alpha(T) = a + bT$ [63]. All parameters were allowed to vary for the fitting.

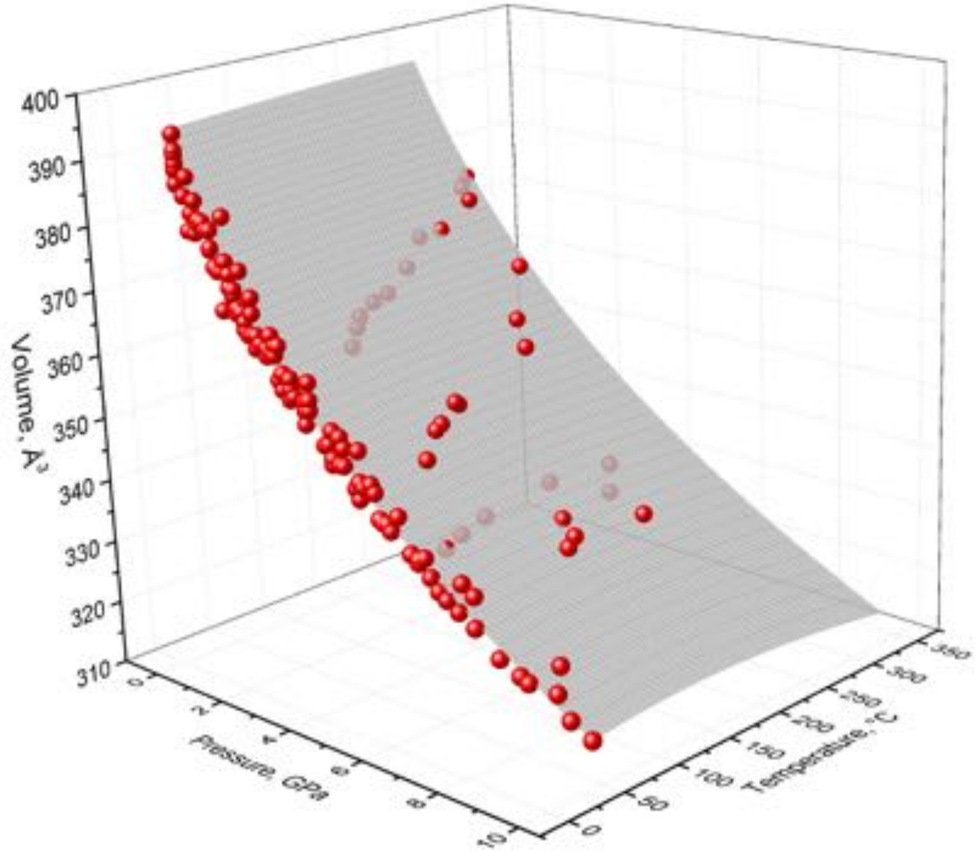

Figure 5.19: P-V-T data for the high-pressure β phase. The surface is the fit to the third-order high-temperature Birch-Murnaghan equation of state (EOS).

The high pressure β phase has an isothermal bulk modulus of $K_0 = 29(3)$ GPa, ambient unit cell volume of $V_0 = 388(1)$ Å^3, and pressure partial derivative of the bulk modulus of $(\partial K/\partial P)_T = 6.6(9)$, consistent what was found in chapter 3 when only considering the ambient temperature experiments. The thermal partial derivative of the bulk modulus is $(\partial K/\partial T)_P = 0.04(1)$ indicating that varying temperatures has only a small effect on the bulk modulus. The volume thermal expansivity is $\alpha(T) = a + bT$ with $a = -2.0(6) \times 10^{-4}$ K^{-1} and $b = 7(4) \times 10^{-7}$ K^{-2}.

Using the EOS and the In_2Se_3 unit cell volumes determined from the GSAS analysis, we can calculate approximate pressures for the two experiments missing pressure calibration at elevated temperatures, but only for temperatures below the first phase transition. Naively assuming the pressure remains constant after the phase transition, I added these two experiments to the P-T plot (figure 5.20). We can see that there are two distinct β phase regions, a high pressure region (labeled HP-β) and a high temperature region (labeled HT-β) with a transition region in-between. When cooled, the diffraction spectra do not show the additional peaks that were observed between 250 °C and 380 °C, indicating that the sample remains in the high-temperature β phase upon cooling to room temperature.

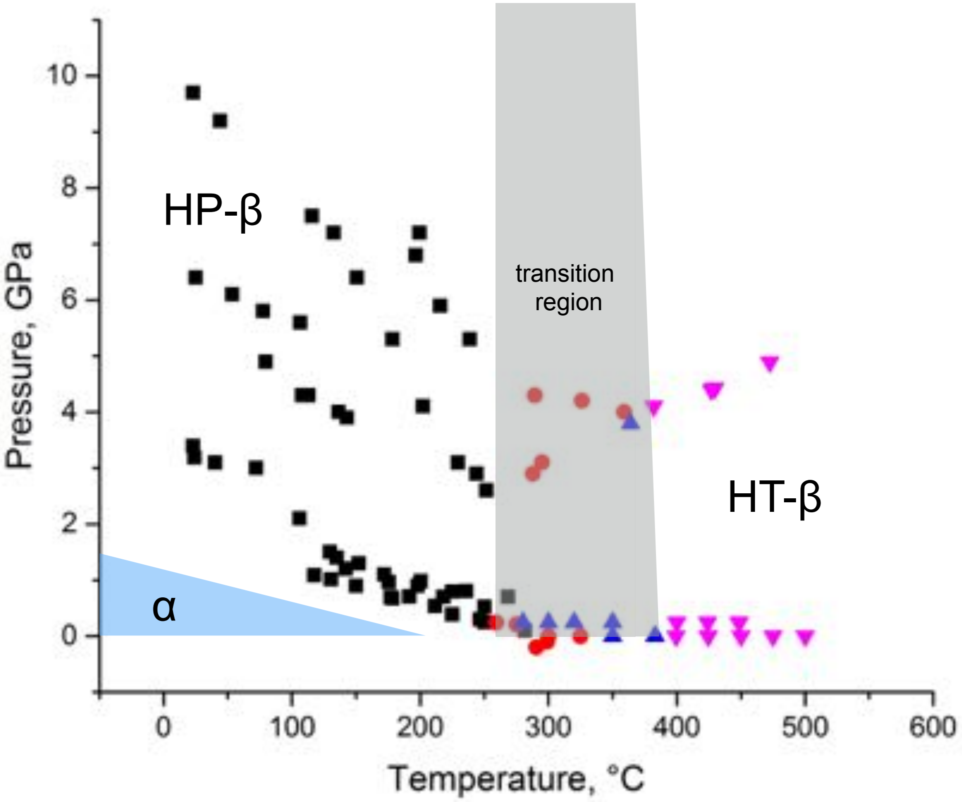

Figure 5.20: P-T plots of all experiments indicating phase present, including test experiments without pressure calibrant. The grey highlight indicates the transition region between the high-pressure and high-temperature β phases.

5.3 Conclusions

Using XRD and high temperature DACs we investigated how elevated temperatures and pressures affect the crystal structure of In_2Se_3. The thermal α to β phase transition was found to occur around 200 °C at atmospheric pressure, consistent with the observations of Popović *et al.* [5]. The high-pressure β phase transitions into a high-temperature β phase at temperatures above 380 °C. The thermal expansion of the α phase was characterized for atmospheric pressures. The EOS parameters were found for the high-pressure β phases by fitting P-T-V data to the high-temperature Birch-Murnaghan EOS.

Chapter 6

Conclusions

6.1 Phase Diagram for In_2Se_3

Our XRD studies of In_2Se_3 under high pressure and high temperature give insight into the phase diagram of In_2Se_3. Figure 6.1 is a metastable “phase diagram” showing the transitions between metastable and stable phases of In_2Se_3. At elevated pressure at room temperature, the α phase transforms into the high-pressure β phase. This high-pressure β phase appears to be distinct from the high-temperature β phase. Increasing the temperature causes the high-pressure β phase to go through an intermediate phase before transitioning into the high-temperature β phase. This suggests that the high-pressure β phase is not the stable phase at high pressure but a metastable phase with a kinetic barrier preventing the transition into the stable β phase. With an increase in temperature the kinetic barrier is overcome and the sample transforms into the stable β phase. α-phase In_2Se_3 transforms directly into the stable high-temperature β phase with the transition beginning just below 200 °C. The stable phase diagram for In_2Se_3 is shown in figure 6.2, which is quite simple. The α phase transitions into the stable β phase under increased pressures or increased temperatures.

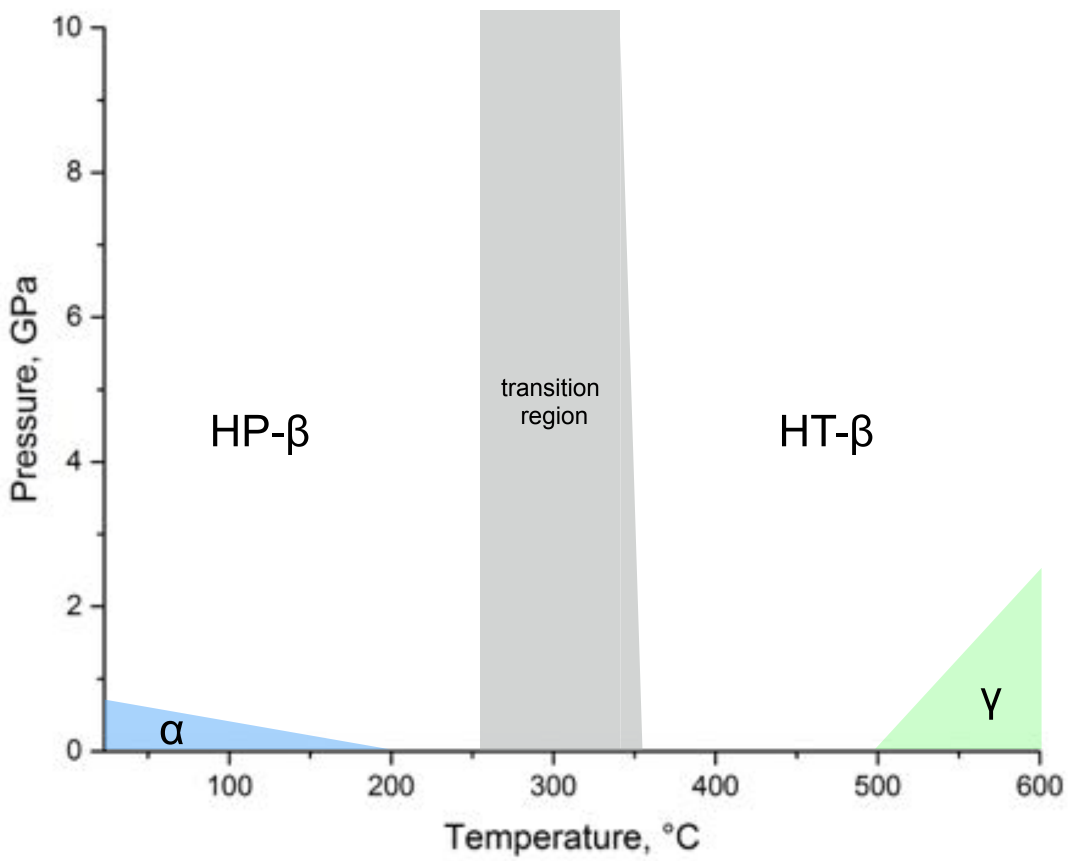

Figure 6.1: Metastable “phase diagram” for In_2Se_3.

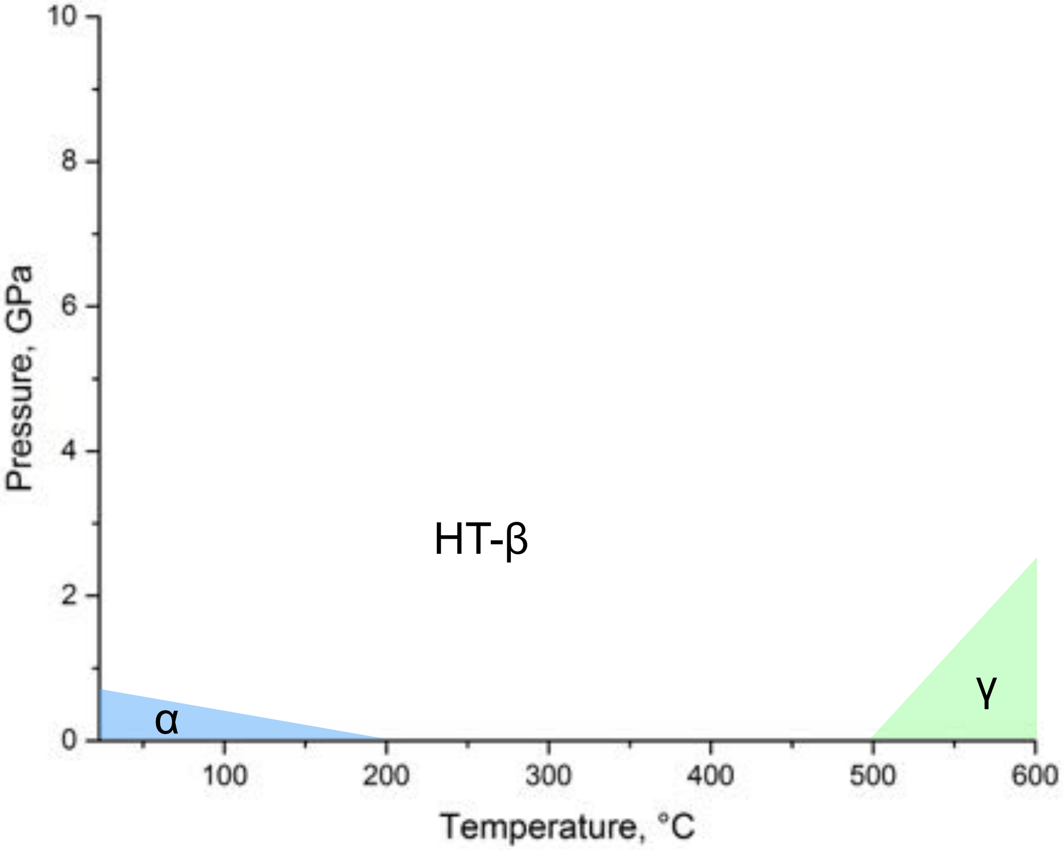

Figure 6.2: Stable phase diagram for In_2Se_3.

From the Birch-Murnaghan EOS fits, we found that the α phase, high pressure β phase, and γ phase all have similar atmospheric bulk moduli of $K_0 = 22 \pm 5$ GPa, $K_0 = 29 \pm 2$ GPa, and $K_0 = 28.2 \pm 0.7$ GPa, respectively. For the α phase EOS fit we held the atmospheric volume fixed at 134 Å^3 per In_2Se_3 molecule. The high pressure β phase is denser with atmospheric volume of 130 Å^3 per In_2Se_3 molecule. The metastable γ phase is the least dense of the three phases studied with an atmospheric volume of 142 Å^3 per In_2Se_3 molecule.

6.2 Future work

Additional high-temperature, high-pressure experiments would help to better characterize the high-pressure β to high-temperature β transition. Determining the atom locations within the unit cell through Rietveld refinement could reveal structural differences between the high-pressure and high-temperature β phases. High-temperature DAC experiments exceeding 520 °C would allow us to determine the stable pressure-temperature region for the γ phase.

Bibliography

[1] S. Raoux, F. Xiong, M. Wuttig and E. Pop, MRS Bulletin **39** (2014), p. 703

[2] J. Y. Lee, K. Sun, B. Y. Li, Y. H. Xie, X. Y. Wei and T. P. Russell, Appl. Phys. Lett. **97** (2010), p. 092114

[3] H. Lee, D. H. Kang and L. Tran, Mater. Sci. Eng. B **119** (2005), p. 196

[4] B. Yu, S. Ju, X. Sun, G. Ng, T. Nguyen, D. Janes and M. Meyyappan, Appl. Phys. Lett. **91** (2007), p. 133119

[5] S. Popović, A. Tonejc, B. Gržeta-Plenković, B. Čelustka and R. Trojko, J. Appl. Cryst. **12** (1979), p. 416

[6] A. Pfitzner and H. D. Lutz, J. Solid State Chem. **124** (1996), p. 305

[7] A. Likforman, D. Carré and R. Hillel, Acta Crystallogr. Sect. B. **34** (1978), p. 1

[8] J. Ye, S. Soeda, Y. Nakamura and O. Nittono, Jpn. J. Appl. Phys. **37** (1998), p. 4264

[9] G. Han, Z. Chen, J. Drennan and J. Zou, Small **10** (2014), p. 2747

[10] E. Mafi, A. Soudi and Y. Gu, J. Phys. Chem. C **116** (2012)), p. 22539

[11] A. V. Kolobov, J. Haines, A. Pradel, M. Ribes, P. Fons, J. Tominaga, Y. Katayama, T. Hammouda and T. Uruga, Phys. Rev. Lett. **97** (2006), p. 035701

[12] J. Zhao and L. Yang, J. Phys. Chem. C. **118** (2014), p. 5445

[13] F. Ke, C. Liu, Y. Gao, J. Zhang, D. Tan, Y. Han, Y. Ma, J. Shu, W. Yang, B. Chen, H. Mao, X. Chen and C. Gao, Appl. Phys. Lett. **104** (2014), p. 212102

[14] H. B. Callen, *Thermodynamics* (1985)

[15] A. Mujica, A. Rubio, A. Munoz and R. J. Needs, Rev. Mod. Phys. **75** (2003), p. 863

[16] V. V. Brazhkin, Phs.-Usp **49** (2006), p. 719

[17] M. Yousuf, *Semiconductors and Semimetals* (1998)

[18] W. A. Bassett, High Press. Res. **29** (2009), p. 163

[19] L. Dubrovinsky, N. Dubrovinskaia, E. Bykova, M. Bykov, V. Prakapenka, C. Prescher, K. Glazyrin, H.-P. Liermann, M. Hanfland, M. Ekholm, Q. Feng, L. V. Pourovskii, M. I. Katsnelson, J. M. Wills and I. A. Abrikosov, Nature **525** (2015), p. 226

[20] J. C. Chervin, B. Canny and M. Mancinelli, High Pressure Research **21** (2001), p. 305

[21] G. J. Piermarini, S. Block and J. D. Barnet, J. Appl. Phys. **44** (1973), p. 5377

[22] Z. A. Dreger, N. Trotman and Y. M. Gupta, *The use of ruby single crystals to examine the nonhydrostaticity of pressure media in diamond anvil cell experiments*, unpublished.

[23] P. Vandenabeele, *Practical Raman Spectroscopy: An Introduction* (2013)

[24] C. Kittel, *Introduction to Solid State Physics* (2005)

[25] G. J. Piermarini, S. Block, J. D. Barnet and R. A. Forman, J. Appl. Phys. **46** (1975), p. 2774

[26] H. K. Mao, J. Xu and P. M. Bell, Geophys. Res. **91** (1986), p. 4673

[27] A. L. Robinson, *History of Synchrotron Radiation*, X-Ray Data Booklet
URL: `http://xdb.lbl.gov/Section2/Sec_2-2.html`

[28] F. R. Elder, A. M. Gurewitsch, R. V. Langmuir and H. C. Pollock, Phys. Rev. **71** (1947), p. 829

[29] W. H. Bragg and W. L. Bragg, Proc R. Soc. Lond. A **88** (1913), p. 428

[30] M. Kunz, A. A. MacDowell, W. A. Caldwell, D. Cambie, R. S. Celestre, E. E. Domning, R. M. Duarte, A. E. Gleason, J. M. Glossinger, N. Kelez, D. W. Plate, T. Yu, J. M. Zaug, H. A. Padmore, R. Jeanloz, A. P. Alivisatos and S. M. Clark, J. Synchrotron Radiation **12** (2005), p. 650

[31] A. P. Hammersley, S. O. Svensson and M. Hanfland, High Press. Res. **14** (1996), p. 235

[32] H. M. Rietveld, J. Appl. Cryst. **2** (1969), p. 65

[33] A. L. Bail, Powder Diffraction **20** (2005), p. 316

[34] A. L. Bail, H. Duroy and J. L. Fourquet, Mat. Res. Bull. **23** (1988), p. 447

[35] A. C. Larson and R. B. von Dreele, *GSAS manual*, Los Alamos National Laboratory (1988)

[36] B. H. Toby, J. Appl. Cryst. **34** (2001), p. 210

[37] F. D. Murnaghan, PNAS **30** (1944), p. 244

[38] F. Birch, Phys. Rev. **71** (1947), p. 809

[39] J.-P. Poirier, *Introduction to the Physics of the Earth's Interior* (2000)

[40] R. Lewandowska, R. Bacewicz, J. Filipowicz and W. Paszkowicz, Materials Research Bulletin **36** (2001), p. 2577

[41] R. J. Nelmes and M. I. McMahon, *Semiconductors and Semimetals* (1998)

[42] M. Einaga, A. Ohmura, A. Nakayama, F. Ishikawa, Y. Yamada and S. Nakano, Phys. Rev. B **83** (2011), p. 092102

[43] R. Vilaplana, D. Santamaría-Pérez, O. Gomis, F. J. Manjón, J. González, A. Segura, A. Munoz, P. Rodríguez-Hernández, E. Pérez-González, V. Marín-Borrás, V. Munoz-Sanjose, C. Drasar and V. Kucek, Phys. Rev. B **84** (2011), p. 184110

[44] O. Gomis, R. Vilaplana, F. J. Manjón, P. Rodríguez-Hernández, E. Pérez-González, A. Munoz, V. Kucek and C. Drasar, Phys. Rev. B **84** (2011), p. 174305

[45] J. Zhao, H. Liu, L. Ehm, Z. Chen, S. Sinogeikin, Y. Zhao and G. Gu, Inorganic Chemistry **50** (2011), p. 11291

[46] S. H. Tolbert and A. P. Alivisatos, Ann. Rev. Phys. Chem. **46** (1995), p. 595

[47] G. Kresse and J. Furthmüller, Phys. Rev. B. **54** (1996), p. 11169

[48] P. E. Blöchl, Phys. Rev. B. **50** (1994), p. 17953

[49] G. Kresse and D. Joubert, Phys. Rev. B. **59** (1999), p. 1758

[50] J. P. Perdew, K. Burke and M. Ernzerhof, Phys. Rev. Lett **77** (1996), p. 3865

[51] S. Grimme, J. Antony, S. Ehrlich and H. Krieg, J. Chem. Phys. **132** (2010), p. 154104

[52] S. Grimme, S. Ehrlich and L. Goerigk, J. Comp. Chem **32** (2011), p. 1456

[53] G. J. Hanna, S. T. Teklemichael, M. McCluskey, L. Bergman and J. Huso, J. Appl. Phys. **110** (2011), p. 073511

[54] S. H. Tolbert and A. P. Alivisatos, Science **265** (1994), p. 373

[55] A. P. Alivisatos, J. Phys. Chem. **100** (1996), p. 13226

[56] J. D. Bauer, L. Bayarjargal and B. Winkler, High Press. Res. **32** (2012), p. 155

[57] A. H. Jahren, M. B. Kruger and R. Jeanloz, J. Appl. Phys. **71** (1992), p. 1579

[58] F. Datchi, R. LeToullec and P. Loubeyre, J. Appl. Phys. **81** (1997), p. 3333

[59] Q. Wei, N. Dubrovinskaia and L. Dubrovinsky, J. Appl. Phys. **84** (1998), p. 4049

[60] F. Datchi, A. Dewaele, P. Loubeyre, R. LeToullec, Y. L. Godec and B. Canny, High Press. Res. **27** (2007), p. 447

[61] A. Kavnera and T. S. Duffy, J. Appl. Phys. **89** (2001), p. 1907

[62] Y. Wang, J. Zhang, H. Xu, Z. Lin, L. L. Daemen, Y. Zhao and L. Wang, Appl. Phys. Lett. **94** (2009), p. 071904

[63] I. Suzuki, J. Phys. Earth **23** (1975), p. 145

[64] C. Ma, Q. Zhou, F. Li, J. Hao, J. Wang, L. Huang, F. Huang and Q. Cui, J. Phys. Chem. C **115** (2011), p. 18310

Appendix A

Heptane under pressure

In this section we report the results of a high-pressure XRD experiment on n-heptane.

A.1 Experimental Methods

Samples of n-heptane were loaded into a piston-cylinder diamond-anvil cell. A pre-indented stainless steel gasket was used to contain the sample. Ruby microspheres were inserted into the sample chamber for *in situ* pressure measurements. The pressure was measured before and after each XRD spectrum by the R_1 and R_2 peak shifts using the Mao scale [26] and the average used as the experimental pressure value with estimated precision of 0.1 GPa.

XRD experiments were performed at the Advanced Light Source (ALS), Lawrence Berkeley National Laboratory (LBNL), beamline 12.2.2 (Ref. [30]) The sample was loaded to an initial pressure of 1.7 GPa and spectra were taken for both compression and decompression. All experiments were done at ambient temperature. Spectra were collected at wavelength of 0.4959 Å by a high resolution MAR3450 plate detector. The diffraction images were integrated using the FIT2D program.

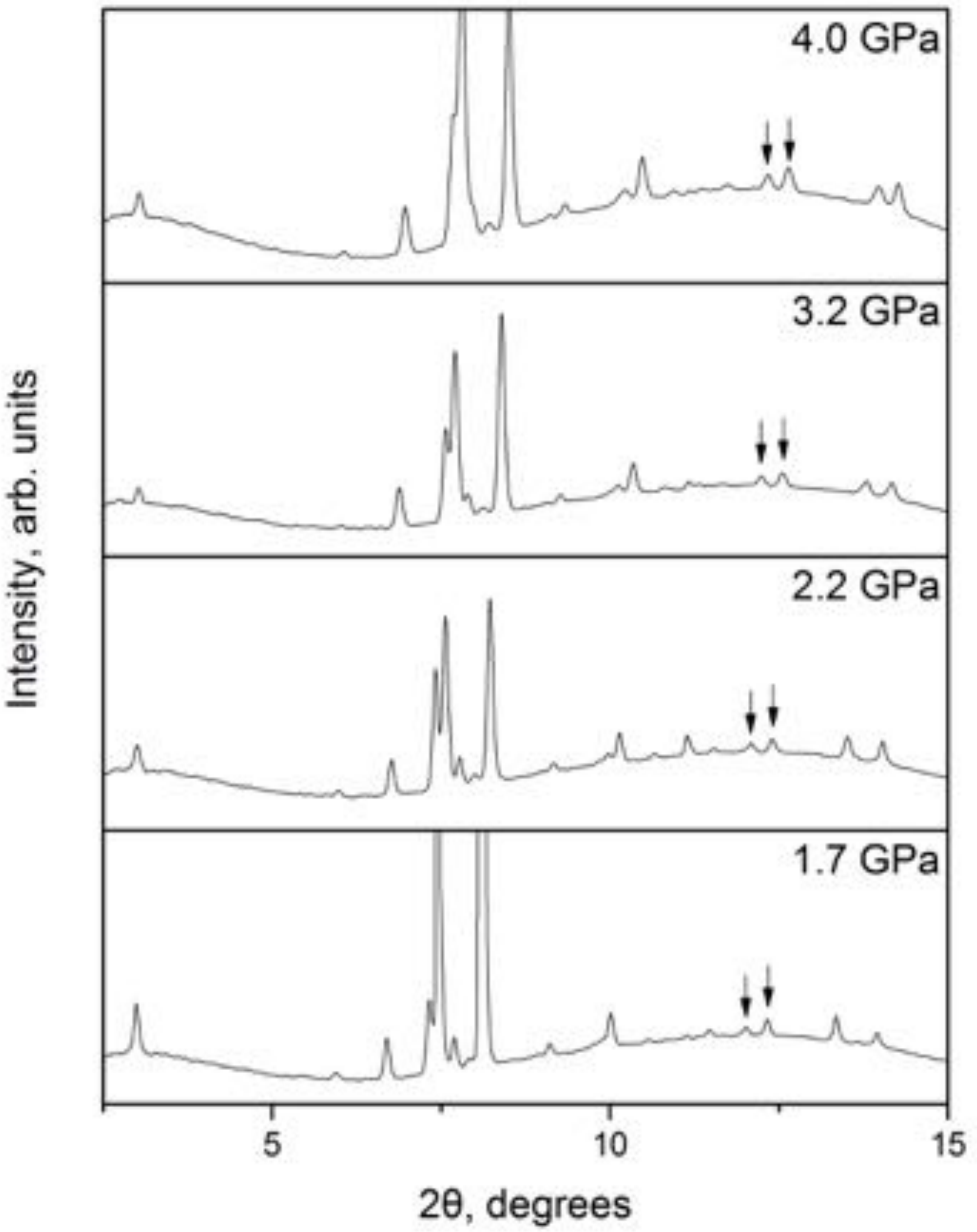

Figure A.1: Integrated XRD spectra for n-heptane at elevated pressures.

A.2 Results and Discussion

Ma *et al.* [64] report a rotator-rotator transition of n-heptane under pressure at approximately 3 GPa, indicated by the appearance of a new peak in the XRD spectra at a d-spacing just under 2.30 Å. They also report two additional peaks appearing around 7.5 GPa, which they consider to be the onset of a rotator-crystalline transition, one of these peaks has a slightly larger d-spacing than the peak they report appearing at 3 GPa.

Figure A.1 shows our XRD spectra for increasing pressures between 1.7 GPa and 4 GPa. We identify two peaks, indicated by arrows, in our 1.7 GPa spectrum corresponding to the two peaks reported by Ma *et al.* to be indicators of the 3 GPa and 7.5 GPa transitions. The presence of these peaks in our experiment at pressures below 3 GPa contradicts their findings. We find no XRD evidence to support a rotator-rotator transition in n-heptane below 4 GPa.

A.3 IR Absorption

We also performed IR absorption experiments on heptane at elevated pressures in a DAC. Figure A.2 shows the IR absorption spectra at 1.8 GPa, 3.9 GPa, and 5.7 GPa take by a Bomem FTIR spectrometer. The peak at 4260 cm^{-1} and the double peaks around 4330 cm^{-1} in the 1.8 GPa spectra shift linearly with pressure between 1.5 GPa and 8.0 GPa (figure A.3). In addition the double peaks change in relative intensity, with the higher wavenumber peak increasing in intensity and the lower wavenumber peak decreasing. A discontinuity in the absorption peak shifts would suggest a first-order phase transition occurs, however, this is not observed. The peaks shift smoothly in the 1.5 GPa to 8.0 GPa pressure range.

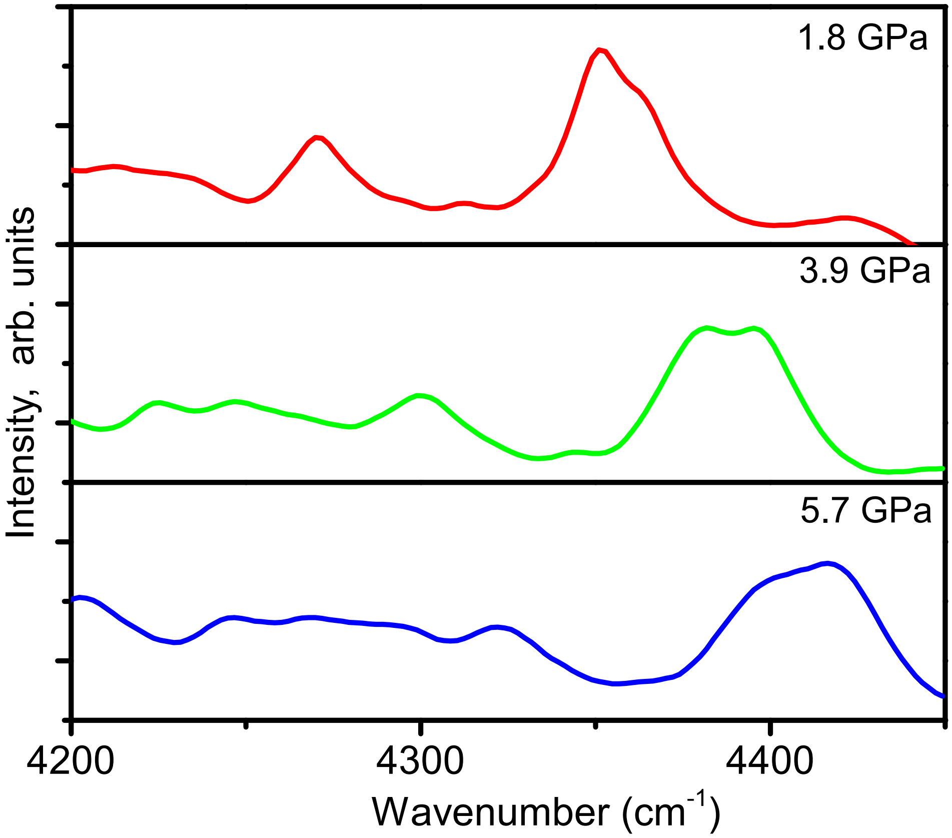

Figure A.2: IR absorption spectra at elevated pressures.

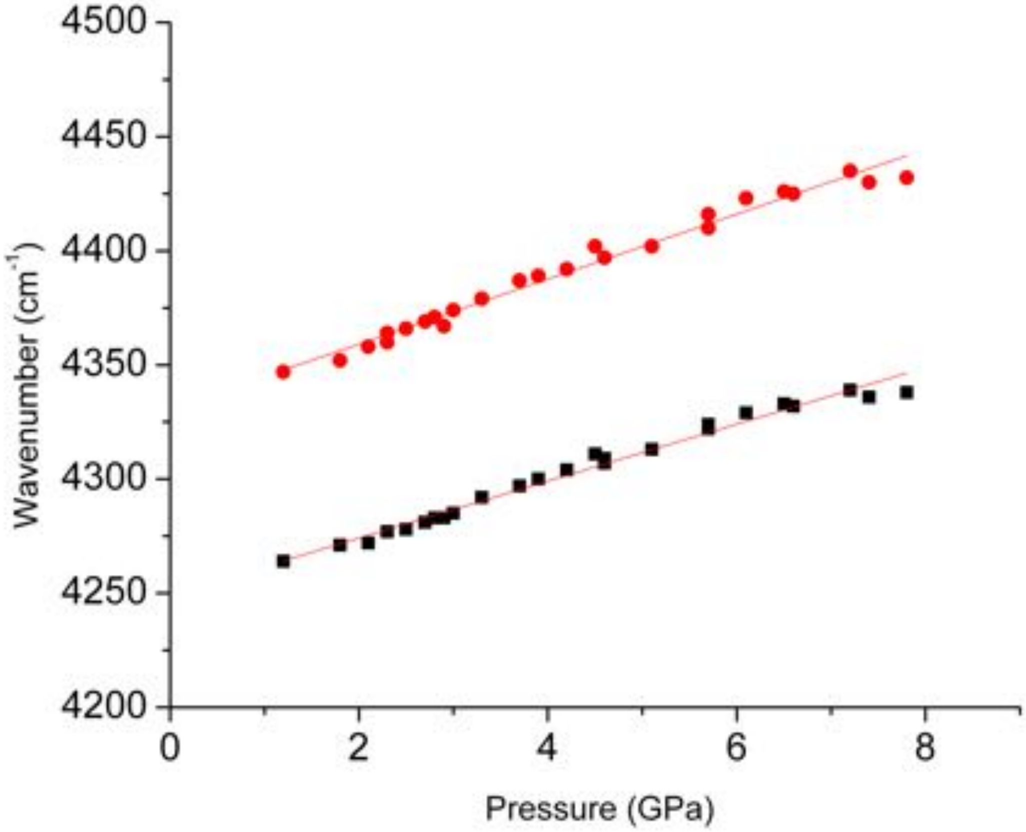

Figure A.3: IR absorption peak shifts with pressure.

Appendix B

Supplementary data

B.1 Supplementary data: α-β transition.

Date	Sample	Location	Wavelength	Beam size (µm)	Pressure medium	Pressure (GPa)	a (Å)
11/2/2011	Bulk	CHESS	0.4859	100	methanol-ethanol	0.9	3.977
11/2/2011	Bulk	CHESS	0.4859	100	methanol-ethanol	1.1	3.969
11/2/2011	Bulk	CHESS	0.4859	100	methanol-ethanol	1.9	3.942
11/2/2011	Bulk	CHESS	0.4859	100	methanol-ethanol	2.8	3.921
11/2/2011	Bulk	CHESS	0.4859	100	methanol-ethanol	3.9	3.902
11/2/2011	Bulk	CHESS	0.4859	100	methanol-ethanol	4.7	3.887
11/2/2011	Bulk	CHESS	0.4859	100	methanol-ethanol	5.3	3.876
11/3/2011	Bulk	CHESS	0.4859	100	methanol-ethanol	5.5	3.875
11/3/2011	Bulk	CHESS	0.4859	100	methanol-ethanol	6.3	3.863
11/3/2011	Bulk	CHESS	0.4859	100	methanol-ethanol	7.3	3.850
11/3/2011	Bulk	CHESS	0.4859	100	methanol-ethanol	7.0	3.854
11/3/2011	Bulk	CHESS	0.4859	100	methanol-ethanol	6.6	3.857
11/3/2011	Bulk	CHESS	0.4859	100	methanol-ethanol	6.1	3.865
11/3/2011	Bulk	CHESS	0.4859	100	methanol-ethanol	5.6	3.871
11/3/2011	Bulk	CHESS	0.4859	100	methanol-ethanol	4.9	3.888
11/3/2011	Bulk	CHESS	0.4859	100	methanol-ethanol	3.1	3.917
11/3/2011	Bulk	CHESS	0.4859	100	methanol-ethanol	2.7	3.923
11/3/2011	Bulk	CHESS	0.4859	100	methanol-ethanol	2.2	3.935
11/3/2011	Bulk	CHESS	0.4859	100	methanol-ethanol	1.6	3.954
11/3/2011	Bulk	CHESS	0.4859	100	methanol-ethanol	1.0	3.971
11/3/2011	Bulk	CHESS	0.4859	100	methanol-ethanol	0.4	3.988
11/3/2011	Bulk	CHESS	0.4859	100	methanol-ethanol	0.2	3.994
11/3/2011	Bulk	CHESS	0.4859	100	methanol-ethanol	0.0	4.013
11/17/2011	Bulk	ALS	0.4959	10	methanol-ethanol	0.2	4.021
11/17/2011	Bulk	ALS	0.4959	10	methanol-ethanol	0.5	3.966
11/17/2011	Bulk	ALS	0.4959	10	methanol-ethanol	1.8	3.940
11/18/2011	Bulk	ALS	0.4959	10	methanol-ethanol	2.0	3.937
11/18/2011	Bulk	ALS	0.4959	10	methanol-ethanol	2.4	3.929
11/18/2011	Bulk	ALS	0.4959	10	methanol-ethanol	3.0	3.919
11/18/2011	Bulk	ALS	0.4959	10	methanol-ethanol	3.4	3.913
11/18/2011	Bulk	ALS	0.4959	10	methanol-ethanol	4.0	3.901
11/18/2011	Bulk	ALS	0.4959	10	methanol-ethanol	4.4	3.894
11/18/2011	Bulk	ALS	0.4959	10	methanol-ethanol	4.8	3.891
11/18/2011	Bulk	ALS	0.4959	10	methanol-ethanol	5.2	3.885
11/18/2011	Bulk	ALS	0.4959	10	methanol-ethanol	3.0	3.925
11/18/2011	Bulk	ALS	0.4959	10	methanol-ethanol	2.8	3.926
11/18/2011	Bulk	ALS	0.4959	10	methanol-ethanol	2.4	3.935
11/18/2011	Bulk	ALS	0.4959	10	methanol-ethanol	1.5	3.953
11/18/2011	Bulk	ALS	0.4959	10	methanol-ethanol	0.9	3.969
11/18/2011	Bulk	ALS	0.4959	10	methanol-ethanol	0.3	3.978
11/18/2011	Bulk	ALS	0.4959	10	methanol-ethanol	0.0	3.989
11/19/2011	Bulk	ALS	0.4959	15	methanol-ethanol	0.3	3.961
11/19/2011	Bulk	ALS	0.4959	15	methanol-ethanol	0.5	3.963
11/19/2011	Bulk	ALS	0.4959	15	methanol-ethanol	1.8	3.935
11/19/2011	Bulk	ALS	0.4959	15	methanol-ethanol	2.1	3.930
11/19/2011	Bulk	ALS	0.4959	15	methanol-ethanol	3.0	3.913
11/19/2011	Bulk	ALS	0.4959	15	methanol-ethanol	4.1	3.894
11/19/2011	Bulk	ALS	0.4959	15	methanol-ethanol	4.8	3.880
11/19/2011	Bulk	ALS	0.4959	15	methanol-ethanol	5.4	3.875
11/19/2011	Bulk	ALS	0.4959	15	methanol-ethanol	6.3	3.863
11/19/2011	Bulk	ALS	0.4959	15	methanol-ethanol	6.8	3.851
11/19/2011	Bulk	ALS	0.4959	15	methanol-ethanol	7.7	3.840
11/19/2011	Bulk	ALS	0.4959	15	methanol-ethanol	8.3	3.830
11/19/2011	Bulk	ALS	0.4959	15	methanol-ethanol	9.0	3.822
11/19/2011	Bulk	ALS	0.4959	15	methanol-ethanol	10.5	3.806
11/19/2011	Bulk	ALS	0.4959	15	methanol-ethanol	10.0	3.811
11/19/2011	Bulk	ALS	0.4959	15	methanol-ethanol	8.8	3.824
11/19/2011	Bulk	ALS	0.4959	15	methanol-ethanol	4.1	3.895
11/19/2011	Bulk	ALS	0.4959	15	methanol-ethanol	3.4	3.918
11/19/2011	Bulk	ALS	0.4959	15	methanol-ethanol	2.5	3.932
11/19/2011	Bulk	ALS	0.4959	15	methanol-ethanol	1.4	3.959
11/19/2011	Bulk	ALS	0.4959	15	methanol-ethanol	0.7	3.977
11/19/2011	Bulk	ALS	0.4959	15	methanol-ethanol	0.0	4.006
5/24/2012	Bulk	ALS	0.6199	10	mineral oil	0.2	4.028
5/24/2012	Bulk	ALS	0.6199	10	mineral oil	1.3	3.961
5/24/2012	Bulk	ALS	0.6199	10	mineral oil	2.5	3.932
5/24/2012	Bulk	ALS	0.6199	10	mineral oil	3.5	3.918
5/24/2012	Bulk	ALS	0.6199	10	mineral oil	4.3	3.895
5/24/2012	Bulk	ALS	0.6199	10	mineral oil	7.7	3.848
5/24/2012	Bulk	ALS	0.6199	10	mineral oil	7.4	3.855
5/24/2012	Bulk	ALS	0.6199	10	mineral oil	5.8	3.874
5/24/2012	Bulk	ALS	0.6199	10	mineral oil	5.1	3.887
5/24/2012	Bulk	ALS	0.6199	10	mineral oil	4.4	3.904
5/24/2012	Bulk	ALS	0.6199	10	mineral oil	1.7	3.956

5/24/2012	Bulk	ALS	0.6199	10	mineral oil	0.0	3.980
5/25/2012	Bulk	ALS	0.6199	50	mineral oil	0.2	4.026
5/25/2012	Bulk	ALS	0.6199	50	mineral oil	0.4	4.021
5/25/2012	Bulk	ALS	0.6199	50	mineral oil	0.9	3.950
5/25/2012	Bulk	ALS	0.6199	50	mineral oil	1.4	3.947
5/25/2012	Bulk	ALS	0.6199	50	mineral oil	2.0	3.942
5/25/2012	Bulk	ALS	0.6199	50	mineral oil	2.7	3.930
5/25/2012	Bulk	ALS	0.6199	50	mineral oil	4.8	3.895
5/25/2012	Bulk	ALS	0.6199	50	mineral oil	4.1	3.901
5/25/2012	Bulk	ALS	0.6199	50	mineral oil	3.5	3.913
5/25/2012	Bulk	ALS	0.6199	50	mineral oil	2.6	3.934
5/25/2012	Bulk	ALS	0.6199	50	mineral oil	1.3	3.963
5/25/2012	Bulk	ALS	0.6199	50	mineral oil	0.6	3.972
5/25/2012	Bulk	ALS	0.6199	50	mineral oil	0.0	3.979
5/25/2012	Bulk	ALS	0.4959	50	methanol-ethanol	0.2	4.002
5/25/2012	Bulk	ALS	0.4959	50	methanol-ethanol	0.4	3.995
5/25/2012	Bulk	ALS	0.4959	50	methanol-ethanol	0.7	3.957
5/25/2012	Bulk	ALS	0.4959	50	methanol-ethanol	1.2	3.924
5/25/2012	Bulk	ALS	0.4959	50	methanol-ethanol	1.8	
5/25/2012	Bulk	ALS	0.4959	50	methanol-ethanol	2.0	3.957
5/25/2012	Bulk	ALS	0.4959	50	methanol-ethanol	2.6	3.934
5/25/2012	Bulk	ALS	0.4959	50	methanol-ethanol	3.5	3.913
5/26/2012	Bulk	ALS	0.4959	50	methanol-ethanol	4.3	3.894
5/26/2012	Bulk	ALS	0.4959	50	methanol-ethanol	2.1	3.949
5/26/2012	Bulk	ALS	0.4959	50	methanol-ethanol	1.5	3.960
5/26/2012	Bulk	ALS	0.4959	50	methanol-ethanol	0.6	3.975
5/26/2012	Bulk	ALS	0.4959	50	methanol-ethanol	0.0	3.976
6/23/2012	Bulk	CHESS	0.4859	100	mineral oil	0.0	4.026
6/23/2012	Bulk	CHESS	0.4859	100	mineral oil	0.1	4.026
6/23/2012	Bulk	CHESS	0.4859	100	mineral oil	0.3	4.026
6/23/2012	Bulk	CHESS	0.4859	100	mineral oil	0.7	3.965
6/23/2012	Bulk	CHESS	0.4859	100	mineral oil	0.7	3.968
6/23/2012	Bulk	CHESS	0.4859	100	mineral oil	0.6	3.972
6/23/2012	Bulk	CHESS	0.4859	100	mineral oil	0.2	4.026
6/23/2012	Bulk	CHESS	0.4859	100	mineral oil	0.2	4.025
6/23/2012	Bulk	CHESS	0.4859	100	mineral oil	0.3	4.025
6/23/2012	Bulk	CHESS	0.4859	100	mineral oil	0.4	4.020
6/23/2012	Bulk	CHESS	0.4859	100	mineral oil	0.6	4.015
6/23/2012	Bulk	CHESS	0.4859	100	mineral oil	0.8	3.968
6/23/2012	Bulk	CHESS	0.4859	100	mineral oil	1.2	3.958
6/23/2012	Bulk	CHESS	0.4859	100	mineral oil	1.5	3.952
6/23/2012	Bulk	CHESS	0.4859	100	mineral oil	1.7	3.940
6/23/2012	Bulk	CHESS	0.4859	100	mineral oil	1.6	3.941
6/23/2012	Bulk	CHESS	0.4859	100	mineral oil	0.0	3.990

B.2 Supplementary data: γ-β transition.

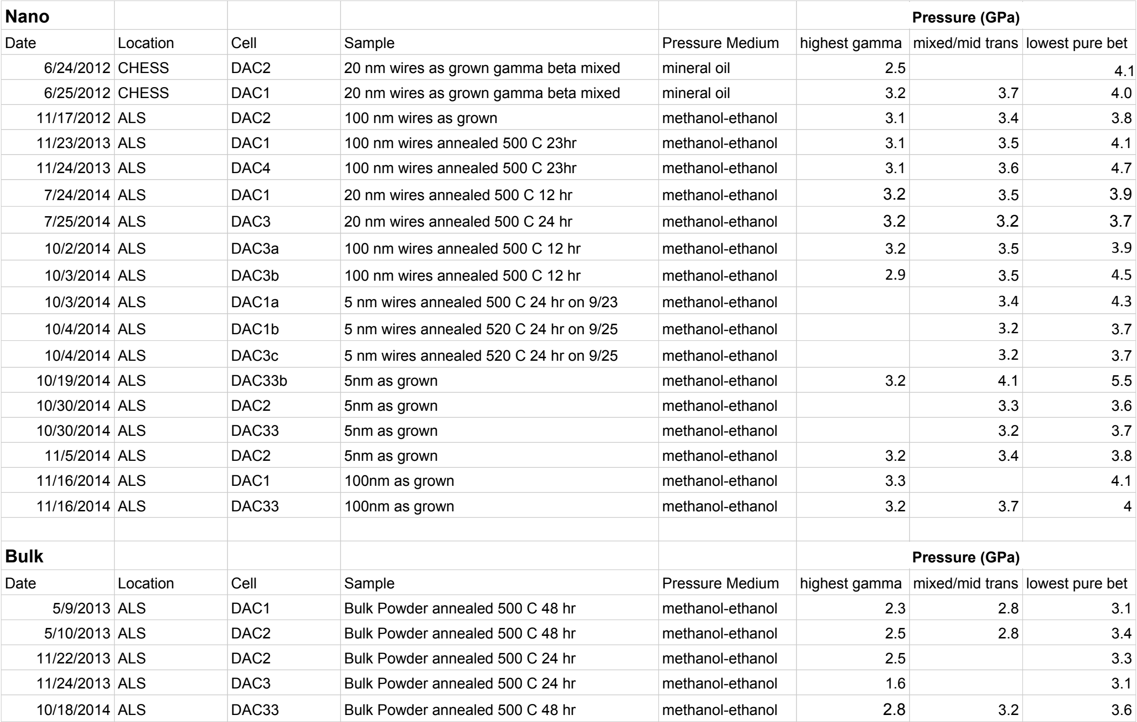

Nano						**Pressure (GPa)**	
Date	Location	Cell	Sample	Pressure Medium	highest gamma	mixed/mid trans	lowest pure bet
6/24/2012	CHESS	DAC2	20 nm wires as grown gamma beta mixed	mineral oil	2.5		4.1
6/25/2012	CHESS	DAC1	20 nm wires as grown gamma beta mixed	mineral oil	3.2	3.7	4.0
11/17/2012	ALS	DAC2	100 nm wires as grown	methanol-ethanol	3.1	3.4	3.8
11/23/2013	ALS	DAC1	100 nm wires annealed 500 C 23hr	methanol-ethanol	3.1	3.5	4.1
11/24/2013	ALS	DAC4	100 nm wires annealed 500 C 23hr	methanol-ethanol	3.1	3.6	4.7
7/24/2014	ALS	DAC1	20 nm wires annealed 500 C 12 hr	methanol-ethanol	3.2	3.5	3.9
7/25/2014	ALS	DAC3	20 nm wires annealed 500 C 24 hr	methanol-ethanol	3.2	3.2	3.7
10/2/2014	ALS	DAC3a	100 nm wires annealed 500 C 12 hr	methanol-ethanol	3.2	3.5	3.9
10/3/2014	ALS	DAC3b	100 nm wires annealed 500 C 12 hr	methanol-ethanol	2.9	3.5	4.5
10/3/2014	ALS	DAC1a	5 nm wires annealed 500 C 24 hr on 9/23	methanol-ethanol		3.4	4.3
10/4/2014	ALS	DAC1b	5 nm wires annealed 520 C 24 hr on 9/25	methanol-ethanol		3.2	3.7
10/4/2014	ALS	DAC3c	5 nm wires annealed 520 C 24 hr on 9/25	methanol-ethanol		3.2	3.7
10/19/2014	ALS	DAC33b	5nm as grown	methanol-ethanol	3.2	4.1	5.5
10/30/2014	ALS	DAC2	5nm as grown	methanol-ethanol		3.3	3.6
10/30/2014	ALS	DAC33	5nm as grown	methanol-ethanol		3.2	3.7
11/5/2014	ALS	DAC2	5nm as grown	methanol-ethanol	3.2	3.4	3.8
11/16/2014	ALS	DAC1	100nm as grown	methanol-ethanol	3.3		4.1
11/16/2014	ALS	DAC33	100nm as grown	methanol-ethanol	3.2	3.7	4
Bulk						**Pressure (GPa)**	
Date	Location	Cell	Sample	Pressure Medium	highest gamma	mixed/mid trans	lowest pure bet
5/9/2013	ALS	DAC1	Bulk Powder annealed 500 C 48 hr	methanol-ethanol	2.3	2.8	3.1
5/10/2013	ALS	DAC2	Bulk Powder annealed 500 C 48 hr	methanol-ethanol	2.5	2.8	3.4
11/22/2013	ALS	DAC2	Bulk Powder annealed 500 C 24 hr	methanol-ethanol	2.5		3.3
11/24/2013	ALS	DAC3	Bulk Powder annealed 500 C 24 hr	methanol-ethanol	1.6		3.1
10/18/2014	ALS	DAC33	Bulk Powder annealed 500 C 48 hr	methanol-ethanol	2.8	3.2	3.6